



POLITECNICO DI TORINO

NANOTECHNOLOGIES FOR ICTS

Design, fabrication and evaluation of silicon tip chips for reverse tip sample scanning probe microscopy

Master's thesis, April 2021

Author:

Giulia SCAMPORRINO

Supervisors:

Matteo COCUZZA

Thomas HANTSCHHEL

—
Academic year 2020/2021

"E: What am I to say?

V: Say, I am happy.

E: I am happy.

V: So am I

E: So am I.

V: We are happy.

E: We are happy. (Silence.) What
do we do now, now that we are
happy?"

Waiting for Godot

Samuel Beckett

Abstract

Recently, a new and promising scanning probe microscopy (SPM) configuration called reverse tip sample (RTS) SPM has been developed at IMEC to overcome the main limitations of the classical SPM approach. In RTS SPM, the classical position of tip and sample is switched: the tip is placed on the stage (where normally the sample is located) and the sample is placed at the cantilever end (where the tip is commonly located). The major advantage of this novel approach is the possibility to substitute a single tip with a chip containing hundreds to thousands of tips. Further advantages of this promising method are: rapid and seamless tip switching within seconds (typically 10 min in the classical configuration), the potential to combine different measurement techniques requiring each a different tip and measure quasi simultaneously with different tips for improved data statistics.

So far, only pyramidal diamond tips made by the common moulding approach have been developed and used for RTS SPM. Despite their high hardness and suitable sharpness, they suffer from a low aspect ratio and are not well suited for all SPM modes. Furthermore, the moulding process is not easily adaptable to other attractive tip materials such as silicon and metals.

Therefore, the main aim of this thesis project is to design, fabricate and evaluate various silicon RTS tip chips prototypes with a focus on high-aspect-ratio tips and the selection of a technology approach adaptable to other tip materials.

For this, the tips geometrical requirements are first analysed and established and a suitable tip chip layout is determined. Next, a manufacturing process based mainly on lithography and dry etching is developed, the silicon RTS tip chips are fabricated and subsequently inspected. Through iterative cycles the process parameters are optimized and improved bringing the tip prototype features closer to the required specifications. Finally, the RTS tip chips functionality and performances are validated through SPM measurements in RTS mode.

Preface

The project presented in this master thesis was carried out at the imec research center in Leuven, Belgium. I did a six-month internship (from October 2020 to March 2021) within the Materials and Components Analysis research group, under the guidance of my mentor Thomas Hantschel. The aim of the research was to manufacture the first silicon tips, optimize the fabrication process steps and finally evaluate the tips performance. Most of the work was done in the cleanroom facilities to perform the lithographic and etching steps and in the atomic force microscopy (AFM) laboratory for the tips performance evaluation.

List of abbreviations

AFM	Atomic force microscopy
CDT	Coated diamond tip
DC	Direct current
EFM	Electron force microscopy
FIB	Focused ion beam
FinFET	Fin field-effect transistor
FDT	Full diamond tip
ICs	Integrated circuits
MFM	Magnetic force microscopy
RTS	Reverse tip sample
RTS SPM	Reverse tip sample scanning probe microscopy
SEM	Scanning electron microscopy
SPM	Scanning probe microscopy
SRP	Spreading resistivity profiling
SSRM	Scanning spreading resistance microscopy
sSSRM	Scalpel scanning spreading resistance microscopy
STM	Scanning tunneling microscopy
TEM	Transmission electron microscopy
BHF	Buffered Hydrofluoric Acid
RF	Radio Frequency
RIE	Reactive ion etching
ICP-RIE	Inductively coupled plasma reactive ion etching
SEM	Scanning electron microscopy
DNPs	Diamond nanoparticles
CVD	Chemical vapour deposition

Contents

Abstract	1
Preface	2
List of abbreviations	3
1 Introduction	6
1.1 Project motivations	6
1.2 Project objectives	8
2 Theoretical background	9
2.1 Scanning Probe microscopy	9
2.1.1 Atomic force microscopy	10
AFM working principle	10
AFM probe	12
2.1.2 Scanning spreading resistance microscopy	14
SSRM working principle	14
SSRM probe	18
2.1.3 Scalpel SSRM	20
Scalpel SPM working principle	21
sSSRM probe	21
2.2 Reverse tip sample SPM	22
2.2.1 Introduction	22
2.2.2 RTS SPM working principle	23
2.2.3 RTS SPM tips fabrication based on molding	24
2.2.4 RTS SPM sample	26
3 RTS SPM silicon tip chips	27
3.1 Introduction	27
3.2 Geometrical requirements	27
3.2.1 Tip material	28

<i>CONTENTS</i>	5
3.2.2 Tip shape and dimensions	29
Tip base	29
Tip shape	29
Tip height	29
Distance between tips	30
3.3 Mask design	32
3.4 Fabrication process	34
3.4.1 Dry etching	36
Dry etching parameters	37
Experimental research general information	39
First set of experiments: etch rate	40
Second set of experiments: tip tapering	42
Third set of experiments: looking for the right shape	45
Fourth set of experiments: new approach	47
Fifth set of experiments: refine the tip features	51
Sixth set of experiments: increase of the tip aspect ratio	55
3.5 Conclusions	58
4 RTS SPM measurements	59
4.1 Introduction	59
4.2 Samples	59
4.3 RTS SPM measurements	61
4.3.1 Sample A	61
4.3.2 Sample B	63
4.3.3 Sample C	66
4.3.4 Sample D	67
4.4 Samples E	68
5 Conclusions and outlook	72
5.1 Conclusions	72
5.2 Future work and outlook	74
Acknowledgments	75
List of Figures	76
List of Tables	78
Bibliography	78

1. Introduction

1.1 Project motivations

The incessant need of the semiconductor industry to have smaller, faster, cheaper and more performing integrated circuits (ICs) has recently led to the introduction of sub 10-nanometers nodes and the inauguration of a new era made of three-dimensional and high performance transistors [1]. Unfortunately, the arrival of this new technology has opened a Pandora's box, in the sense that, the research and development of these smaller technological nodes has created also enormous production and characterization issues [2], [3]. The precise determination of the carrier distribution plays a key role in tackling the new device characterization challenges. Therefore new methods are needed that allow not only 1D and 2D, but also 3D analysis of the carrier distribution with a 1-nm spatial resolution. The Scanning Probe Microscopy (SPM) technique has proven itself as the best candidate for this role in the past two decades because it allows for ultra-high resolution measurements and it is an extremely versatile instrument [4], [5]. The SPM tool uses a probe formed by a needle-shaped tip, on the order of nanometers, to scan the surface of the sample. The interaction between the tip and the sample is recorded and quantified; this allows to perform different kind of analysis. Depending on the type of information obtained and the type of probe being used, it is possible to distinguish different techniques that belong to the probe microscopy family. Among these, the Scanning Tunneling Microscopy (STM) [6] and the Atomic Force Microscopy (AFM) [7] are particularly known.

Starting from the AFM setup, an operating mode able to quantify carrier distribution in a semiconductor material was developed: Scanning Spreading Resistance Microscopy (SSRM) [8], [9], [10]. In SSRM, a small conductive tip is used to measure the local spreading resistance, which is directly proportional to the local resistivity. This is done by applying a bias voltage between the tip and a back contact and measuring the resulting current. By sliding the tip over the entire sample it is possible to obtain a 2D map of the local spreading resistance

with a spatial resolution linked to the radius of the tip. A high pressure (8-12 GPa on silicon structures) is applied between the tip and the sample in order to make the spreading resistance the dominant component in the sample total resistance. Due to the high pressure used, the standard AFM tips are deformed, therefore they are replaced by doped diamond or diamond-coated Si tips [11].

SSRM is therefore able to provide a 2D map of the spreading resistance and accordingly of the carrier distribution. Obtaining 3D-images with a technique that provides 2D-images is possible by collecting 2D-images of successive planes, i.e. at different depths of the sample. A slice-and-view approach, already employed in other imaging techniques, is used but with some changes, as it must be able to dissect the device with nanometric steps that do not disturb the original carrier distribution [12], [13], [14], [15].

Focused Ion Beam (FIB) sectioning allows to obtain subsequent cross-sections with nm-step but the ion beam amorphizes the top material and leads to ion implantation (Ga) which impacts the property measured: therefore it is not suited. A very good technique that can be used is the Scalpel SPM. This technique provides SSRM with the desired extension, able to apply the slice-and view approach by means of a tip-induced material removal method [16].

The classic configuration of the AFM tool, therefore also applicable to SSRM, only allows the use of a single tip to scan the sample. Therefore when Scalpel-SSRM is used, in order to obtain the 3D-carrier distribution, only one tip is used for both analysis and material removal. This leads to a limited possibility in obtaining high-throughput measurements, as the tip must be replaced frequently; furthermore there is a rapid loss of resolution during the measurements due to progressive damage of the tip. A possible solution could be to use one tip for analysis and another one for material removal but the required constant tip changes would make the process very long, since the time required for manual probe exchanges is about ten minutes (one hour if the measurement is done under high vacuum).

Therefore recently, at IMEC, a new configuration has been developed, the Reverse Tip Sample SPM (RTS SPM), which provides the possibility to easily and quickly change the tip during the measurement. This method involves inverting the positions of the tip and the sample: the sample is positioned at the end of the cantilever and mounted on the AFM tool, while the probe tips on which the sample is scanned are placed in place of the sample. It is possible to construct a tip chip in such a way that a small cantilever translation allows the selection of a new tip. This makes it easy to use one tip for SSRM and another one for removing material [17].

1.2 Project objectives

As shown in the previous section, RTS SPM is a promising approach for tackling future SPM challenges because it overcomes the single-tip limitation of classical SPM. First RTS SPM feasibility measurements have been demonstrated [17] using diamond tip chips developed in a previous master thesis work [18]. The existing RTS tip fabrication technology is limited to pyramidal diamond tips which can be made by a molding process. Despite their high hardness and suitable sharpness, tips made in this way suffer from low tip aspect ratio. Furthermore, it cannot be easily adapted to other more common and also attractive tip materials such as for example silicon and metals. Therefore, this master thesis explores the development of RTS tip chips made out of silicon. The specific objectives of this work can be summarized as follows:

- analyze the geometrical requirements for the wanted high-aspect-ratio tip structures based on existing SPM setup;
- translate the tip geometrical requirements into suitable tip array structures for fabrication by lithography and dry etching;
- develop a process, fabricate and inspect silicon RTS tip chips and further improve and optimize their processing during iterative cycles;
- evaluate the functionality and performance of fabricated tip chips in RTS SPM mode and benchmark them against classical SPM.

2. Theoretical background

2.1 Scanning Probe microscopy

The realization of tools that allow to investigate the chemical, physical and structural properties of materials, at the micro, nano and atomic level, is a fundamental step for progress in modern sciences. Structural information can be obtained thanks to Scanning and Transmission Electron Microscopy (SEM and TEM) while obtaining a high resolution analysis of the electronic properties, has only been possible since 1981, with the development of Scanning Tunneling Microscopy (STM) [6]. STM, based on tunneling between a sharp tip and a conductive surface, was able to provide high resolution images of the local electronic properties of a sample. In 1986 the Atomic Force Microscopy (AFM) was developed [7], based on the interaction force between a tip, positioned at the end of a cantilever, and a surface. AFM has been a very powerful invention as its use can be extended to different types of analysis: topographic, electrical, magnetic and chemical. The incredible property to measure both probe currents and sample-tip forces at the nano and atomic scale has led to a rapid growth of the varieties of Scanning Probe Microscopy (SPM) techniques.

In this chapter we will analyze the operating principle of the AFM system, underlining the operating modes and the various components of the AFM probe. An in-depth study will then follow on one of the various applications of AFM, Scanning Spreading Resistance Microscopy (SSRM), in order to determine the 2D charge carriers distribution in a device and a possible solution to extend the mapping into three dimensions.

2.1.1 Atomic force microscopy

Atomic force microscopy (AFM) was introduced in 1986 by Binnig et al. [7],[19] as a new method for measuring the topography of a sample. Historically, AFM was preceded and inspired by scanning tunneling microscopy (STM), invented in 1981, which is based on the electron tunneling between a metal tip and a conductive sample in an external electric field. In AFM a special probe, composed of an elastic cantilever having a sharp tip on the end, is used to measure the interactive force between the tip and the sample. The variation of this force, when the tip is moved along xy -plane of the sample, provides the signal and it allows to map the contours of the sample surface.

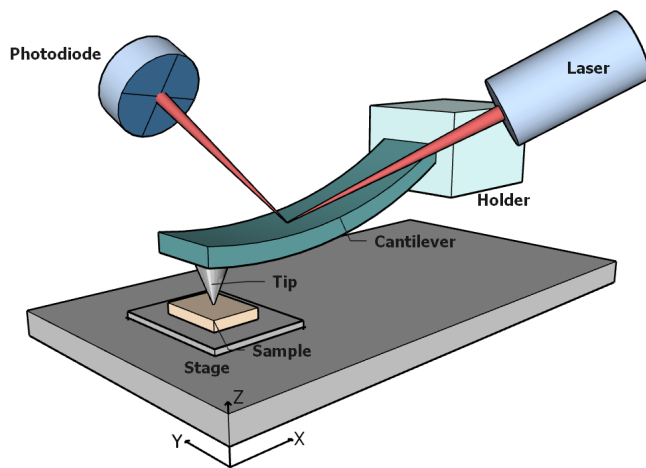


Figure 2.1

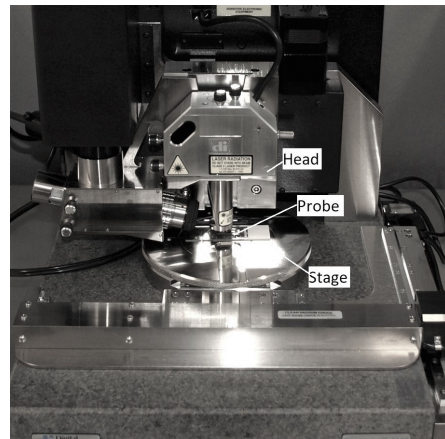


Figure 2.2

Fig.2.1: AFM setup: the tip is scanned in $x-y$ plane over the sample, its movement along the z -direction is detected by a photodetector. Fig.2.2: AFM D3100 from Digital Instrument [20]

AFM working principle

The structure of AFM apparatus is shown in figure 2.1. The tip is located at the end of the cantilever and it interacts with the sample during the scan. The force applied from the sample to the tip causes a bending of the cantilever and, by measuring the deflection of the latter, it is possible to evaluate the interaction force between the tip and the sample. In order to record the small deflection of the elastic cantilever an optical method called *beam-bounce* is used: a beam is emitted by a laser diode, is focused on the cantilever and is subsequently reflected towards the center of a photodetector. A four-section split photodiode is used as a position-sensitive photodetector. Initially the reflected beam is positioned in such a way that it hits the photodiode in the middle. During the measurement,

a variation of the tip-sample force, therefore a variation of the z -position of the tip, causes a bending of the cantilever and therefore a movement of the laser spot with respect to the center of the photodiode. Two quantities can be measured in this way: the cantilever bending due to attractive and repulsive forces along the z -direction or the cantilever torsions due to lateral components of the tip-sample force. The current variation in the photodiode with respect to the initial condition is measured. If I_{01} , I_{02} , I_{03} and I_{04} are the reference values of the photocurrent in the photodiode four sections, and I_1 , I_2 , I_3 and I_4 are the current values after a change of cantilever position, then it is possible to calculate the differential current for each section $\Delta I_i = I_i - I_0$ that will determine the intensity and the direction of the cantilever deflection [5]. A Dimension 3100 AFM, used in this project, is shown in figure 2.2.

There are two different ways to acquire images during an AFM measurement: the contact mode and the intermittent contact mode mode.

Contact mode In contact mode the tip apex is in direct contact with the sample surface and the tip-sample force is counterbalanced by the cantilever deflection. There are two ways to get the sample image in contact mode: constant force and constant average distance. In the constant force mode the current variation along z -direction is considered: $\Delta I_z = (\Delta I_1 + \Delta I_2) - (\Delta I_3 + \Delta I_4)$. It is used as input in a feedback system and it is kept constant by the scanners (piezoelectric transducers). The latter regulate the tip-sample distance in order to keep the forces, therefore the cantilever bending, constant. In this mode, the plot of the z -position of the tip with respect to the xy -coordinate provides an image of the sample profile. In the constant average distance mode the z -position of the tip is maintained constant while the variation of the current, i.e. the variation of the tip-sample interaction force, is recorded. The plot of the current variation with respect the xy -coordinate allows to trace the profile of the sample.

Contact mode is the most generic and widely applicable approach used to generate AFM images. It has an high scanning speed and a high resolution. The cantilevers used have a small stiffness in order to minimize the deformation of the probes and at the same time to limit the influence of the tip on the sample. However, if the sample is particularly sensitive, it may be damaged during scanning, furthermore, the tip can be broken.

Intermittent contact mode Intermittent contact mode was introduced in order to overcome the limitations present in the contact mode. The cantilever is kept in oscillation by a piezo-vibrator at its resonance frequency, with oscillations of about 10-100 nm in amplitude. When the tip approaches the surface, the probe will feel an additional force given by the tip-sample interaction and this will cause the oscillation frequency of the cantilever to vary. The amplitude and phase changes of the cantilever oscillation are recorded. The amplitude changes form the topographic AFM image of the sample while the phase changes bring information about the image contrast.

The AFM lateral resolution is of the order of fractions of nanometers and it is mainly determined by the radius of curvature of the tip and by the sensitivity of the optical system that measures the deflection of the cantilever. The sensitivity of the measurement is defined by the cantilever stiffness. For this reason, a lot of research has been carried out in order to obtain suitable probes for mapping the sample with atomic resolution [5], [21], [22], [23] .

AFM probe

AFM probes are produced today by modern Si wafer technology. A single AFM probe is composed of holder chip, cantilever and tip as shown in figure 2.3.

The holder chip is positioned at one end of the cantilever, it is necessary for probe handling as the cantilever is too thin and delicate to be directly mounted in the AFM system. It is fixed to the cantilever during the fabrication process. It is made out of Si, glass or metal and is about 3.2 mm long, 1.6 mm wide and 0.5 mm thick.

The cantilever is sandwiched between the tip and the holder, it is about 100-450 μm long, 50 μm wide and 0.3-10 μm thick. The cantilever elastic constant k depends on the cantilever material and geometry. The k values for common probes vary in the range 0.1 – 50 N/m. The cantilever resonant frequency ω determines the maximum scan rate and it is a relevant parameter in the intermittent constant mode. It is determined by the following formula:

$$\omega = \frac{\lambda}{l^2} \sqrt{\frac{EJ}{\rho S}}, \quad (2.1)$$

where l is the cantilever length, E the Young's modulus, J the inertia moment of the cantilever cross-section, ρ the material density, S the cross section and λ a numerical coefficient that indicates the oscillation mode. For the main modes ω is in the 10-400 kHz range [5], [24].

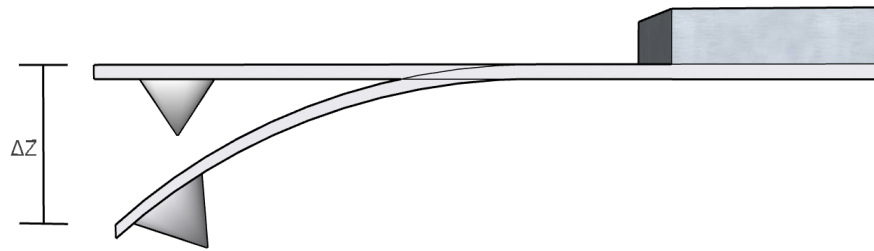


Figure 2.3: AFM probe schematic figure: the AFM probe is composed of holder chip, cantilever and tip.

The tip is fixed at the free side of the cantilever. It is mainly used in two configurations: high-aspect-ratio tip and pyramidal tip with low aspect ratio. The interaction force F of a tip with the sample surface can be estimated from Hooke's law:

$$F = k \cdot \Delta Z, \quad (2.2)$$

where k is the cantilever elastic constant and ΔZ is the tip displacement due to the cantilever bending caused by surface-tip force.

The materials used for tips can be different according to the needs, mainly Si, Si_3N_4 metal and diamond are used. Silicon tips are usually sharper whereas silicon nitride tips wear out more slowly than silicon ones. Diamond tips have many advantages: they are wear-resistant and have a stable shape during measurement. Furthermore they can be made with a conductive diamond material and can provide more reliable results in electrical measurements. AFM tips can also be functionalized or coated depending on the need, for example for electrical or magnetic measurements it is necessary to coat the tip with a metal such as cobalt-chromium (CoCr), platinum-iridium (PtIr) or gold (Au) [25].

2.1.2 Scanning spreading resistance microscopy

Scanning spreading resistance microscopy (SSRM) is an electrical characterization technique based on AFM, able to measure the two-dimensional resistivity distribution in semiconductor devices and consequently to determine the local carrier concentration. It was first developed in IMEC in the early nineties [26], [27] in order to improve the performance of Spreading Resistance Profiling (SRP) [28], the previous technique for the in-depth resistivity determination.

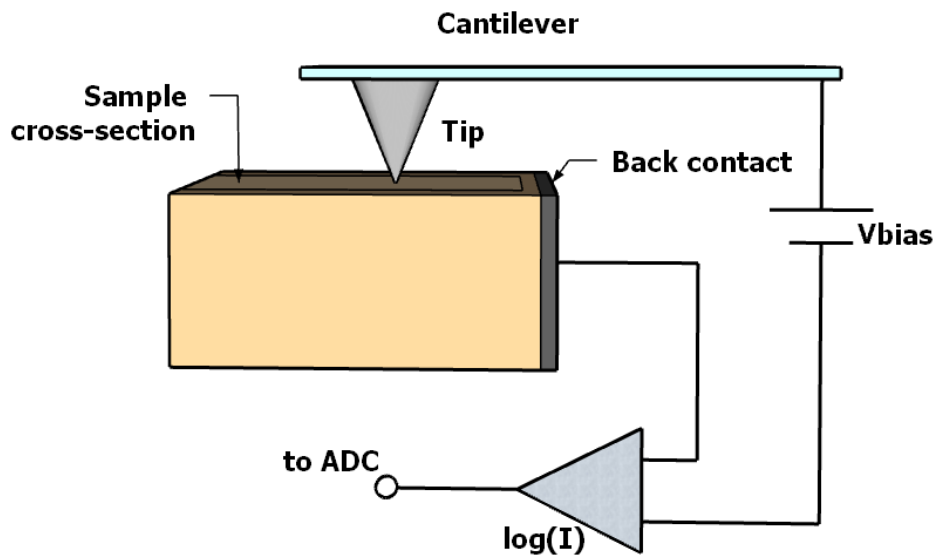


Figure 2.4: SSRM setup schematic figure: a small voltage of about 5-50 mV is applied between the tip and the back contact, the tip is scanned over the sample and the current is measured.

SSRM working principle

In SSRM, a conductive tip, located at the end of a cantilever, is used to scan at high force (μN), in contact mode, along the cross section of the sample as shown in figure 2.4. A DC bias is applied between the conductive tip and an electrical back-contact, positioned on the backside of the sample. Due to the geometry of the system, the electric current flows from the tip to the sample undergoing a constriction first, due to the small apex of the tip, followed by a spreading, given by the fact that the analyzed sample has a larger volume. An electrical resistance called *Spreading Resistance* is associated to the spreading current. The spreading resistance is caused by the spreading current locally below the tip, therefore, if the total resistance of the circuit is dominated by the spreading resistance, it is possible to obtain the resistance value of the sample precisely at

the point where the tip is located. High force is needed to minimize the probe contact resistance and to make the spreading resistance the dominant component of total sample resistance [29]. The resistance value, as shown below, is linked to the carrier concentration and therefore, by knowing the resistance value in a given point of the sample, the local carrier concentration is simultaneously also known. A logarithmic amplifier is used in order to obtain a wide dynamic range in the measurement in the current and consequently allows the analysis of the entire carrier concentration range of interest ($10^{15} - 10^{21} \text{ cm}^{-3}$) [30].

Spreading resistance The measurement of the spreading current given by the nanometric contact existing between the tip and the sample is the goal of SSRM. In the generic case, when the contacts considered are large, the total resistance of a conductor is given by the ohmic resistance and the resistance of the contacts is negligible. In this case, however, having one of the contacts very small, the contact resistance is no longer negligible. If the contact area between the tip and the sample is considered as a disk of radius a and the sample is considered a semi-infinite medium of resistivity ρ , then the spreading resistance is the dominant resistance. It is described by Maxwell's spreading resistance formula if a is large with respect to the mean free path of charge carriers in the sample, otherwise, it is described by Sharvin's law:

$$R_{Maxwell} = \frac{\rho_{sample}}{4a}, \quad (2.3)$$

$$R_{Sharvin} = \frac{4\rho_{sample}\lambda}{3\pi a^2}, \quad (2.4)$$

where λ is the carriers mean free path:

$$\lambda = \mu \frac{\sqrt{3kTm^*}}{e}, \quad (2.5)$$

where μ is the carriers mobility, k the Boltzmann constant, T the temperature, m^* the effective mass and e the electric charge. Since the mean free path is proportional to the carriers mobility, which is doping concentration dependent, then it happens that the mean free path increases with the mobility and consequently decreases with the increase of the doping concentration. In conclusion, for low or medium-low doping values, λ is greater than a and therefore Sharvin's law is used [18].

As previously mentioned, in SSRM it is necessary that the spreading resistance is the predominant component of the resistance, hence the contact resistance

must be negligible. It has been shown that, if the sample is composed of silicon and a high pressure is applied between the tip and the sample, then the silicon, in the region just below the tip, will undergo a phase transition passing from the diamond structure, characteristic of semiconductors, to a metallic $\beta - Sn$ phase. The experimental transition pressure range is 11.3 – 12.6 GPa [31]. It is possible to study the phase transition analysing the resistance-pressure behaviour: a bias is applied between the tip and the sample and the resistance is measured at increasing pressure values. It has been shown that, starting from a certain pressure (threshold pressure), a drop in resistance occurs [32], [33]. Before the transition the dominant resistance was that of the contact between the tip and the substrate but after the transition this resistance becomes negligible. The volume of the region that is subjected to transition depends on the applied pressure (as pressure increases, volume increases), therefore it is advisable to work at a pressure just above the threshold value. In this way there are two advantages: the transition lowers the resistance and the tip effective radius becomes much smaller and therefore increases the SSRM resolution [34], [35]. Figure 2.5 shows the difference between the geometrical tip radius, given by the tip shape, the contact radius, given by the insertion depth due to the higher hardness of the tip compared to the substrate and the effective radius, given by the silicon phase transition.

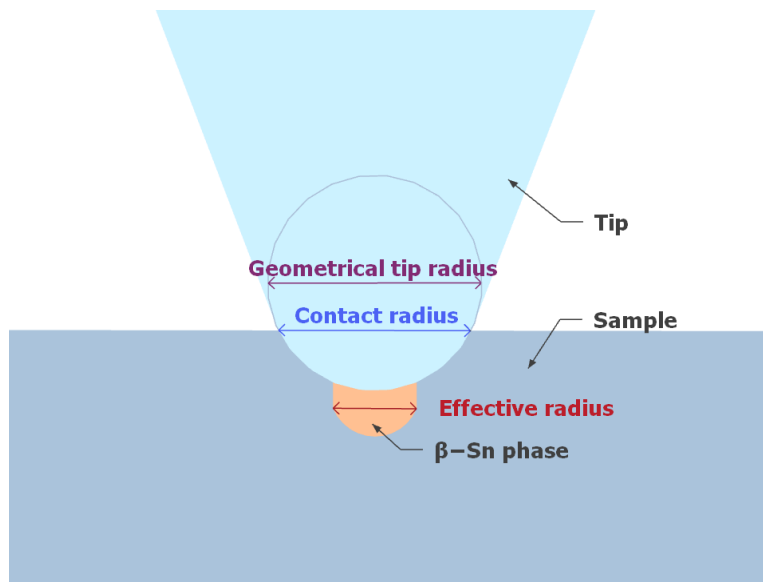


Figure 2.5: SSRM nanocontact schematic figure: this illustration shows how much the effective radius a , due to the phase transition $\beta - Sn$, is smaller than the size of the probe tip.

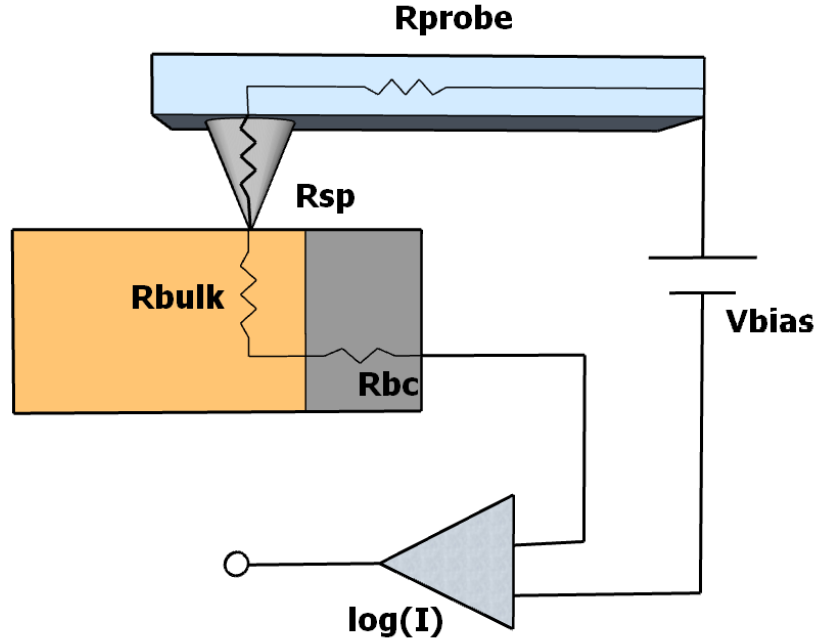


Figure 2.6: SSRM equivalent electric circuit: the spreading resistance R_{sp} is directly linked to sample dopant concentration.

SSRM equivalent circuit The total resistance measured by the SSRM corresponds to the resistance existing between the probe and the sample back-contact and is the sum of different contributions:

$$R_{tot} = R_{sp} + R_{bulk} + R_{bc} + R_{probe}, \quad (2.6)$$

as shown in figure 2.6. R_{sp} is the spreading resistance, R_{bulk} , R_{bc} and R_{probe} are respectively the resistance of the sample along the path that connects the tip to the back-contact, the back-contact resistance and the intrinsic resistance of the probe. As previously mentioned, only the spreading resistance value is linked to the local carrier concentration of the sample and therefore the correct local carrier concentration can be extracted only if the other resistance terms are negligible. Unfortunately, even if this condition was fulfilled, in practice it is not possible to quantify the local carrier concentration in this way because:

- the tip effective radius a is unknown,
- the contact between the tip and the sample is actually non ohmic but it is influenced by the surface states and by the nature of the contact between the $\beta - Sn$ region and the sample,
- the high pressure applied leads to a bandgap modifications under the transi-

tion region and so the standard values of the effective mass and the mobility cannot be used.

The only solution to extract the desired information is to use a calibration sample, which allows to obtain a calibration curve. This calibration sample is a sample formed by different doping regions covering the range of interest, therefore knowing the response of a known sample allows the quantification of an unknown sample, measured under the same conditions [30].

SSRM probe

As described in the previous section, the SSRM probe is composed, as for the AFM system, of holder chip, cantilever and tip.

The SSRM holder chip dimensions are the same as for the AFM probe. It must have a highly conductive surface in order to provide good electrical contact between the probe and the AFM system. The connection between the holder chip and the cantilever membrane must also be conductive.

The cantilever stiffness required is high because of the high pressure needed for the measurement. The pressure generated must be from 10 GPa to 12 GPa therefore the required elastic constant is adjusted to the range 10-40 N/m. It is possible to make probes with three cantilevers, having different lengths, in order to have three different elastic constants available. The cantilever is usually made of Si or metal. Silicon nitride is not suitable due to its low stiffness. Diamond, despite its high rigidity, is not suitable; diamond cantilevers suffer from high internal stress during bending and they have a rough surface due to the laser used for deflection detection [24].

The tip is a key element of the SSRM setup. It must generally be sharp, electrically conductive and wear resistant but its characteristics will also depend on the type of material to be probed. For example, silicon is a very hard material and therefore it is necessary to establish a high pressure with the tip to keep the contact stable. In this case, diamond tips are the best candidates while metal tips fail [36]. Diamond is a very hard and stable material; furthermore its high Young's modulus (1220GPa) makes it wear resistant much more than silicon (Young's modulus = 185GPa) or silicon nitride (Young's modulus = 250GPa) [37]. There are two main types of diamond tips: Full Diamond Tips (FDTs) and Coated Diamond Tips (CDTs) [38], [39]. FDTs are manufactured with a technique called tip molding: an inverted pyramid-shaped silicon mold is anisotropically etched, then is filled with the diamond and finally is removed. CDTs, on the other hand, are formed by silicon tips covered with a diamond layer. FDTs have a high mechanical

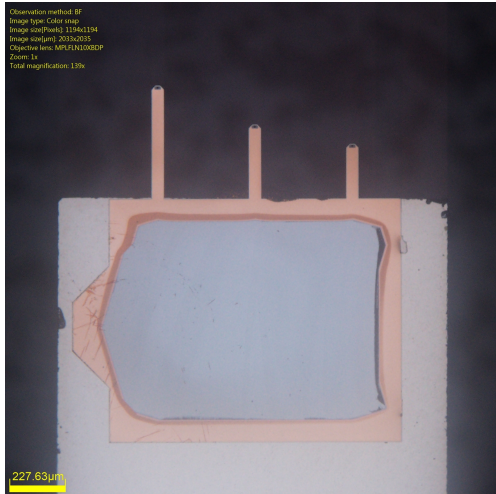


Figure 2.7: SSRM probe composed of three different nickel cantilevers.



Figure 2.8: SSRM probe, zoom on the medium cantilever.

stability due to a low aspect ratio but suffer from lower electrical conductivity. CDTs have a higher electrical conductivity but they often break near the apex due to the high force used during the scanning. Finally, FDTs are superior to CDTs in terms of spatial resolution.

Figure 2.7 shows an example of an SSRM probe. It is composed of three different nickel cantilevers, respectively $465 \mu\text{m}$, $305 \mu\text{m}$, and $225 \mu\text{m}$ long. Figure 2.8 shows a zoom-in of the medium cantilever end where the diamond tip area can be seen. It has a pyramid shape with a $7 \mu\text{m} \times 7 \mu\text{m}$ base and it is made of diamond.

2.1.3 Scalpel SSRM

As already said in the introduction, section 1.1, the need for ever smaller and more performing devices has also led to changes in the characterization techniques. With the introduction of the FinFET [40], the need to know the distribution of carriers in 3D arises in order to investigate the correlation between the device performances and 3D-doping distribution. As described above in section 2.1.2, SSRM is able to provide a 2D-spreading resistance map and therefore a 2D carrier distribution map. It can be extended to the third dimension, by collecting 2D images of successive planes, i.e. by carrying out the measurement along the xy plane at different sample depths z [15], as shown in figure 2.9.

The transition from one layer to another can be done in different ways, some are more effective than others: for example, it is possible to use the Focused Ion Beam (FIB) to remove one layer and move to next one. Unfortunately, the use of FIB strongly impacts the electrical measurements as the ions used in the beam change the crystallinity and the electrical properties of the sample [41]. The Scalpel-SSRM (sSSRM) method has recently been developed, in which the tip itself of the SSRM is used as a scalpel to remove the material layer by layer. This method doesn't cause electrical alterations in the sample and then allows to perform nanometric steps between two consecutive layers.

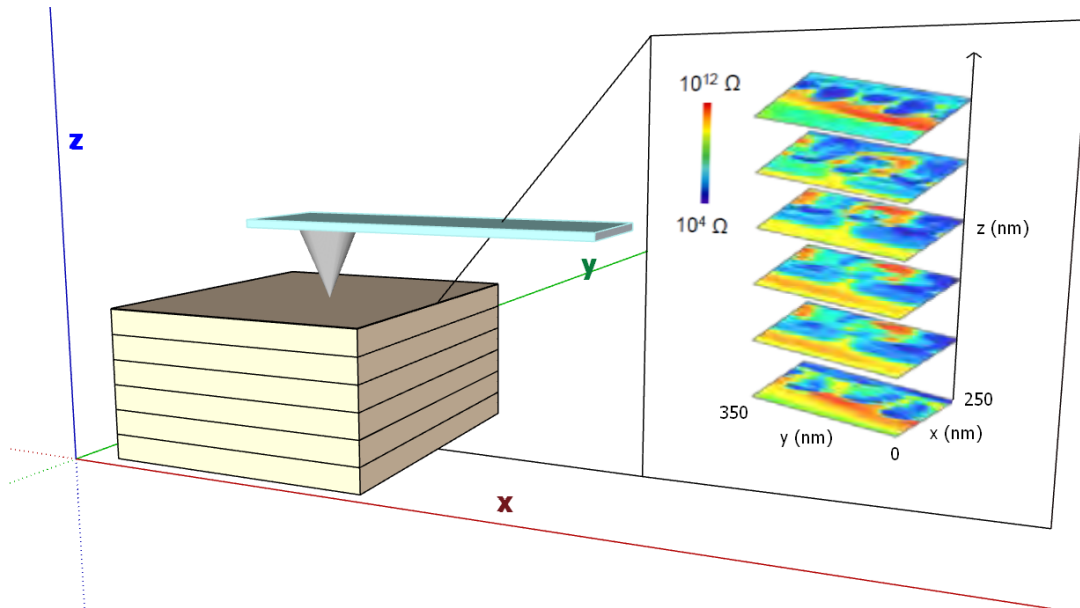


Figure 2.9: Scalpel SPM, 3D-image as a sum of 2D-images at different z depths [16].

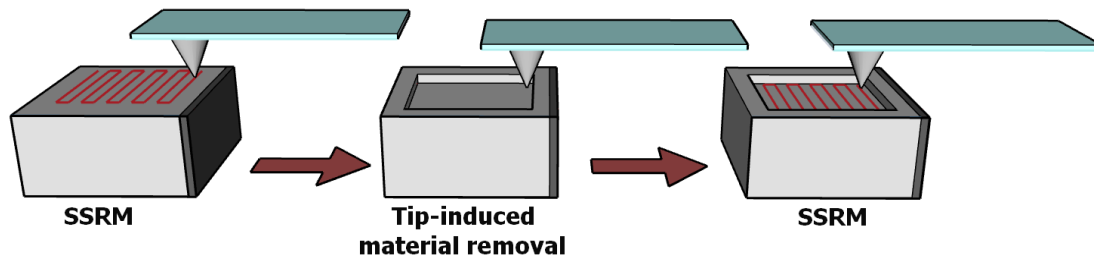


Figure 2.10: Scalpel SSRM working principle schematic figure: the region of interest is scanned and a 2D image is acquired, then a layer of material is removed by high pressure scanning. This cycle is repeated until the whole region of interest is scanned.

Scalpel SPM working principle

As shown in figure 2.10, sSSRM consists of two different phases: SSRM and tip-induced material removal. First, the sample is scanned, as in a classic SSRM, and subsequently the analyzed layer is removed from the tip by applying a high pressure, making the new layer accessible. These steps are repeated iteratively until the desired depth of the sample is reached. In this way consecutive 2D carrier maps are generated with sub-2nm resolution, forming an high resolution 3D carrier map of the sample [42].

sSSRM probe

The probe used for sSSRM is the same as for SSRM: a cantilever with a tip at its end. The tip is used for both measuring and material removal. Full diamond tips are the better choice in order to limit the probe wear [43]. As mentioned above, the use of a single tip is very limiting: the tip is worn quickly during the material removal and this causes the loss of resolution in the measurement phase. Furthermore the tip can be contaminated by the sample during the removal of the material, part of the sample material can deposit on the tip varying its apex and its properties.

2.2 Reverse tip sample SPM

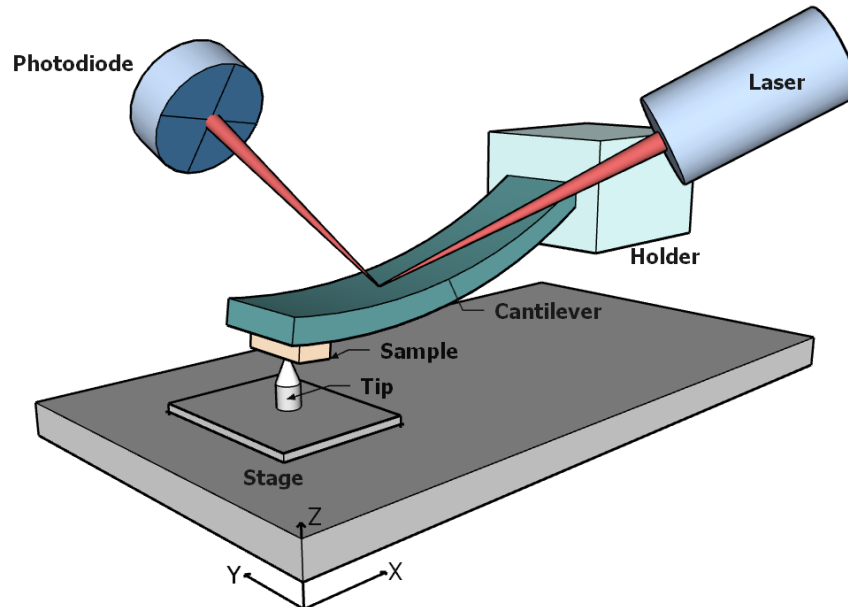


Figure 2.11: RTS SPM setup schematic figure: the position of the tip and the sample is reversed compared to the AFM classical configuration.

2.2.1 Introduction

As mentioned in section 2.1.3 sSSRM, based on one single tip that scans the sample, suffers from several limitations [17]:

- it is often necessary to replace the tip, which wears easily, this leads to long measurement times and is very impractical;
- there is a limited possibility to combine techniques that require different tips;
- the use of different tips, due to their incessant replacement, makes difficult the elimination of tip-induced artefacts and variability.

The need for new ideas that overcome these limitations leads to the implementation of the Reverse Tip Sample (RTS) configuration.

In this chapter the concept of the reverse tip sample is explained in detail, highlighting the strengths of its configuration. The focus will shift then to the tip fabrication and the sample preparation.

2.2.2 RTS SPM working principle

The Reverse Tip Sample configuration, as the name implies, involves the inversion of the respective tip and sample AFM positions. The sample is no longer positioned on the stage but it is placed at the end of the cantilever, while the tip is located on the stage (as shown in figure 2.11). In this way the tip will remain fixed while the sample will be scanned, moving the cantilever, on it. The cantilever motion detection principle remains the same as for classic AFM.

The great potential of this new configuration lies in the fact that it is possible to replace the single tip with a chip consisting of hundreds to thousands of tips, that can be reached with a simple movement of the cantilever, see figure 2.12. With the use of this new approach, the data acquisition is faster since a simple translation of the cantilever allows the passage from a worn tip to a new one. Furthermore, having different tips available, it becomes easier to combine different types of techniques, which require each a different tip. Finally, it is possible to alternate between two different tips during Scalpel SPM: one tip is used to carry out the measurement while another tip, easily interchangeable, is used as a scalpel. Although this structure has been designed to overcome the standard sSSRM limitations, it is possible to extend the concept to other needs as well, since the tips can be of any size and of different materials [17],[18].

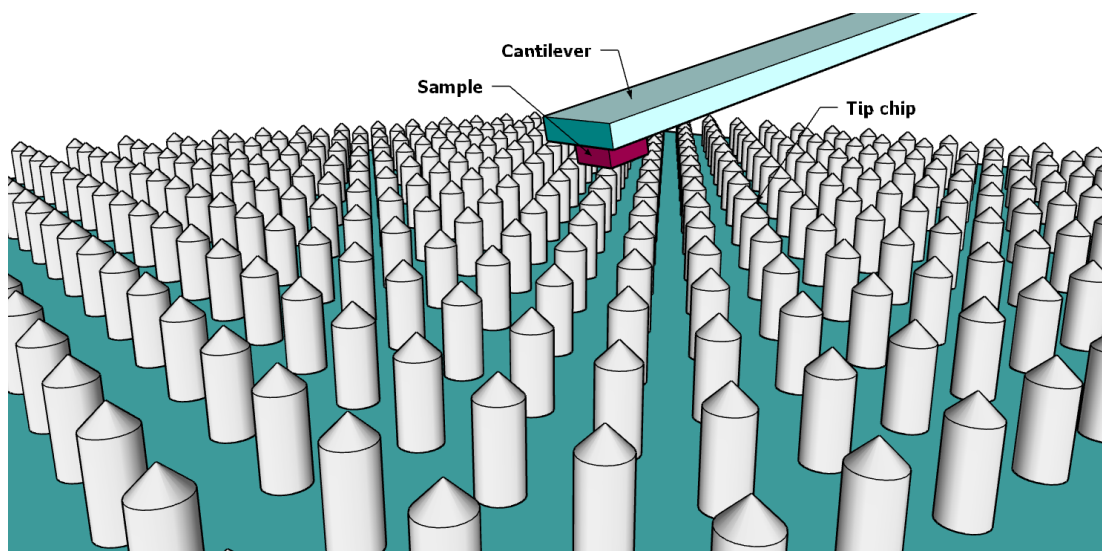


Figure 2.12: RTS SPM concept: this new configuration allows to have thousands of tips available during the measurement.

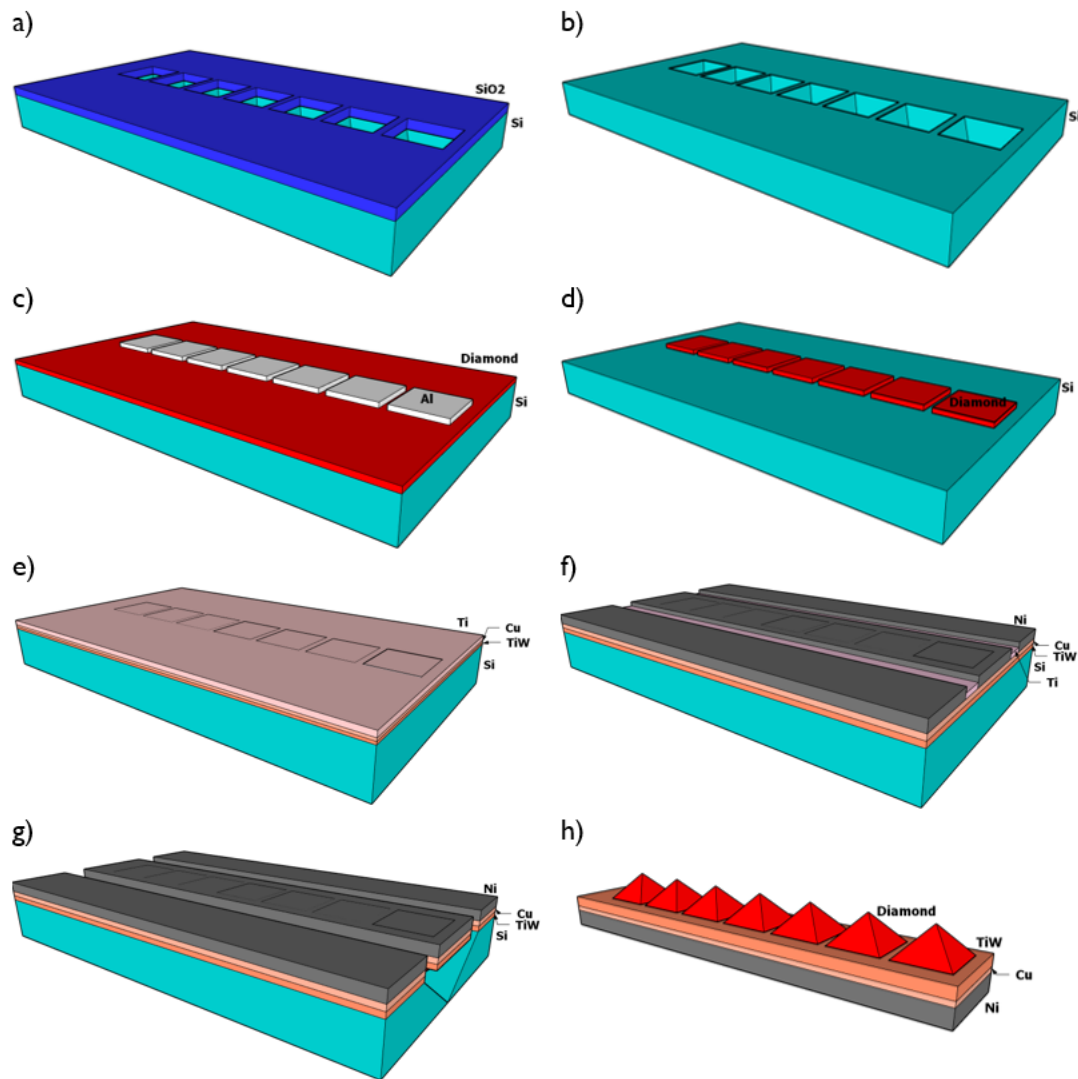


Figure 2.13: Diamond tips fabrication process flow: a) SiO_2 layer is patterned and reverse pyramid molds are etched in the silicon substrate. b) SiO_2 layer is removed. c) Diamond and Al layers are deposited and the aluminum layer is patterned. d) Diamond layer is etched and Al is removed. e) A metal stack composed by TiW/Cu/Ti is deposited. f) Ti layer is patterned and Ni layer is electroplated on exposed Cu. g) The remaining metals are etched and the structure is underetched in KOH. h) The pyramidal diamond tip chip is ready to use.

2.2.3 RTS SPM tips fabrication based on molding

This section describes the existing tip chip fabrication process. In particular, the probes taken into consideration are full diamond tips suitable for SSRM. The method used is based on the already well known full diamond tips manufacturing technique [38]; however, changes have been made to adapt the process, designed for 200 mm silicon wafer, to 100 mm silicon wafer.

The image 2.13 shows the steps of the fabrication process. The diamond tip

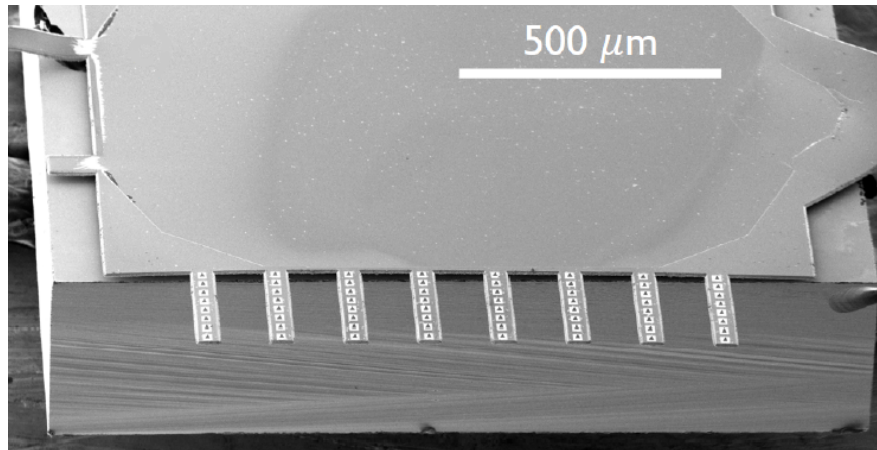


Figure 2.14: SEM image of a diamond RTS chips [18].

chip is created using three lithographic steps, starting from a $\langle 100 \rangle$ silicon wafer coated with a 200 nm silicon oxide layer. In this process the silicon substrate is used as a mold for the diamond tips. The first lithographic step consists in the silicon oxide patterning, as shown in figure 2.13(a). Subsequently the silicon oxide is used as a mask to etch the reversed pyramid mold into the silicon substrate, after that the silicon oxide is removed 2.13(b). Next, a $1\mu\text{m}$ thick boron doped polycrystalline diamond layer is deposited on the wafer followed by an aluminium layer. In the second lithographic step, the aluminum layer is patterned and it is used as hard mask during the diamond etching 2.13(c). The diamond is dry etched and the mask is stripped away 2.13(d). Afterwards, a metal stack of TiW/Cu/Ti is deposited on the wafer. The titanium-tungsten layer is used as an adhesion layer, the copper one is used as nickel electroplating seed layer, while the titanium one is used as protective layer for the copper against the oxidation 2.13(e). The third lithographic step is used to pattern the chip, followed by nickel electroplating, the patterned titanium is used as mask 2.13(f). In the last step, the metals are etched away and the device is underetched in KOH 2.13(g). The final result, after its removal from the wafer, is shown in figure 2.13(h). To facilitate handling, the tips can be created on several cantilevers connected to a membrane. The membrane, as happens for the classic AFM configuration probes, can be glued to a silicon holder chip as shown in figure 2.14 [18].

2.2.4 RTS SPM sample

To carry out the measurement it is necessary to position the sample on the cantilever and this is done by means of a dedicated procedure, shown in figure 2.15. First of all a lamella is prepared, as in the classic TEM sample preparation, with the use of the FIB [44]. The lamella is then placed on a Ni cantilever 2.15(b) and it is fixed on the cantilever by means of encapsulation with an epoxy 2.15(c). Finally, the area of interest is exposed in order to remove all the material in excess. It is done by tip induced erosion.

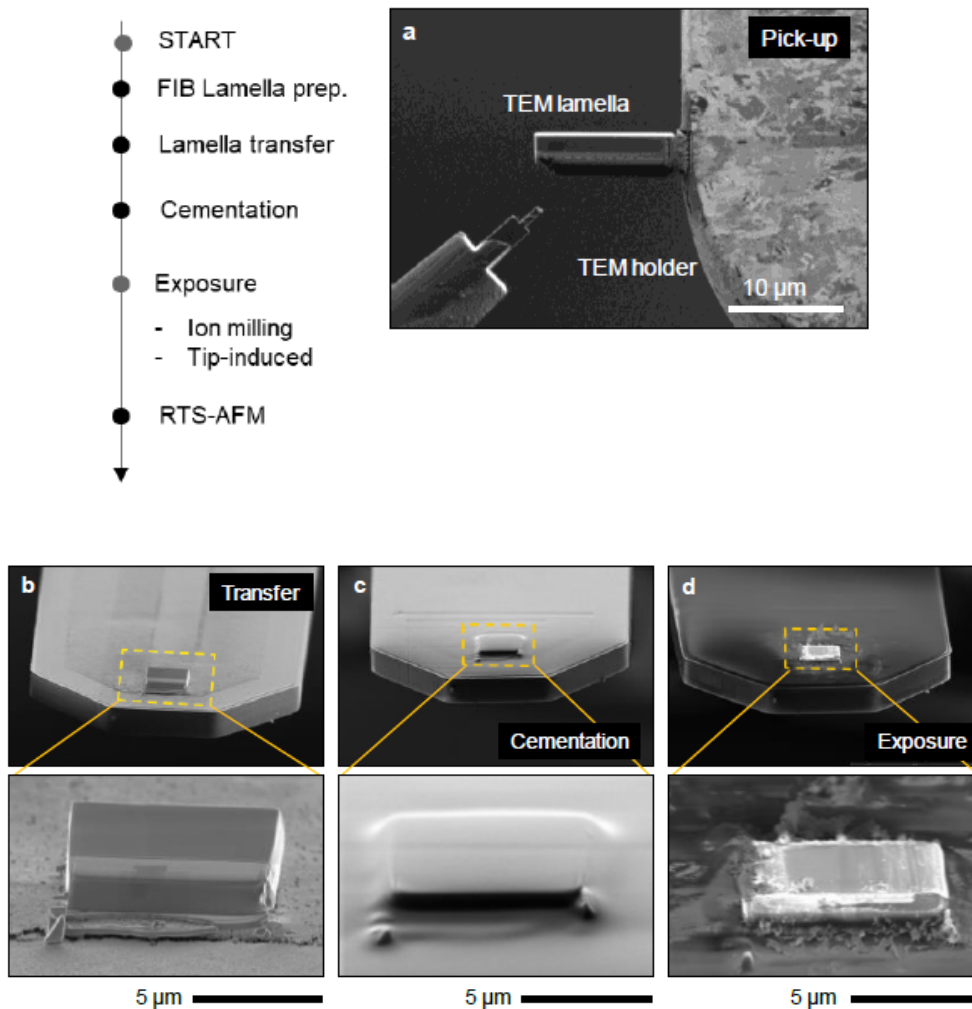


Figure 2.15: Detailed list for the RST sample preparation: a) A TEM lamella is prepared from the sample. b) The lamella is transferred onto the cantilever. c) Sample is fixed to the cantilever. d) The material in excess is removed during the exposure. [17]

3. RTS SPM silicon tip chips

3.1 Introduction

This chapter contains a detailed and accurate description of the project. The chapter first part encloses all the considerations and theoretical studies performed in order to design the desired silicon tip chip. In particular, the focus is posed on the reasons that led to the choice of the material, the shapes and the dimensions used. Subsequently the attention is shifted to the manufacturing steps; once the final objective has been set, a detailed version of the various attempts made to achieve the goal will be provided, including the strengths and limitations of every path followed.

3.2 Geometrical requirements

In the previous chapter the great potential of the RTS SPM were highlighted and the manufacturing steps of the first diamond tip chip have been analyzed. This tip chip has been made up of diamond tips with a pyramidal shape. They have the advantage of having high a hardness and suitable sharpness. The sharpness is a very important parameter: it depends on the tip radius of curvature (i.e. a small the tip radius corresponds to a high tip sharpness) and no data acquired can have a slope steeper than the tip one, hence the tips radius directly determines the minimum resolvable feature of the analyzed surface. For this reason the tip sharpness has to be as high as possible. Despite their important qualities, this type of tips have two main limitations:

- Low tip aspect ratio: by defining the aspect ratio as the ratio between the height of the tip and its base, the pyramidal diamond tip created by the molding process has a low aspect ratio. A high-aspect-ratio tip is important when the features of the sample surface have steep sidewalls such as trenches, if the tip height will be higher than the wall and the tip width will be smaller than the space between the trench sidewalls then the tip will

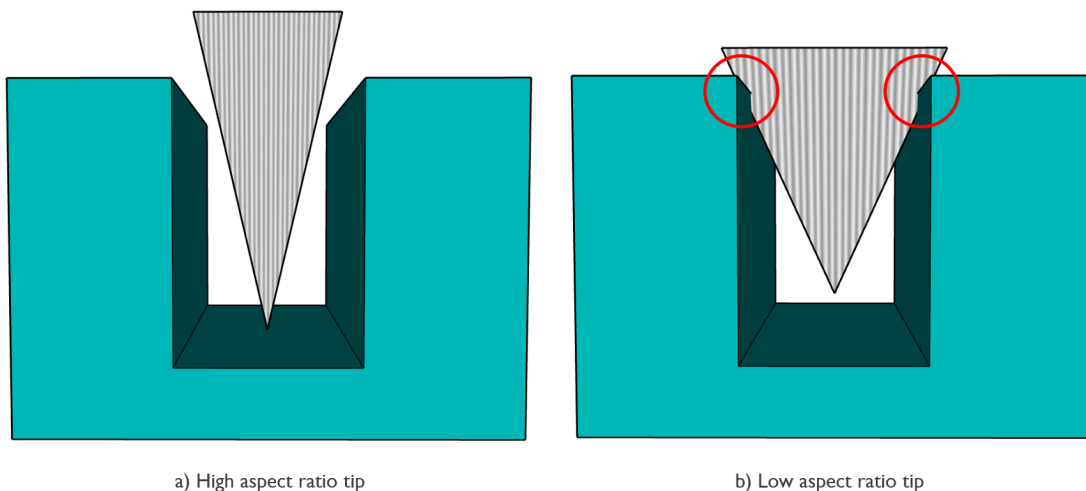


Figure 3.1: Tips with different aspect ratio: a) high-aspect-ratio tip, the tip is able to reach the bottom of the trench and so the measure will be correct. b) low aspect ratio tip, the tip base is larger than the trenches width and the tip height is lower than the sidewalls height and so the tip cannot reach the trench bottom, the measure will not correct.

be able to scan correctly the sample [45], [46], [47]. Otherwise, in case of lower aspect ratio tip, the tip cannot reach the bottom of the trench and the image obtained will not be correct, as shown in figure 3.1.

- The molding process used to create the pyramidal diamond tip chip cannot be adapted to other attractive tip materials such as silicon and metals. Moreover, this type of process involves the use of three lithographic steps (i.e. three different lithographic masks), for each step the lithographic mask must be aligned manually by the operator before the exposure and this takes a long time and can introduce misalignment errors. Therefore it becomes necessary to search for a simpler, faster and more versatile manufacturing process.

3.2.1 Tip material

This thesis project aims to overcome these limitations and to create a tip chip composed of high-aspect-ratio and high sharpness tips. The material that has been chosen is silicon because silicon tips are cost-effective and very popular among AFM user. Silicon is a very well characterized material and the in-dept knowledge on the tip mechanical property is of fundamental importance for the sample characterization [48]. Moreover, within certain limits, silicon tips have the ability to withstand high pressures without fracturing or deforming [49].

3.2.2 Tip shape and dimensions

Tip base

As shown previously, the diamond tips made in the first prototype have been produced with a pyramidal shape obtained starting from a square base. In this project, however, a circular base has been chosen as the starting point. For the first attempts, four different diameter sizes ($4\mu m$, $6\mu m$, $8\mu m$, $10\mu m$) were selected in order to test the manufacturing process and subsequently decide which diameter is best suited for the purpose.

Tip shape

Once the base shape was selected, the tip profile was analyzed. Considering that the tip should have a high-aspect-ratio and a very small apex, two possible tip shapes have been considered: the first one is a simple conical shape while the second one is the sum of a cylindrical pillar with a sharp tip on the top. Both shapes would be acceptable to reach the final goal from a theoretical point of view. The choice of one of them over the other one will be determined during the manufacturing process, considering which of them will be more easily obtainable and which will give more promising results (reproducibility of manufacture, wear resistance, resistance to external factors such as collision and handling).

Tip height

In the previous section the importance of having high-aspect-ratio tips was highlighted. It is now necessary to quantify this aspect by focusing on the ideal height that the tip must have. To determine what the ideal tip height is, it is necessary to consider the context in which it will be used: it will be included in a tip chip and the sample, positioned on the cantilever, will have to be scanned on it. Frequently the cantilever and the sample are respectively $5\mu m$ and $2\mu m$ thick and the sample is fixed on the cantilever with a glue $1\mu m$ thick: so the sum of the cantilever, the glue and the sample thickness is about $8\mu m$. Usually the cantilever is inclined by 12 degrees with respect to the horizontal plane and the sample is positioned approximately at $2\mu m$ from its edge. The tip must have a height that allows the complete sample scan without the cantilever touching the tips substrate surface during the measurement. Figure 3.2 shows the scanning phase for two tips with different heights. As one can see, for tips with a height lower than $4\mu m$, the cantilever touches the ground during the measurement, therefore the minimum tip height that allows a correct measurement is $4\mu m$. However, another aspect must

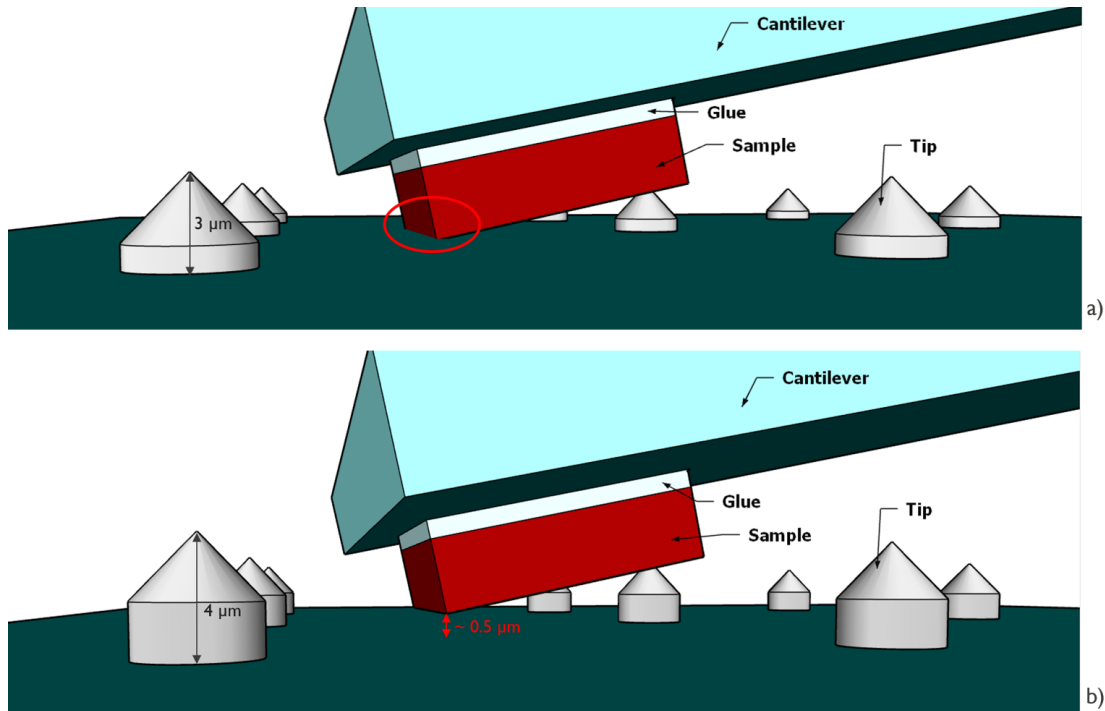


Figure 3.2: Tip chip composed by tips with different heights: a) The tips height is $3\mu m$, it is not sufficient to allow a complete sample scan. The cantilever impacts with the tip chip. b) The tips height is $4\mu m$, it is sufficient to obtain a complete sample scan without collisions. The minimum distance between the cantilever and the tip chip is about $0.5\mu m$.

be considered: the discussion made so far is valid from the theoretical point of view, it is possible that in reality the cantilever is inclined more than 12 degrees, that the sample is positioned more than $2\mu m$ from the cantilever edge or that the total thickness is greater than $8\mu m$. It is therefore necessary to work at a height greater than the minimum one, i.e. it is always necessary to add a safety margin. Thanks to these considerations in this project the ideal tips height is set in the range between $8\mu m$ and $10\mu m$.

Distance between tips

The last parameter to be fixed is the distance between the tips contained by the tip chip. Again, the distance must be sufficient to allow the tip to scan the entire sample without collision between the sample and the surrounding tips. Assuming that the sample has standard dimensions (i.e. $15\mu m$ wide, $15\mu m$ long and $2\mu m$ high) the minimum distance between two tips must at least be slightly larger than the width of the sample. Also in this case it is not recommended to work at the minimum distances as small variations of the dimensions considered would cause a malfunction of the system. For example, it may be that the cantilever is

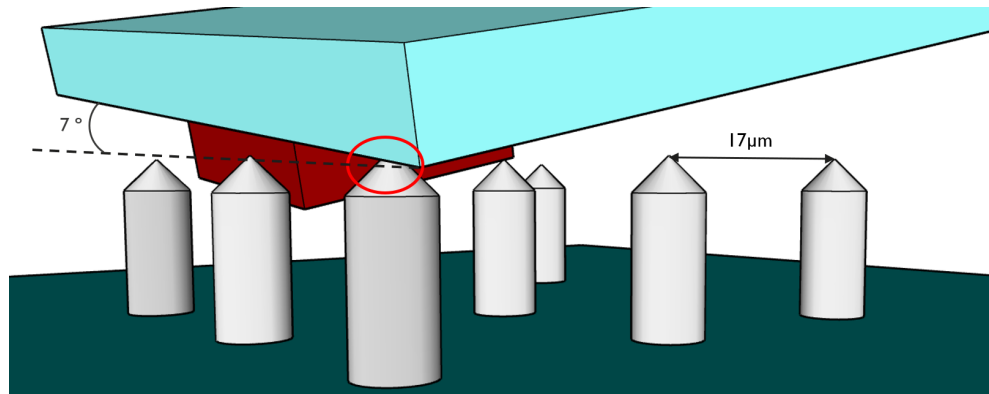


Figure 3.3: Cantilever 7° tilted: the distance between tips (set to $17\mu m$) is longer than the minimum distance but it is not enough. If the cantilever is a little bit tilted it could impact anyway with the neighbouring tips. For this reason it is reasonable to set the distance to $25\mu m$, i.e. one half of the cantilever width.

tilted slightly, if the distance between tips is $17\mu m$ (minimum distance necessary so that the sample does not come into contact with the other tips), the cantilever tilt would cause an impact between the cantilever and one of the neighboring tips during the measurement, as shown in figure 3.3. For this reason it is better to choose a wider distance between the tips. For a standard size cantilever ($200\mu m$ long, $50\mu m$ wide and $5\mu m$ thick) the best choice is to set a distance of $25\mu m$ between tips, that corresponds on one half of the cantilever width.

Another aspect to consider is the number of tips that can be reached in a single measurement. The major advantage of this reverse AFM configuration is the ability to easily change the tip during the measurement, therefore the higher is the number of tips that can be reached, the higher is the advantage of the new AFM configuration over the standard one. Considering the Dimension 3100 AFM used in this project, its stage can only move over an area of $50\mu m \times 50\mu m$ after engaging the sample to the probe. For this reason, if a distance of $25\mu m$ has been set between the tips, the maximum number of tips reachable during the measurement is nine. In order to have more tips available for each measurement, some changes can be introduced. If smaller samples (for example $10\mu m \times 10\mu m \times 2\mu m$) is used, it is possible to replace the standard cantilever with one with a smaller width ($20\mu m$ instead of $50\mu m$), so in this case it is possible to set the distance between the tips to $15\mu m$. In doing so, the tips that can be reached in each measurement are sixteen instead of nine.

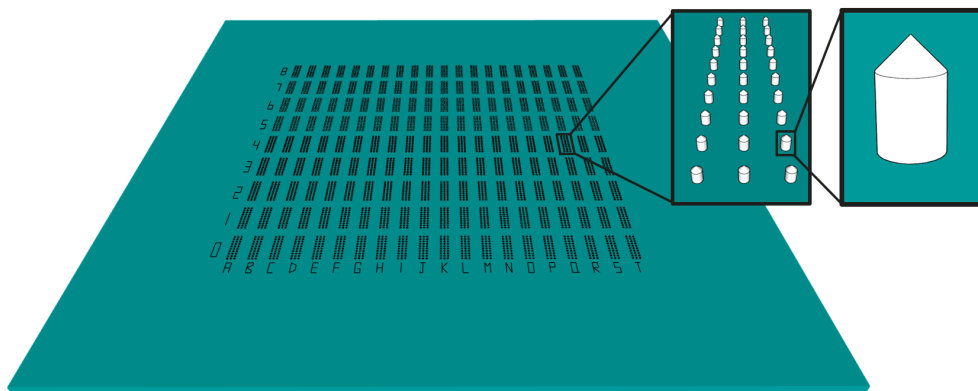


Figure 3.4: Tip chip example of structure: the chip is 5mm x 5mm wide and contains the tips in its central part. The tips are organized in 10 rows and 3 columns matrices, within each matrix the tips are $25\mu\text{m}$ apart. This chip contains 180 tip matrices, $100\mu\text{m}$ apart, organized in 9 rows and 20 columns. In total, therefore, it holds 5400 tips.

3.3 Mask design

In the previous section all the desired tip features have been analyzed. The following step consists in the design and realization of the first lithographic mask. In this project all the masks were designed with Cadence Virtuoso software. The lithographic mask will then be used during the exposure phase in order to transfer its geometry into the resist deposited on the wafer. Subsequently in the etching phase the resist geometry will be finally transferred to the substrate; therefore the mask geometry determines the resist geometry and consequently the substrate geometry. Obviously the first mask designed will not be the definitive one, because at the beginning of the experiment it is necessary to have many different structures with different dimensions on the mask; following the first results obtained during the etching phase, a new mask will be designed. Structures with different dimensions are necessary at the beginning as the etching phase parameters that will be used are not known yet and therefore it is not possible to choose the most suitable structure at this stage. Having many different structures allows to study the behavior of etching as the shape changes and it provides better information on how to adapt the parameters to reach the final goal.

The wafer that will be used to make the tip chips has a diameter of 4 inches and hence the mask must be a 5 inches square mask. Since the objective is to create a tip chip with the characteristics described in the previous section (an example is shown in figure 3.4), most of the mask surface will be composed of tip chip models with some small differences between them. A $5\text{mm} \times 5\text{mm}$ square chip was chosen for all tip chip models. The tips are contained in the central area of the chip (in some chips it is a $3\text{mm} \times 3\text{mm}$ square in others $2\text{mm} \times 2\text{mm}$) making it

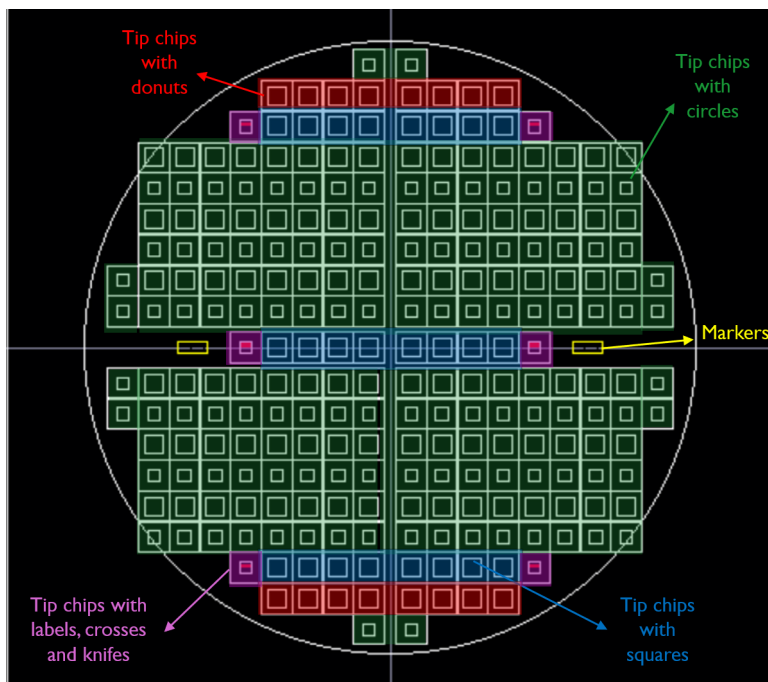


Figure 3.5: Five inches mask structure: the white circle in the middle represents the four inches wafer, it is not really present on the mask it is just an indicator to show the chips position. All the chips are $5mm \times 5mm$ squares and they host principally circular shapes (green chips). In order to better estimate the etching behaviour also chips containing other shapes are present: squares (blue) and donuts (red). The violet chips contain letters and numbers (with different dimensions in order to establish what are the most suitable as labels), crosses and knives.

possible to separate the chips (during the wafer cleaving step) without damaging the tips. Inside the chip the tips are organized in matrices; these matrices are made up of 10 rows and 3 columns, spaced $25\mu m$ or of 10 rows and 4 columns, spaced $15\mu m$. As described in the previous section, these two models are designed for two different cantilevers, one of standard size and one smaller one. The choice to divide the chip into matrices is given by the fact that in this way it is possible to recognize the tips during the measurement phase, in order to know which of them have already been used and which ones are still to be used. To further facilitate the recognition of the matrices, letters and numbers have also been inserted along the sides of the inner square as labelling. The matrices are spaced $100\mu m$ from each other. Depending on the parameters chosen, a chip of this type can host from about 2000 to about 10000 tips. Each tip chip variation described is present with $4\mu m$, $6\mu m$, $8\mu m$, $10\mu m$ diameter circles. In addition to tip chips composed of circular geometries, the mask also contains chips with square-based geometries and donuts shapes, crosses and knives to more carefully evaluate the behavior of the substrate when the etching parameters vary. Figure 3.5 shows the mask's final structure.

3.4 Fabrication process

Two different types of wafers were used as substrates in the fabrication process: $\langle 100 \rangle$ -oriented 4-inch silicon wafer and $\langle 100 \rangle$ -oriented 4-inch silicon wafer with 200 nm of thermally grown silicon oxide. The same spinning, exposing and developing parameters were used for both wafers. The first lithography step is the photoresist coating 3.6(1): a positive photoresist is poured onto the wafer which is then spun on a rotating plate at high speed. The wafer is then heated on a hot plate to dry and stabilize the previously deposited resist film. At this point the exposure phase takes place using a mask aligner: the 5-inch mask described in the previous paragraph is aligned with the wafer and both are exposed to UV light. In this step the mask geometry is transferred to the resist. Once exposed, the resist needs to be developed: the wafer is immersed into a developer and the part of the resist exposed to light, therefore not covered by the mask in the exposure phase, is removed 3.6(b). Finally, during the post-bake phase, the wafer is heated again at high temperatures on a hot plate in order to harden the resist image so that it can resist during the etching phase.

At this point the silicon wafer is ready while the silicon wafer with silicon oxide requires a further step: the geometry of the resist must be transferred to the silicon oxide. The silicon oxide is etched into BHF (buffered-HF) 3.6(3).

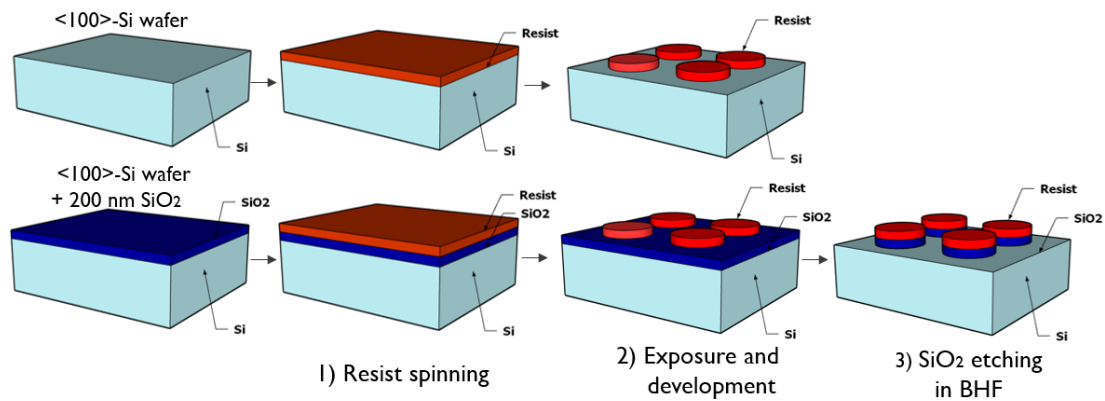


Figure 3.6: Sample fabrication process: $\langle 100 \rangle$ -oriented silicon wafer and $\langle 100 \rangle$ -oriented silicon wafer with 200 nm of silicon oxide were used as substrates for samples preparation. The first step (1) of the fabrication process is the resist spinning, followed by the exposure and development phases (2) in which the mask geometry is transferred to the resist layer. The silicon covered by silicon oxide wafer needs a further step to transfer the resist geometry to the oxide layer, this is done with an etching in BHF(3).

The next step in the tip chip manufacturing process is etching in which the exposed surface of the substrate, i.e. the part of the surface not covered by the mask, is progressively removed. It is the key step of this project and finding the right parameters, that allow the creation of the tips with the desired characteristics, is the real challenge. The etching processes are divided into two main categories: wet etching and dry etching. In the wet etching process, the wafer is immersed into a chemical bath in which some etchants are present that react with the surface of the substrate. In the dry etching process the etchants are in a gas or vapour phase and they are typically ionized. The advantages of the wet etching process are mainly the speed (high etching rate) and simplicity of the equipment: only a beaker and a hot plate are sufficient to make the process. However, it has many disadvantages. Wet etching is primarily an isotropic process, so etchants remove the material under the mask in the same way as the material in the bulk. Furthermore, it is inadequate for creating features size smaller than $1\mu m$ and there are also wafer contamination issue. Moreover, it requires the handling of dangerous acids and solvents. As for the dry etching process, it has the advantage of being completely automated, thus reducing the danger for handling chemicals and increasing the process control. Furthermore it has a high versatility, different gases can be used with different process settings allowing to adapt the process according to the needs; the operator can choose between anisotropic and isotropic etching changing the gasses parameters. With this type of process a features size of smaller than 100nm can be obtained. Another aspect to underline is that, while in wet etching the etching directionality was given by the crystallographic orientation of the substrate, in dry etching it is possible to carry out a directional etching that does not follow the crystallographic orientation. The disadvantage of the dry etching process is mainly in the equipment: it requires a specific and expensive tool with a vacuum chamber [50]. Moreover, some gases used can be toxic and corrosive and it may also occur that some non-volatile compounds are re-deposited on the substrate.

In this project both processes have been taken into consideration but the focus has been placed only on dry etching as it has a higher degree of freedom in the process parameters variation. Therefore, the following paragraphs will contain all the information regarding the tips manufacture using the dry etching process.

3.4.1 Dry etching

As mentioned above, dry etching is a process in which several gases can be used to remove material from the sample. It is usually done in the plasma phase in which reactive ions and free radicals (neutral molecules with incomplete bonding) are generated by electron bombardment and they are used to attack the wafer surface. In the plasma etching the free radicals, once generate, diffuse on the surface where they are absorbed. They than react with the wafer surface to etch away a surface layer materials. The products of these reactions must be volatile in order to be carried away by the gas stream.

A particular type of plasma etching is the reactive ion etching (RIE). Compared to plasma etching, which performs a chemical isotropic attack, in the RIE the positive ions are accelerated towards the surface, therefore a physical etching given by the ionic bombardment of the surface (sputtering) is also added to the chemical type etching (see figure 3.7). [51].

An Oxford Plasmalab 100 inductively coupled plasma (ICP) reactive ion etcher (RIE) has been used in this project [52]; it is shown in figure 3.8(a). In a generic reactive ion etcher the plasma is generated under low pressure by a strong RF electromagnetic field, the high-energy ions and the free radicals created are directed towards the wafer surface reacting with it. The plasma source is responsible for both ion density and energy. In an ICP-RIE etcher the plasma is generated instead with an RF powered magnetic field, in this case it is possible to decouple ion current and energy. The ICP-RIE reaction chamber is shown in figure 3.8(b).

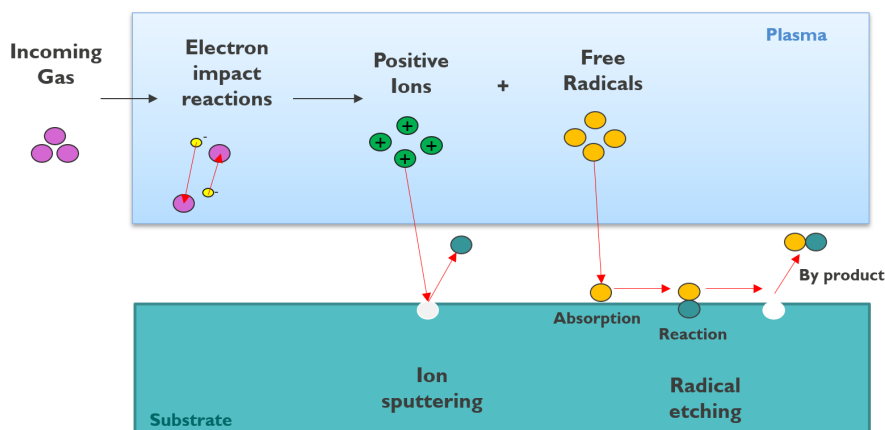


Figure 3.7: Reactive ion etching schematic figure: the etchant gases are inserted in the chamber; positive ions and free radicals are created. Positive ions are directed towards the substrate by a strong electric field causing the substrate sputtering. Free radicals are neutral particles, they are absorbed by the surface and react with it causing a chemical etching. The volatile by products are carried away by the gas stream.

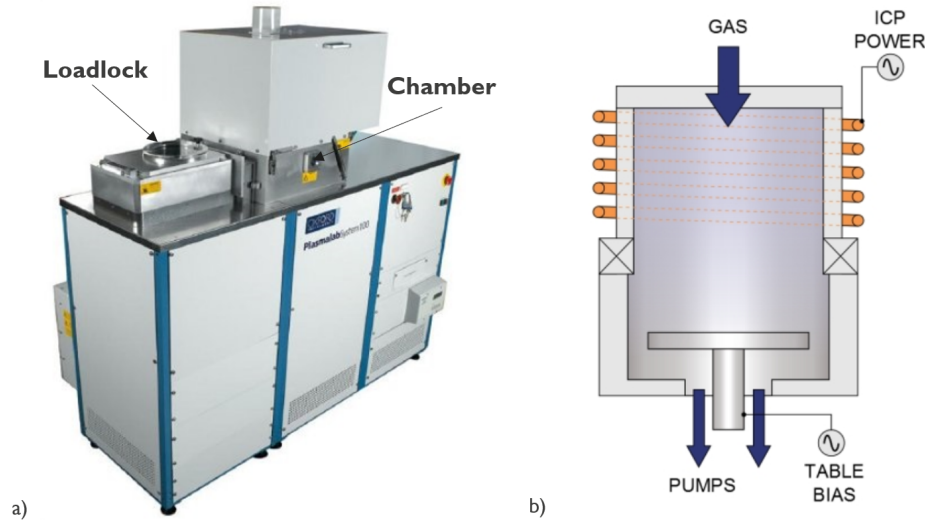


Figure 3.8: a) Picture of Oxford Plasmalab 100: sample loadlock is indicated on the left side. It can only hold 100mm wafers, if it is necessary to use smaller samples they need to be placed on a 100mm carrier wafer. [53]. b) ICP-RIE schematic figure: Two different RF power generators are present to control separately ion energy and ion density, ICP power is responsible to generate chemical species, RF power accelerates the ions towards the substrate.[52]

Dry etching parameters

- Gases selection: The choice of gases to be used during the process is made according to the type of material to be etched and the masking material. The substrate material must be very sensitive to the gas injected into the chamber while the latter must affect the mask as little as possible in order to obtain the maximum selectivity. This project is based on silicon substrates, using the silicon oxide or just the photoresist as a mask. Fluorine-based gases, such as SF_6 or CF_4 , have a high etching rate on silicon since fluorine is the halogen that reacts more effectively with silicon producing SiF_4 . The choice to use sulfur hexafluoride instead of carbon tetrachloride is due to the tool used limitations: CF_4 is not supported. In any case, SF_6 is a very good etchant gas. It is injected in the reactor and it is dissociated into reactive products such as F atoms, that are responsible of the high etch rate, and SF_x (with $x=1-5$) ions, which are accelerated towards the substrate provoking surface physical sputtering [54].

To obtain high-aspect-ratio structures, SF_6 cannot be used alone as it performs an almost isotropic etching and so the material under the mask would be consumed before reaching the desired height. For this reason it is also necessary to use a passivating gas that protects the sidewalls making the

etching more anisotropic. The passivation gas used is C_4F_8 and the process in which it is used is called Pseudo Bosch process. For a better understanding of the Pseudo Bosch process it is necessary to first explain how the Bosch process works. It is defined as a process that alternates two plasmas with different chemistry: the first plasma, C_4F_8 plasma in this case, generates polymers that are deposited on the sample surface protecting it from the incoming radicals (passivation phase), while the second plasma, i.e. the SF_6 plasma, it is used to etch silicon (etching phase). During the passivation phase the polymers (polimerized CF_2) are deposited equally on the entire surface of the sample but during the etching phase, thanks to the ion bombardment, the passivation carried out on horizontal surfaces is removed, in this way only the sidewalls are protected. The etcher switches between one process and another in few seconds, a faster switch allows less degradation of the side walls. The only disadvantage of this type of process is that during the etching phase the sidewalls are however slightly worn. This, following many cycles, produces a scalloping profile on the side walls of the silicon. The Pseudo Bosch process is used to avoid characteristic scalloping on the sidewalls. In it, passivation and etching occur simultaneously, it involves a continuous passivation of the sidewalls at the same time as etching along the vertical direction [51], [55], [56].

- Gas flow rates: SF_6 gas is fundamental in the realization of high-aspect-ratio structure as it is the source of the reactive chemical substances in the chamber. Given that as the SF_6 flow rate increases, the positive ions that can bombard the substrate and the free radicals that react with it will increase, it seems to be obvious that the increase in the SF_6 flow rate is directly proportional to the etching rate. This is partially true but when the density of the fluorine radicals increases, it can happen that the F ions collide with each other, also directing towards the sidewalls, leading to an isotropic etching. Therefore an excessive increase in the SF_6 flow rate becomes an obstacle to the etching process itself. Regarding the C_4F_8 gas, it is used to generate polymer materials that are deposited on the substrate protecting the side walls from etching. It affects the etching rate, the sidewalls angle and the sidewalls damage. In general, the higher the C_4F_8 flow rate, the greater will be the etching anisotropy, allowing the creation of structures with perfectly vertical sidewalls and without damage. By decreasing the value of the C_4F_8 flow rate, the anisotropy decreases and this result in a greater angle of inclination of the sidewalls. However, an

excessive increase in the C_4F_8 flow rate could form a protective layer that is too thick and it would take a long time for the F atoms to remove the passivation and to start etching the silicon [57]. In this project the SF_6 flow rate is predominantly kept constant while the C_4F_8 flow rate has been studied in a certain range.

- RF power and ICP power: The RF power is responsible for the ion bombardment on the substrate and therefore the degree of anisotropy of the etching. A high RF power value increases the ion kinetic energy by increasing ion sputtering. This can cause significant damage to the mask and the sidewalls and cause an excessive sample heating. However, a low value of RF power makes the ion bombardment negligible compared to chemical etching, the process is therefore almost isotropic. The ICP power controls the density of ionized atoms and therefore the generation of chemical species within the plasma [58].
- Pressure: In general, the pressure determines the density of the fluorine atoms and the energy of the ion flow. When a low pressure is used the ion flow is high (the ions do not encounter obstacles in their path) and the bombardment is intense but there are fewer fluorine radicals reacting with the substrate. On the other hand, if the pressure is high, the radicals are a sufficient number for the reactions with silicon but the ion bombardment is less effective as the ions collide many times before reaching the surface of the wafer.
- Temperature: the temperature is kept low to prevent damage to the mask, which in this case can also be just the photoresist.

Experimental research general information

The experimental part of this project has been divided into six sections called "set of experiments". Each set is characterized by a main objective and, in order to achieve this, a certain number of samples have been processed. Table 3.1 shows all the samples processed for each set of experiments. For each sample the wafer specifications were reported. As previously explained, two different types of wafers were used according to the needs: $\langle 100 \rangle$ -silicon wafer covered by a 200 nm silicon oxide layer and $\langle 100 \rangle$ -silicon wafer.

Samples	Set	Wafer specification
1-7	I	Wafer 1: <100>-silicon wafer + 200 nm silicon oxide
8-11	II	Wafer 1: <100>-silicon wafer + 200 nm silicon oxide
12-14	III	Wafer 1: <100>-silicon wafer + 200 nm silicon oxide
15	IV	Wafer 2: <100>-silicon wafer
16-19	IV	Wafer 3: <100>-silicon wafer
20-21	V	Wafer 4: <100>-silicon wafer
22-23	VI	Wafer 4: <100>-silicon wafer

Table 3.1: Samples general information

First set of experiments: etch rate

For the first etching tests, silicon samples coated with silicon oxide and resist as a mask were used. The samples were prepared by cleaving the wafer with a diamond pen after immersion in the BHF. Each sample is approximately 2cm x 2cm in size. In order to determine the etch rate, these tests were carried out keeping all the parameters fixed and varying the etching time. Samples with different diameters structures ($4\mu m$, $6\mu m$ and $8\mu m$) were tested in order to verify if the size of the mask affects the etch rate. After each run the samples were examined with SEM in order to obtain detailed pictures of the structures created, it is possible to see an example in figure 3.9. A list of the various samples used in this first phase with their run specifications is shown in table 3.2¹. The most relevant dimensions of the obtained structures in each sample are also reported. Sample 1 was the first sample to be etched in order to get the order of magnitude of the recipe's etch rate. The resulting structures, for a 11 minutes etching, are pillars about $2\mu m$ high. This result allows to estimate the etch rate at about $1.8\mu m$ each 10 minutes therefore the following samples have been etched for much longer times.

As previously explained the etcher can only host 100mm wafers therefore the samples were placed on a carrier wafer for etching. Two techniques were tried to fix the samples to the carrier wafer: the use of a double sided tape and the use of a thermal paste. In order to verify the differences between these two methodologies samples 2 and 3 were etched with the same recipe but sample 2 was glued to the carrier wafer with tape and the sample 3 with thermal paste. As can be seen from the results of table, sample 2 presents structures with greater etch depth and with the mask slightly more affected than sample 3. These differences are

¹All the measurements reported in this project tables were taken manually by the author using a dedicated software for SEM images. The measurement uncertainty is not reported as it is mainly due to the limited resolving power of the human eye and for this reason it is difficult to estimate. Therefore, please consider the measurements contained in this project as indicative.

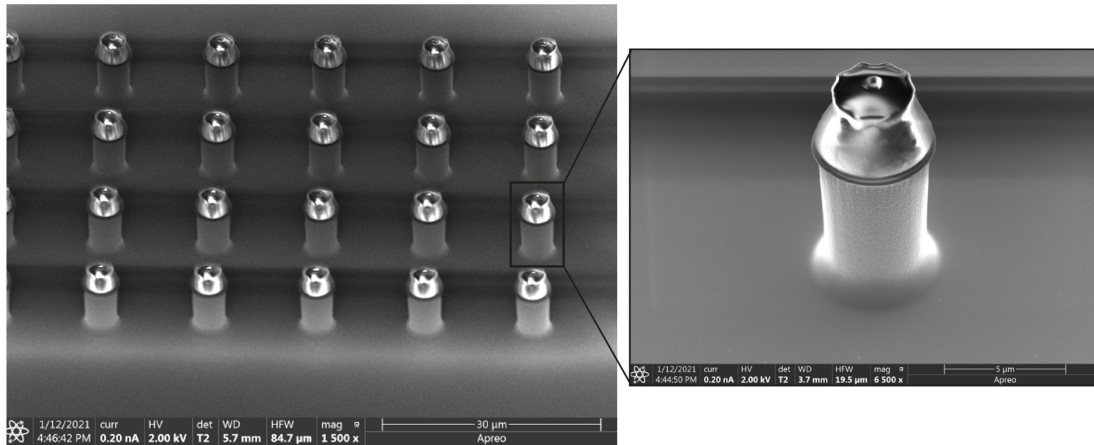


Figure 3.9: This figure shows two SEM images of sample 5 in order to show the structure formed with the starting recipe after an etching of 60 minutes. In this case the size of the starting mask is $6 \mu m$ and the reached etch depth is $7.1 \mu m$. As it is possible to see in the pictures, this type of recipe is purely anisotropic in fact there is no mask underetching, the final structure is a pillar of constant diameter along its entire height.

not very significant, furthermore, the thermal paste is more difficult to remove after the etching than the tape and there is a risk that the thermal paste residues contaminate the sample. Therefore the tape was used for the following samples.

Now, consider samples 1, 3, 4, 5, 6 and 7. These samples have been etched with the same recipe and in the same conditions. The only difference is the etching time. Generally, the shape of the structures obtained is almost the same of that shown in figure 3.9: cylindrical shape pillars with a diameter very close to the mask one. As one can see, the mask, in this case composed of the oxide and the resist, is still present and it has not been strongly affected by etching. This shows that the recipe used has a fairly high selectivity. Mask underetching is not present, the recipe used has a completely anisotropic behaviour. Accordingly, with these particular gas flow rates, it is possible to obtain very high-aspect-ratio structures but some changes will be needed in order to obtain a very small apex on the top

	Etch time	Mask diameter	Pillar height	Pillar diameter
Sample 1	11 min	$8 \mu m$	$2 \mu m$	$7.4 \mu m$
Sample 2	60 min	$4 \mu m$	$7.4 \mu m$	$2.4 \mu m$
Sample 3	60 min	$4 \mu m$	$6.9 \mu m$	$2.5 \mu m$
Sample 4	90 min	$4 \mu m$	$9.2 \mu m$	$2.2 \mu m$
Sample 5	60 min	$6 \mu m$	$7.1 \mu m$	$4.3 \mu m$
Sample 6	75 min	$6 \mu m$	$8.2 \mu m$	$4.0 \mu m$
Sample 7	90 min	$8 \mu m$	$10.8 \mu m$	$6.0 \mu m$

Table 3.2: Summary table containing information of the first set of experiments

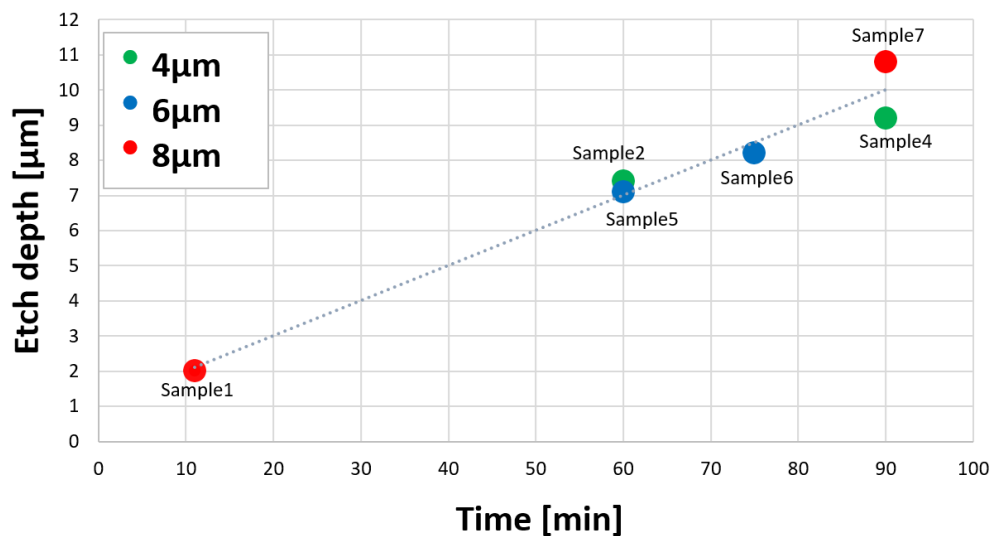


Figure 3.10: The etch depth of samples 1, 2, 4, 5, 6 and 7 is reported in function of the etching time. Each sample is represented by a dot, the dot color indicates the mask diameter size. The dotted line is the points linear interpolation and indicates the function trend.

of the structures.

Regarding the etch depth, during this first sequence of experiments, it is possible to affirm that the pillars height increases almost linearly with the etching time. In graph 3.10 the samples etch depths are reported in function of the etching time (except for sample 3 which, having been etched in different conditions with respect to the others, was left out of the analysis). As can be seen, an etching time of 70-90 minutes is needed for having 8-10 μm high structures.

Second set of experiments: tip tapering

The recipe analyzed in the previous paragraph allows to obtain structures with the desired height but their shape must be modified. Consequently, the next step consists in tuning the recipe parameters in order to obtain structures that not only have the right height but also the wanted shape.

In this second sequence of experiments, the studied parameter is the C_4F_8 flow rate. As previously mentioned, this gas was added in order to protect the sidewalls from SF_6 attack. Therefore, the purpose of this study is to understand how a decrease in the C_4F_8 flow rate, and hence a decrease of passivation degree, can affect the final shape of the structures.

In this phase, three samples were initially considered (samples 8, 9 and 10), which had the same initial conditions: mask composed of silicon oxide and resist with a diameter of 10 μm . All three underwent a 30-minute etching in which the

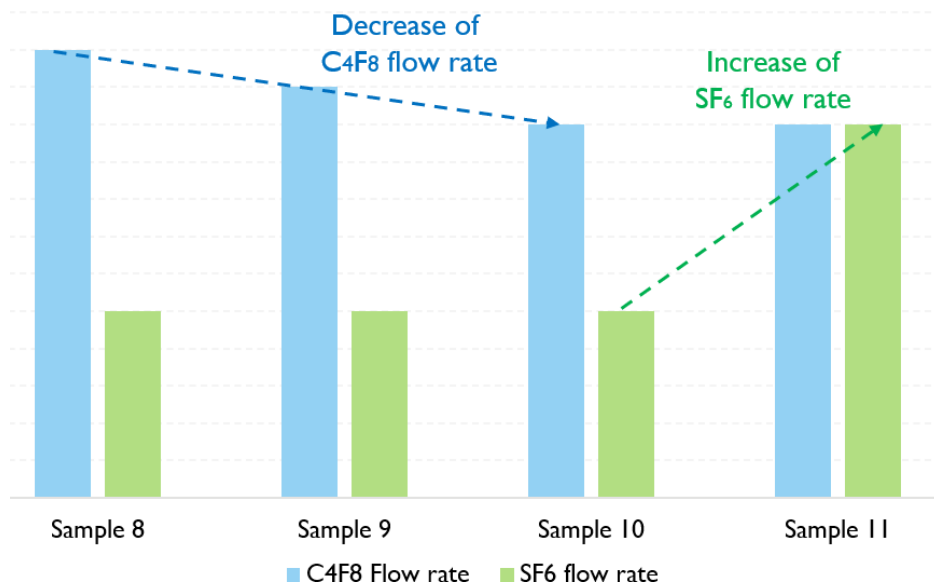


Figure 3.11: Schematic trend on the gas flow rates in samples 8, 9, 10 and 11.

	Height	Slope	Mask underetching
Sample 8	$4.1\mu m$	11°	$0.3\mu m$
Sample 9	$4.9\mu m$	13°	$0.4\mu m$
Sample 10	$5.3\mu m$	21°	$0.5\mu m$
Sample 11	$6.9\mu m$	23°	$0.9\mu m$

Table 3.3: Summary table containing information of the second set of experiments

SF_6 flow rate was maintained constant while the flow rate of C_4F_8 was progressively decreased, as shown in figure 3.1. The shapes of the structures obtained are shown in figures 3.12(a), 3.12(b) and 3.12(c). Table 3.3 shows the most relevant information of each sample, that are the height, the slope of the sidewalls and how much the mask has been underetched. As one can see, a decrease in passivation causes a slight increase in etch depth and in sidewalls slope (angle formed by the sidewalls with respect to the vertical direction). This happens because the passivating layer thickness decreases with the passivating gas flow rate. A thinner passivation layer on the ground is easily destroyed by the ion bombardment, allowing a deeper etching. Instead, a thinner passivation layer on the sidewalls is faster consumed by the SF_6 , causing more tapered structures. As for the mask underetching value, it corresponds to how much material under the mask has been removed. Again, less passivation causes greater material removal and therefore higher mask underetching value. It has been shown that a decrease in the C_4F_8 flow rate makes the pillar more tapered. The choice not to test values of C_4F_8 flow rate further lower is given by the fact that passivation is a key element in the cre-

ation of high-aspect-ratio structures, therefore a further decrease in passivation to increase tapering would affect the possibility of obtaining high-aspect-ratio tips.

A different attempt was made with sample 11. It was etched with the same C_4F_8 flow rate as sample 10 but the SF_6 flow rate was increased (see figure 3.11). As shown in figure 3.12(d) and in table 3.3, an increase of etchant gas causes the same effects as a decrease of the passivation, in fact a comparison between sample 10 and 11 shows that the etch depth and the slope are greater in the sample with higher SF_6 flow rate. The drawback is that a greater amount of SF_6 damages the sidewalls.

In conclusion, this set of experiments showed that in order to obtain more tapered structures one must to decrease the C_4F_8 flow rate value while it is not recommended to further increase the SF_6 flow rate. In the following experiments the aim will be to try to combine the information obtained on the etch rate and on the sidewalls slope to obtain tips with high-aspect-ratio and high sharpness.

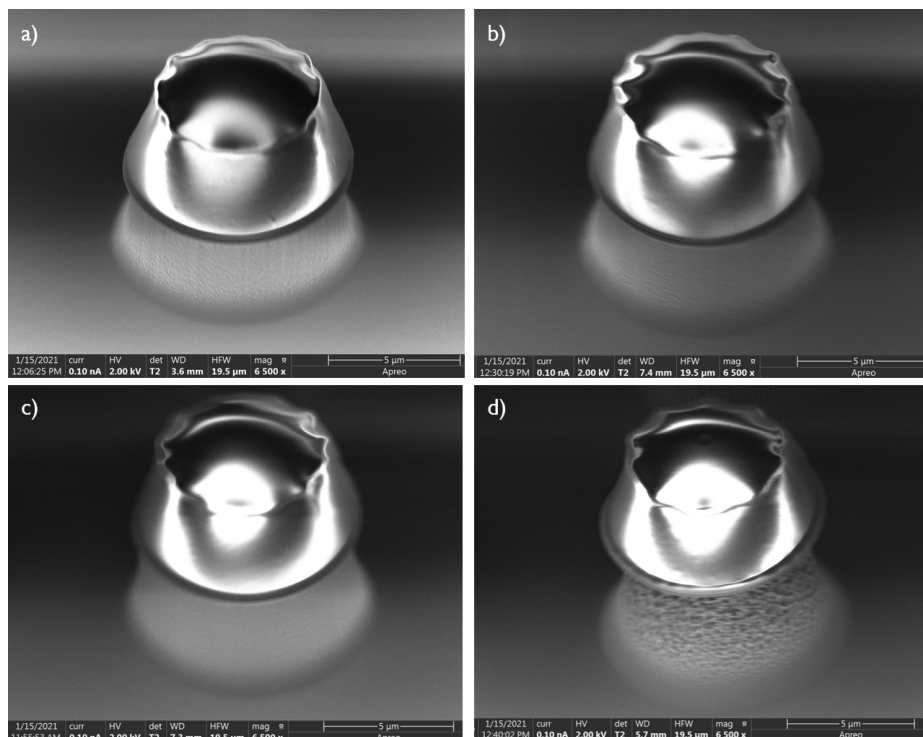


Figure 3.12: SEM images of the structures obtained after a 30-minutes etching with a $10 \mu m$ mask. The C_4F_8 and SF_6 flow rates are been varied to analyze the tip tapering. The samples specifications are contained in table 3.3. In particular the samples shown are: sample 8(a) , sample 9 (b), sample 10 (c) and sample 11 (d).

Third set of experiments: looking for the right shape

In the previous experiments the etch rate was evaluated and it was shown that a decrease of the C_4F_8 flow rate causes more tapered structures. In this third set of experiments the aim is to combine the information obtained to reach the right tip shape. Three samples (samples 12, 13 and 14) with the same initial conditions (silicon oxide and resist mask with a diameter of $4\mu m$) were etched with different recipes. In order to obtain about $10\mu m$ tall tips the overall etch time was set to 90 minutes for all samples. Mainly two recipes were been used in this part. They have the the same parameters except for the C_4F_8 flow rate. For convenience, the recipe with a higher C_4F_8 flow rate value, used in the first set of experiments, will be called "standard recipe" while the one with lower C_4F_8 flow rate value, used previously for sample 10, will be called "less passivating recipe". The details for each sample are listed in table 3.4.

Sample 12 was prepared using first the standard recipe for one hour in order to create about $7\mu m$ high pillars, followed by 30 minutes of the less passivating recipe to further increase the pillars height and make their upper end thinner crating a conical shape tips. Figure 3.13(a) shows a SEM image of one of the structure obtained with this recipe. Differently to what might have been expected, the resulted structure consists in a pointing down conical shape tip. The tip height is $12.7\mu m$ and the tip sharpness is high. Furthermore, in many cases, the base of the tip has become so thin that the structure has broken off, as shown in figure 3.13(b). To try to mitigate the negative slope of the side walls, sample 13 was etched using first the less passivating recipe for 30 minutes and after the standard recipe for one hour. The idea was to create a small tapered structure first and subsequently to etch it vertically. Also in this case the obtained structure (shown in figure 3.13(c)) does not reflect the desired one even if the negative slope of the sidewalls has been reduced compared to the previous sample. As a last attempt for this set of experiments, sample 14 was prepared using the less passivating recipe for 90 minutes. The result is shown in figure 3.13(d). As can be seen in

	Recipe	Height	Smallest diam.
Sample 12	60 min standard recipe 30 min less passivating recipe	$12.7\mu m$	240nm
Sample 13	30 min less passivating recipe 60 min standard recipe	$12.8\mu m$	$1.1\mu m$
Sample 14	90 min less passivating recipe	$13.3\mu m$	520nm

Table 3.4: Summary table containing information of the third set of experiments

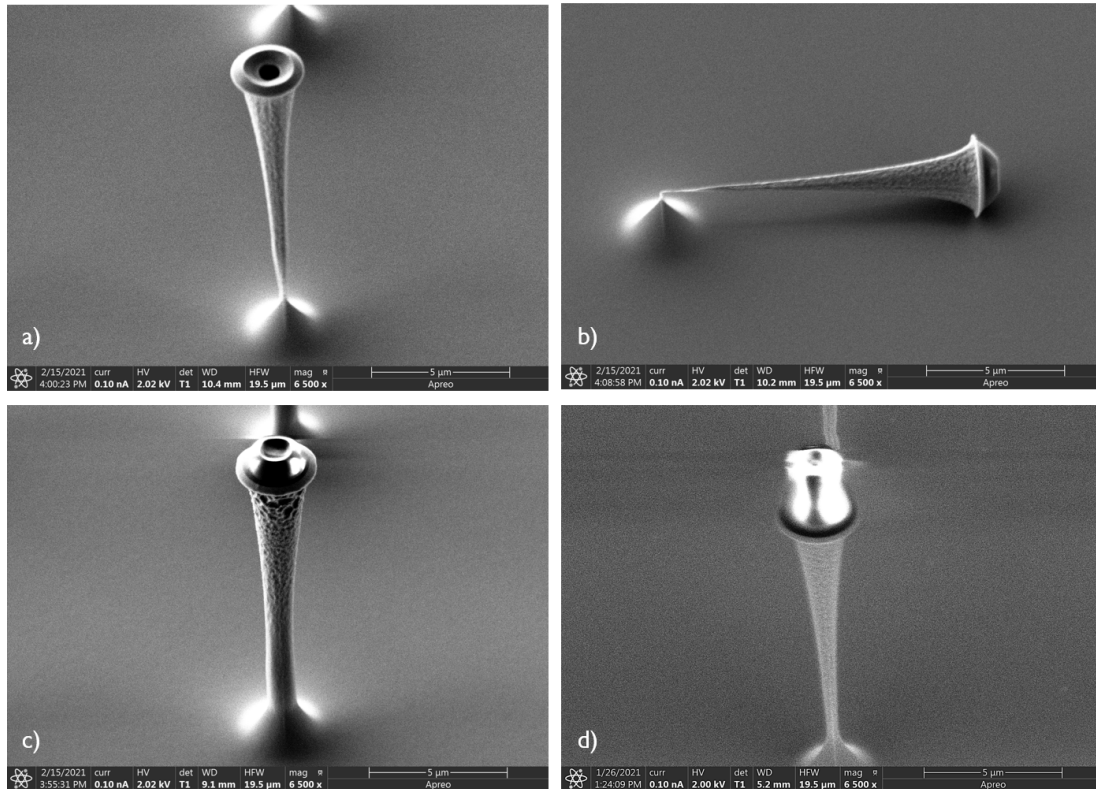


Figure 3.13: SEM images of the structures obtained after a 90-minutes etching with a $4\mu\text{m}$ mask. The recipes used are described in table 3.13 and consist of a combination between the standard recipe and the less passivating one. In particular the samples shown are: sample 12 (a)(b), sample 13 (c) and sample 14 (d).

this case the shape is conical with the tip turned downwards.

A possible explanation could be that during etching the reactions do not take place equally in every point, the mask could have acted as an "umbrella" to the reactants by repairing more the region immediately below it and directing the flow of reactants towards the base of the tip. A similar result, with which it is possible to make a comparison, has been reported in literature [59]. In this paper it is shown that the slope of the sidewalls depends on the percentage ratio between the flow rate of the etchant gas (SF_6) and that of the passivating agent (C_4F_8). If this ratio is greater than 33% the final structure will have sidewalls with a negative slope and as this ratio increases, the negative slope increases. As for the recipes used in this set of experiments, the percentage ratio of the flow rates is greater than 33% for both the recipes, therefore the structures obtained are in agreement with the literature.

In the light of these results, it might seem that if with a percentage ratio of the flow rates greater than 33% a negative slope of the sidewalls is obtained then by decreasing the value of this ratio, that is by decreasing the flow rate by SF_6 , sidewalls with positive slope can be obtained, such as require the specifications of

this project. This is true and it is proven in the literature [60]. The problem is that in doing so the percentage of SF_6 is too low compared to the passivation therefore there is no mask underetching. The sidewalls will form a truncated cone-shaped structure with the mask, making it impossible to form a high sharpness tip. For this reason the SF_6 flow rate will not be decreased in this project.

In conclusion, in this set of experiments, it was shown that the combination of recipes with different degrees of passivation is not sufficient to obtain tips with a conical shape facing upwards. Probably the $4\mu m$ mask is large enough to perturb the reactive gasses flow, affecting the etching and therefore the shape of the tips, this not allows a positive slope of the sidewalls.

At this point a different approach has been developed, it consist in trying to obtain the desired shape in several etching steps instead of just one. More details will be given in the following paragraphs.

Fourth set of experiments: new approach

In the first three sets of experiments the structures were obtained by means of a single etching step. In this way it was possible to find the right combination of parameters to reach the desired structures height but the correct shape was not obtained. In order to achieve the desired tip shape a new approach was tested. It consists of replacing the single phase etching with several etching steps, as shown in figure 3.14. Initially the pillar is created with a 60-minute etching, then the mask on the top of the pillar is reduced in diameter and at this point a second etching step is performed in order to create a sharpened tip in top of the pillar. At the end of the process the remained mask will be removed.

The resist mask, unlike the silicon oxide mask, can be easily reduced in size

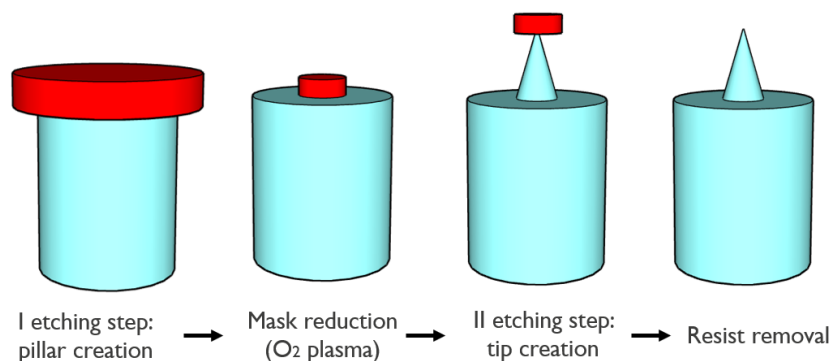


Figure 3.14: Two etching step approach schematic figure: first a pillar is created with 60min-standard recipe, afterwards the mask dimensions are reduced with O_2 plasma and another etching step is performed to created a small tip on the pillar top. If the resist mask is still present it is stripped away with O_2 plasma.

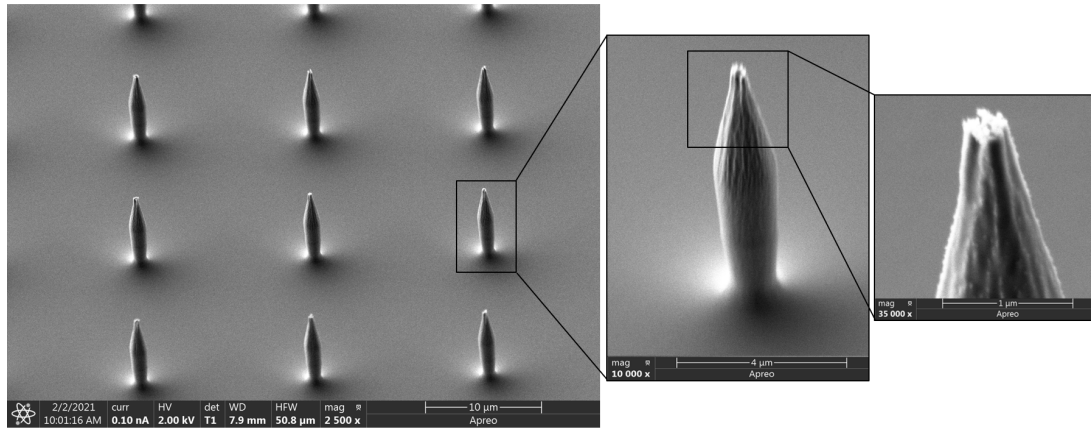


Figure 3.15: Sample 15 SEM images: first promising tips obtained. They are $8.2\mu\text{m}$ high and have a smaller diameter of 250nm . The detailed process information are reported in table 3.5

through an oxygen plasma etching. Furthermore the performances of the resist mask compared to the double layer mask (silicon oxide and resist mask used in all previous experiments) were evaluated: new samples with only the resist mask were subjected to the same etching as the samples used in the first three sets of experiments giving similar results in terms of shape, etch rate and structure height. In light of these facts, the replacement of the double layer mask with the resist mask only does not involve a clear degradation of the quality of the final result. For this reasons, from this point on, silicon samples with only the resist mask will be used.

As for the creation of the initial pillar, both recipes were tested to verify which of the two give the best result. The size reduction of the resist mask and the final resist removal were carried out by means of oxygen stripping tool. As for the tip, different combinations of the two recipes were tested in order to obtain maximum tip sharpness. Thanks to the use of this new method, the first promising results has been obtained. Figure 3.15 shows some SEM images of sample 15 (the detailed sample information are contained in table); it has been subjected to 60 minutes etching with the less passivating recipe to create the pillar, then the mask has been reduced with 60 minutes of oxygen plasma and the tip has been created through 30 minutes etching with the standard recipe.

At this point, once the first tip prototype was obtained, the focus was placed on two fundamental aspects: firstly check if the recipe used guarantees a certain reproducibility of the final result and secondly try to understand how to change the parameters of the recipe used to improve the sharpness of the tip. Some changes aimed to improve the tip sharpness will be analyzed in the next paragraphs while concerning the reproducibility some considerations can be made. Three samples

	Recipe	Height	Top diam.	Mask shape
Sample 15	60 min less passivating recipe 60 min oxygen plasma 30 min standard recipe	$8.2\mu m$	250nm	circle
Sample 16	60 min less passivating recipe 60 min oxygen plasma 30 min standard recipe	$8.2\mu m$	800nm	circle
Sample 17	60 min less passivating recipe 60 min oxygen plasma 30 min standard recipe	$8.8\mu m$	$1.3\mu m$	circle
Sample 18	60 min less passivating recipe 60 min oxygen plasma 30 min standard recipe	$5.9\mu m$	$1.5\mu m$	circle
Sample 19	60 min less passivating recipe 60 min oxygen plasma 30 min standard recipe 10 min less passivating recipe	$6.6\mu m$	40nm	square

Table 3.5: Summary table containing information of the fourth set of experiments

(16, 17 and 18) have been prepared with the same recipe parameters, their final shape have been inspected with SEM (see figure 3.16). Note that although the etching parameters used are the same, the structures have some differences and above all they deviate from the tip shape of the sample 15. This result denotes a poor reproducibility of the recipe which can be attributed to three main factors:

- Sample 15 belongs to wafer 2 while samples 16, 17 and 18 belong to wafer 3 (as can be seen in table 3.1). It is possible that the resist layers deposited on the two wafers during the spin coating phase had two slightly different thicknesses, this would have led to a difference in the resist shape after the O_2 plasma and therefore a different shape of the tip on the pillar.
- In general the spin coating phase can involve a non-uniform distribution of the resist along the surface of the wafer, it is possible that some samples have a thicker resist than others depending on their position in the wafer. This would explain the different behavior of samples 16, 17 and 18 despite being derived from the same wafer.
- Finally, the problem could derive from the etching phase. It is possible that inside the chamber of the etching tool there are small fluctuations in the parameters, this would result in a dependence of the resist shape on the sample position inside the chamber.

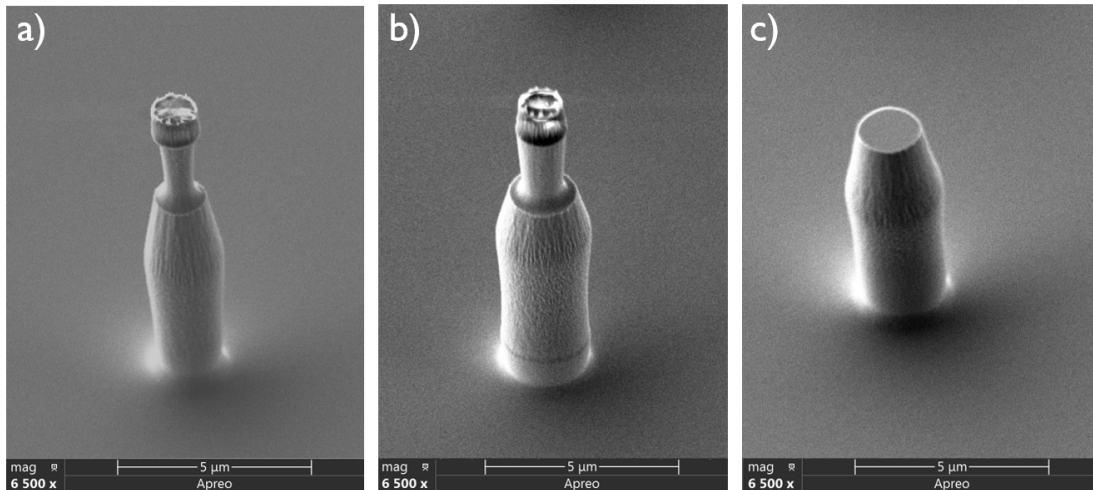


Figure 3.16: SEM images of (a) sample 16, (b) sample 17 and (c) sample 18. The detailed processes information are reported in table 3.5. Although the same etching parameters were used, there are differences between the samples. This means that the reproducibility of the recipe is poor.

The process reproducibility is an important feature to be taken into consideration during the fabrication phase of any prototype. In this project there have often been problems of non-reproducibility of the processes used. They can be solved using more sophisticated tools that ensure greater control of each process to which the sample is subjected. However, the aim of this project is to create the first prototypes so that their characteristics and performance are evaluated. Once established which prototype best reflects the requests, then all the parameters used in each step will be optimized so as to ensure good reproducibility of the product.

In any case, the recipe used for these samples has led to good results for circular masks, therefore it was decided to test it, with a small change, also on a sample having a square mask with a side of $4\mu m$ (sample 19). The change consists in adding an additional 10 minute etching step to the recipe in order to obtain a smaller top tip diameter and therefore a tip with higher sharpness. The less passivating recipe was used for the last 10 minute etching step. Figure 3.17 shows some SEM images of the obtained structure. As one can see, the result is very good. The tip is sharp and has a top diameter of about $40nm$. The height is $6.6\mu m$, it is lower than the desired height but still this result constitutes a good starting point in the creation of high-aspect-ratio and high sharpness tips with a square base. This means that beside a circular bases, even square bases can be suitable to manufacture this type of tips.

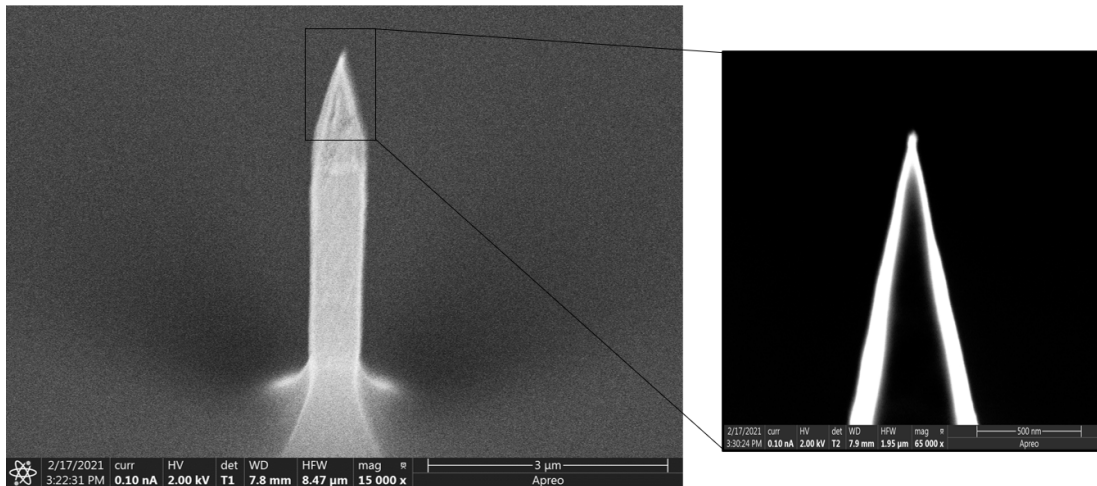


Figure 3.17: Sample 19 SEM images: tip realized starting from a square mask with a side of $4\mu\text{m}$. The height reached is $6.6\mu\text{m}$ and the top diameter is 40nm . The detailed process information are reported in table 3.5.

Fifth set of experiments: refine the tip features

In the previous paragraph it has been shown that with the right combination of recipe parameters it is possible to obtain tips with the shape and characteristics similar to those desired. Sample 15 has tips with the right aspect ratio but with a top diameter still too large, while sample 19 has a high sharpness but its height was not high enough. In this set of experiments the aim is to further optimize the process in order to further refine the tips features.

To achieve this aim it was necessary to study in depth the behavior of the resist: how it appears after the first etching step and how its dimensions vary during the oxygen plasma phase. To better appreciate this aspect a new lithographic mask has been designed. It is designed to create $5\text{mm} \times 5\text{mm}$ chips that contain the tips, organized in matrices in their central part, exactly as in the previous lithographic mask. The difference is that the first mask contained chips with different features (some chips contained circular structures, others contained square structures and the dimensions of the structures were also different, chips with circular structures of $4\mu\text{m}$, $6\mu\text{m}$, $8\mu\text{m}$ and $10\mu\text{m}$ were present) but the structures contained in each chip were all the same, while the new mask contains the same chip everywhere but is composed of structures with different characteristics. In particular, each chip of the second mask is formed by circular structures with different diameters. The matrices belonging to the first column have structures with a diameter of $4\mu\text{m}$, those of the second column have structures with a diameter of $5\mu\text{m}$ and so on up to a diameter of $20\mu\text{m}$ in the seventeenth column. The last three columns (18^{th} , 19^{th} and 20^{th}) contain structures of $25\mu\text{m}$, $30\mu\text{m}$ and $35\mu\text{m}$

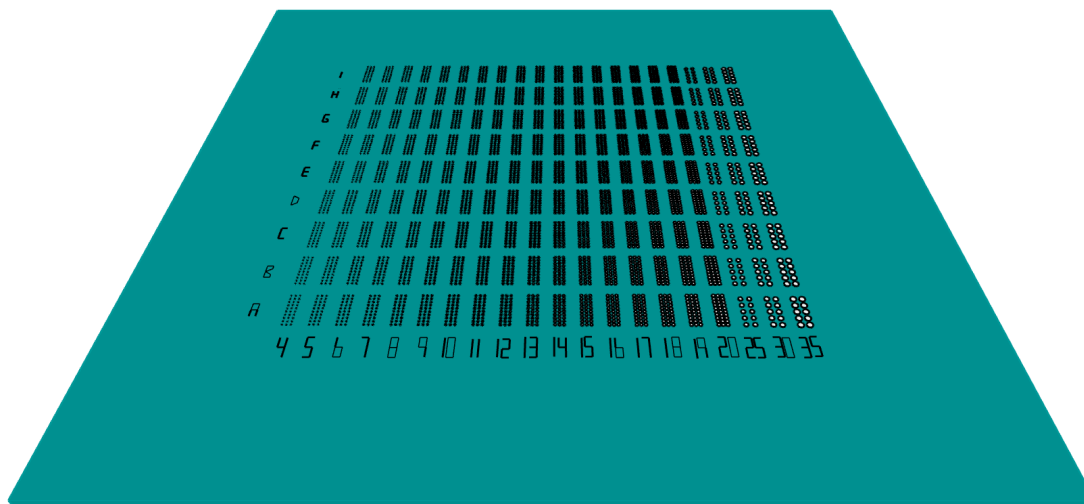


Figure 3.18: Chip obtained with the 2nd lithography mask schematic figure: the chip is 5mm x 5 mm and contains structures in its inner part (3 mm x 3 mm). Tips are organized in matrices and the matrices belonging to the same column are composed by circular mask with the same diameter. The diameters of the structures range from $4\mu\text{m}$ to $20\mu\text{m}$. Diameters of $25\mu\text{m}$, $30\mu\text{m}$ and $35\mu\text{m}$ have also been inserted, they can be used to create tips through wet etching.

in diameter respectively. Figure 3.18 shows a model of the chip obtained with the new mask, also in this case the numbers and letters are used as labels, the numbers correspond to the diameter size of the structures present in that column. This labeling facilitates the chip inspection phase.

It was decided to design this new mask because it allows to have all the variations in each chip and therefore makes it possible to evaluate how each parameter change affects structures of different diameters. Moreover, in this way it is possible to make comparisons in a more consistent way: two structures with different diameters that are positioned very close to each other can be compared and therefore it is assumed that the process parameters are exactly the same for both. To compare two structures with different diameters with the previous mask, it was necessary to take them from two chips that could also be very distant from each other within the sample. In this way it was difficult to assess how much their differences were to be attributed to the fluctuation of the process parameters and how much to the diversity of the diameter of the structures.

As mentioned earlier, in this set of experiments the aim is to further adapt the process parameters to achieve greater tip sharpness. To do this, it was decided to first study the behavior of the resist after the oxygen plasma step. Two samples (samples 20 and 21) were used in this phase. They were simultaneously etched for 60 minutes with the standard recipe followed by 60 minutes of oxygen plasma. In both samples the structures with diameters ranging from $4\mu\text{m}$ to $8\mu\text{m}$ belonging

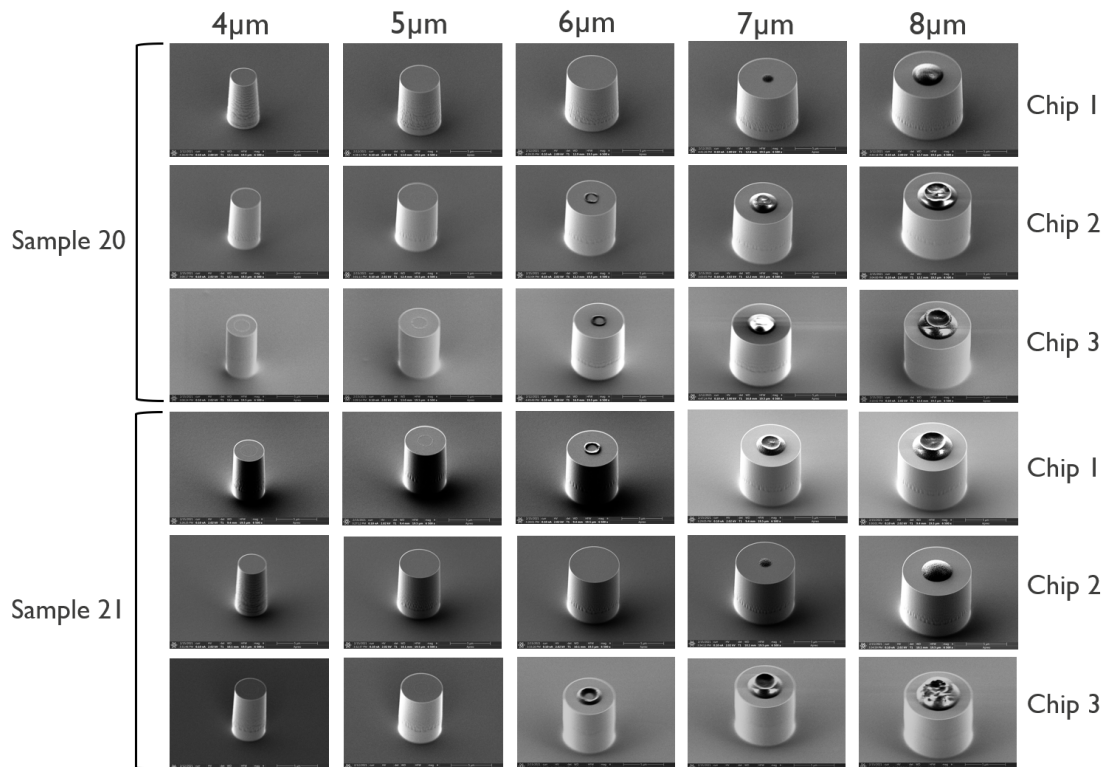


Figure 3.19: SEM images of structures belonging to three different chips of sample 20 and 21. Both samples have been subjected to 60 minutes etching with standard recipe and 60 minutes oxygen plasma. The structures diameters range from $4\mu m$ to $8\mu m$.

to three different chips were analyzed. In this way it is possible to evaluate both the variation of the resist profile depending on the diameter of the pillar and how much the fluctuations of the process parameters can lead to different results. Figure 3.19 shows the SEM images of all the structures analyzed. The first thing that becomes clear is that the resist profile has differences not only between structures belonging to different samples but also between structures belonging to different chips in the same sample. This result confirms what was previously hypothesized: given a structure, its position in the wafer during spin coating and its position within the etching chamber substantially influence its final profile. Now let's consider the variation of the resist sizes according to the pillar diameter. In all chips, the resist is almost completely absent (except for small remnants in some cases) in structures with a diameter of $4\mu m$ and $5\mu m$. In structures with a diameter of $6\mu m$ the resist is still present in four out of six chips and it has a donuts shape. For the structures with a diameter of $7\mu m$ and $8\mu m$ the resist is always present and it has a cylindrical shape (with the internal part more worn) in almost all the chips, except in chip 1 of sample 20 and chip 2 of sample 21 in which the resist on the $7\mu m$ diameter pillars is almost completely stripped away except

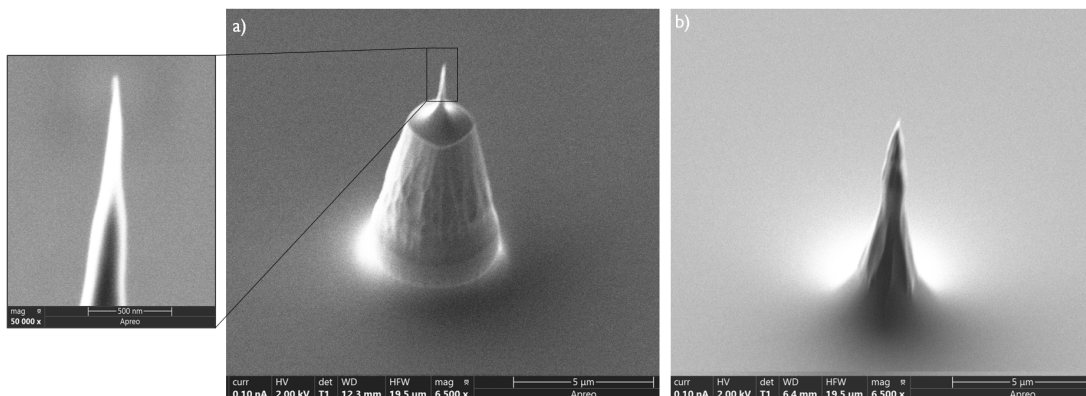


Figure 3.20: Sample 20 (a) and 21 (b) SEM images. Both tips are obtained starting from a $7\mu\text{m}$ diameter mask. Tip belonging to sample 21 is $9.8\mu\text{m}$ high and has a quite high sharpness. It has a conical shape probably due to a too long etching. Tip belonging to sample 20 is $11.2\mu\text{m}$ high and its top diameter is 30nm wide. It is formed by a pillar having a sharp tip on top.

for a small dot in the center. In light of these results it can be concluded that, in most cases, 60 minutes of oxygen plasma is too long to work with structures having diameter $4\mu\text{m}$ and $5\mu\text{m}$ (some exceptions may occur as has been shown for samples 15, 16 and 17). For these reasons, in the following experiments the behavior of the resist will be studied also after a shorter oxygen plasma.

At this point, the two analyzed samples were further processed. Sample 20 was processed with the same recipe as sample 19: after the 60 minutes of oxygen plasma it was subjected to a 30 minute etching with the standard recipe followed by a 10 minute etching with the less passivating recipe. Sample 21, on the other hand, in addition to the steps performed for sample 20, was further subjected to another 10 minutes etching with the less passivating recipe. The processes details are reported in table 3.6.

For both samples, the SEM images of the structures starting from a mask of

	Recipe	Mask	Height	Top diam.
Sample 20	60 min standard recipe 60 min oxygen plasma 30 min standard recipe 10 min less passivating recipe	$7\mu\text{m}$	$11.2\mu\text{m}$	30nm
Sample 21	60 min standard recipe 60 min oxygen plasma 30 min standard recipe 20 min less passivating recipe	$7\mu\text{m}$	$9.8\mu\text{m}$	80nm

Table 3.6: Summary table containing information of the fifth set of experiments

diameter $7\mu m$ were reported as they are the most interesting. Structures obtained from smaller diameters masks have been overetched producing too low structures, while larger diameters structures still have a cylindrical shape. Figure 3.20(b) shows a tip obtained in sample 21, it has a height of $9.8\mu m$ and has a quite high sharpness. Its height and the conical shape indicate that this structure has also been slightly overetched but still it has good features. Figure 3.20(a), on the other hand, shows a tip obtained from sample 20, made with the same recipe as sample 19. It has a height of $11.2\mu m$ and has a very high sharpness: the top diameter is 30nm. Its shape fully reflects the required tip features: it is made up of a resistant cylindrical pedestal surmounted by a very sharp tip. These results are excellent and the recipe used for sample 20 proved to be optimal for making tips starting from a circular mask of $7\mu m$. If one wants to further increase the tip aspect ratio it would be necessary to use a mask with a smaller diameter. For this reason the next experiments will be aimed at adapting this recipe to smaller mask diameters, in particular by reducing the time of the oxygen plasma phase.

Sixth set of experiments: increase of the tip aspect ratio

In the previous set of experiments the right combination of parameters that allow the creation of tips with a high sharpness and a high-aspect-ratio has been found. The recipe proved to be optimal for creating structures starting from a $7\mu m$ diameter circular mask. The aim of this further set of experiments is to adapt this recipe parameters to obtain tips with the same shape of the tip in figure 3.20(a) but starting with smaller diameters masks. To do this, it was necessary to study the behaviour of the resist shape according to the duration of the oxygen plasma phase. Two samples were prepared in this part: sample 22 and sample 23. Both were subjected to the first etching step (60 minutes of standard recipe) to create the pillars. Thereafter, they were subjected to 30 minutes and 50 minutes of plasma oxygen, respectively. The characteristics of the structures present on the two samples were compared with those of sample 20, which was subjected to 60 minutes of plasma oxygen. Figure 3.21 shows pillars contained in the three samples with a diameter ranging from $4\mu m$ to $8\mu m$. As hypothesized, the resist shape present on the pillars varies according to the duration of the oxygen plasma phase. Compared to sample 20, in which the resist has a cylindrical shape only in the pillars with a diameter greater than (or equal to) $7\mu m$, in samples 22 and 23 also the structures with diameter $6\mu m$ have a cylindrical resist on top. Regarding the pillar with a diameter of $5\mu m$, in sample 22 it is covered by a cylindrical shape resist while in sample 23 the resist has a donuts shape. For all the samples,

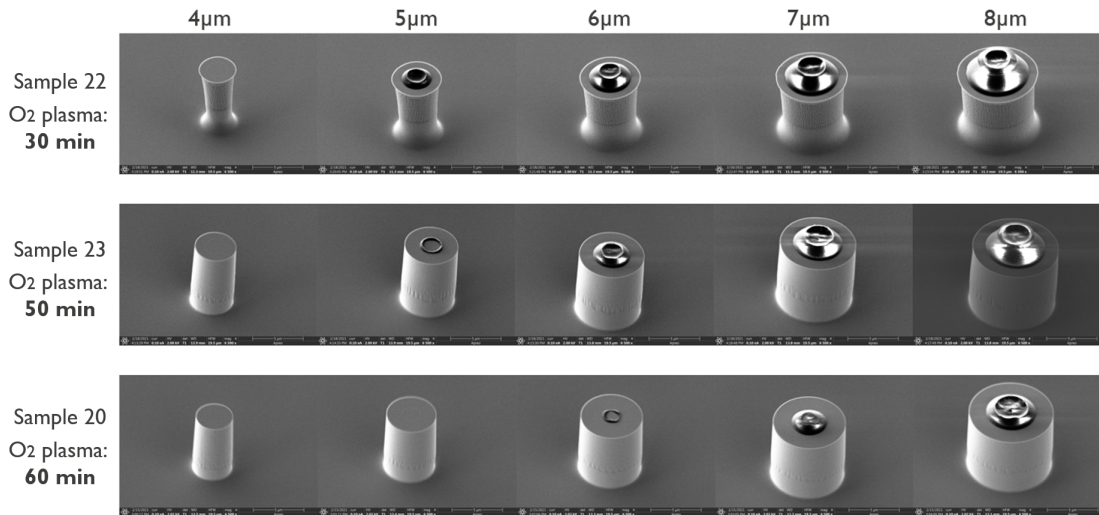


Figure 3.21: Oxygen plasma phase performed at different times: 30 minutes, 50 minutes and 60 minutes. The resist shape changes with the process duration.

in the pillar of diameter $4\mu m$ the resist is completely gone.

Let's now take as a reference the $7\mu m$ diameter pillar belonging to the sample 20, since the recipe used in the previous paragraph has brought good results for this type of pillars, and let's compare it with the resists present on the other samples. The resist on top of the reference pillar has a diameter of $3,5\mu m$ while the resist on top of the $6\mu m$ diameter pillars belonging to the samples 22 and 23 have $4,1\mu m$ and $3,7\mu m$ of diameter respectively. The similarity between the dimensions of the latter with the reference resist is high, therefore it was decided to further process samples 22 and 23 with 30 minutes etching with standard recipe followed by 10 minutes etching with less passivating recipe (same final steps used to obtain the tip on figure 3.20(a)). The processes details and the obtained structures sizes are listed in table 3.7. In figure 3.22 the tips created in the two samples, starting from a $6\mu m$ diameter mask, are shown. As it is possible to see, both tips have

	Recipe	Mask	Height	Top diam.
Sample 22	60 min standard recipe 30 min oxygen plasma 30 min standard recipe 10 min less passivating recipe	$6\mu m$	$8.7\mu m$	15nm
Sample 23	60 min standard recipe 50 min oxygen plasma 30 min standard recipe 10 min less passivating recipe	$6\mu m$	$9.5\mu m$	11nm

Table 3.7: Summary table containing information of the sixth set of experiments

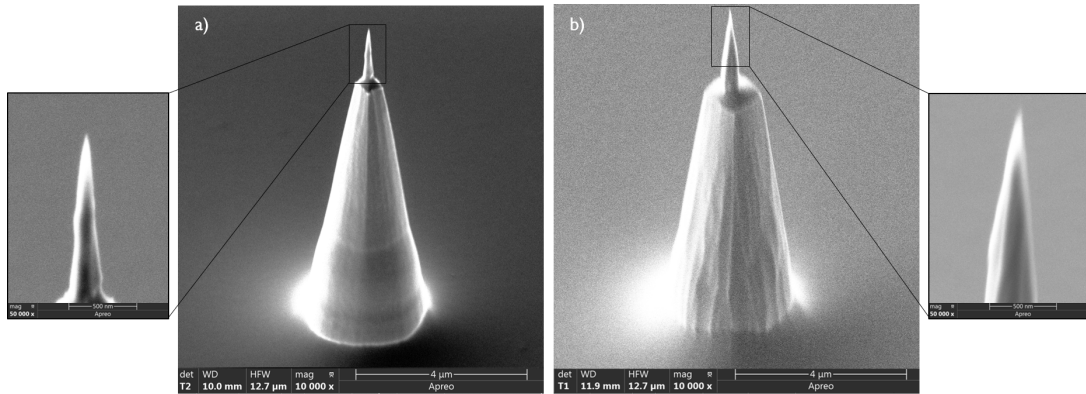


Figure 3.22: Sample 22 (a) and sample 23 (b) SEM images. The only difference between the recipes used to create these tips is the time of the oxygen plasma phase: in sample 22 (a) it was 30 minutes instead in the sample 23 (b) it was 50 minutes. Details about the tips sizes and recipes are contained in table 3.7.

a shape very similar to the tip in figure 3.20(a). The tip contained in sample 22 (3.22(a)) has a height of $8.7\mu\text{m}$ and a top diameter of 15nm while the tip created in sample 23 (3.22(b)) has a height of $9.5\mu\text{m}$ and a tip diameter of 11nm . These results verify the initial hypotheses. It is therefore possible to maintain the tip shape, obtained starting from a mask with a $7\mu\text{m}$ diameter, also with smaller diameters masks without loss in terms of quality of the obtained tip. In fact, the dimensions of the tips diameters obtained for these two samples are of the order of tens of nanometers (even less than those in the previous tips) and this means that the sharpness reached is very high. The only parameter to vary to move towards smaller base diameter structures is the duration of the oxygen plasma phase.

3.5 Conclusions

In this chapter, the fundamental steps that led to the first silicon tip chip prototypes have been analyzed in detail. Initially, the various tips geometric requirements were taken into consideration. The shape and diameter of the base of the tips, the measurement of their height and the distance at which they should be positioned inside the chip were discussed. Then the characteristics of the lithographic mask were analyzed and finally the manufacturing process of the silicon tip chip prototypes was deepened in detail. In particular, the various attempts made to obtain probe tips with the desired features have been reported in the last section. The experimental method used involved the alternation of etching and inspection phases to optimize the process parameters at each step. 26 samples from 4 different wafers were used for the experimentation. Initially it was decided to make the tips through a single etching step. The first tests were carried out with the aim of determining the recipe etch rate and subsequently the variation of tip tapering as a function of the passivating gas flow rate has been studied. By putting the information together, the single-etching-step tip prototypes were created. They turned out to be incompatible with the project specifications and therefore a new approach consisting of multiple etching steps was successively used. This new approach proved to be efficient and allowed the creation of prototype tips with very appreciated features. The process was therefore optimized to create high-aspect-ratio and high sharpness tips starting from a $7\mu m$ diameter circular mask. Finally, the process was also tested for smaller diameters masks obtaining excellent results starting from circular masks of $6\mu m$.

4. RTS SPM measurements

4.1 Introduction

In the previous chapters different silicon tip chips prototypes have been designed and manufactured. The performance of these prototypes have been evaluated by various measurements aimed in particular at determining the tips features. This has been done by analyzing the measurements quality and resolution. Measurements were made using a Bruker Dimension Icon PT AFM in RTS SPM configuration. This chapter contains a detailed description of the measurements made and the samples analyzed. Furthermore, a comparison is made between the performance obtained in the RTS SPM configuration and those generally obtained in the classical configuration. For the RTS SPM to be considered as a valid alternative to the classic method, it is necessary to show that the RTS SPM measurements have at least the same resolution as the classic configuration and that different AFM modes are possible. For this reason the measurements were carried out both in contact mode and in tapping mode.

4.2 Samples

To perform RTS SPM measurements, the tip chip must be placed on the stage while the sample, positioned on the cantilever, is scanned over it, as described in section 2.1.1. The preparation of a FIB-based test sample for this type of measurement is more complex (see section 2.2.4); therefore it was decided to simplify the procedure by using the cantilever itself (without any tip at its edge) as a sample. In particular, three different types of cantilevers were used: a nickel cantilever, a nickel cantilever with an in-plane diamond tip layer and a silicon cantilever. Initially, the first measurements were made to analyze the roughness of the three cantilevers, then the simple nickel cantilever was coated with diamond nanoparticles and the silicon cantilever was coated with DNA. Both were re-analyzed to determine the measurement resolution and quality. The following

list summarizes all the samples used in this work together with an explanation regarding their preparation.

- **Sample A:** Nickel cantilever ($225\mu\text{m}$ long, $50\mu\text{m}$ wide and $5\mu\text{m}$ thick).
- **Sample B:** Diamond nanoparticles (DNPs) coated nickel cantilever. This sample was prepared starting from a simple Ni cantilever. A few droplets of a solution containing DNPs were poured into a beaker. The Ni cantilever was then immersed in the solution for 30 seconds (time necessary for the diamond nanoparticles present in the solution to settle on the surface of the cantilever). Finally the cantilever was immersed in ethanol for rinsing and dried with a nitrogen gun. The DNPs have a diameter of 4-5nm but, once the solution is prepared, they cluster together. Therefore particles with a diameter ranging between 4nm and 30nm can be deposited on the cantilever. The preparation procedure is shown in figure 4.1.

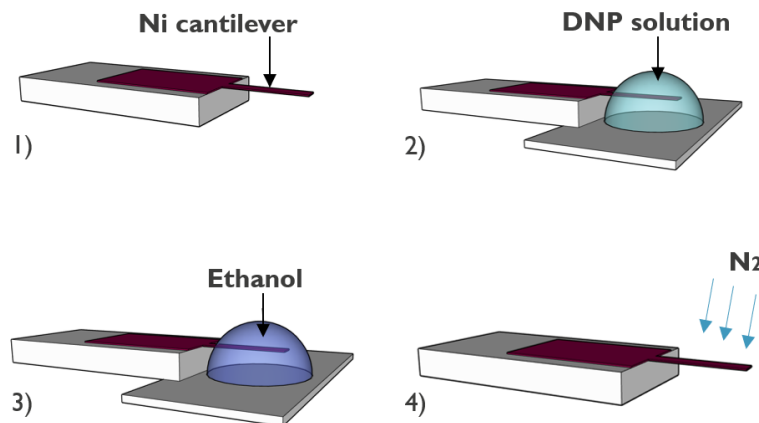


Figure 4.1: DNPs covered Ni cantilever preparation: 1) start from a simple Ni cantilever, 2) immerse it in a DNPs solution, 3) immerse it in ethanol 4) dry with N_2 gun.

- **Sample C:** Nickel cantilever with an in-plane diamond tip made by chemical vapour deposition (CVD), the cantilever is $150\mu\text{m}$ long, $50\mu\text{m}$ wide and $5\mu\text{m}$ thick [61].
- **Sample D:** Silicon cantilever ($125\mu\text{m}$ long, $30\mu\text{m}$ wide and $4\mu\text{m}$ thick [62]) covered with a native oxide layer.
- **Sample E:** DNA coated silicon cantilever. The DNA used is from bacteriophage lambda and it is a linear, double-stranded DNA of 50000bp in length, that corresponds to $16.7\mu\text{m}$ (bp= base pair and 1bp = 0.334nm). The DNA width is about 2nm. To prepare the DNA coated sample a $125\mu\text{m}$

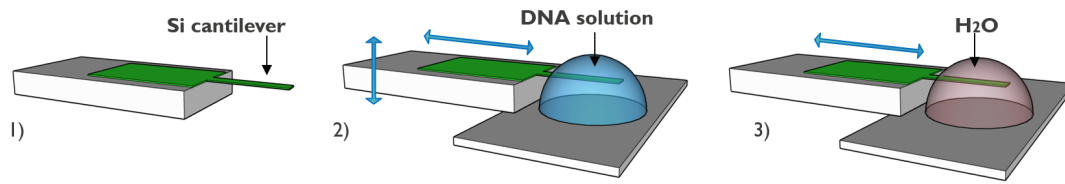


Figure 4.2: DNA covered Si cantilever preparation: 1) start from a simple Si cantilever, 2) immerse it in a DNA solution and moved in and out for straight DNA shape or up and down for more curled DNA shape, 3) moved it a few times forward and backward in pure H_2O .

long Si cantilever is chosen. A $30\mu l$ droplet of DNA solution is placed on a hydrophobic polypropylene surface. Then the Si cantilever is alternately moved in and out of the DNA solution droplet to obtain a straight DNA shape or is moved up and down for more curled and entangled DNA shape. Subsequently, the Si cantilever is moved a few times forward and backward in pure H_2O droplet for the rinsing effect. In this case the sample is used directly without a N_2 drying step. The preparation procedure is shown in figure 4.2.

4.3 RTS SPM measurements

4.3.1 Sample A

Sample A, i.e. the Ni cantilever, was initially analyzed with the Bruker Dimension Icon PT tool. The tips belonging to sample 15 were used as probes (details relating to sample 15 are present in the section 3.4.1, fourth set of experiments). The tool was used in tapping mode. The resonant frequency is a property dependent on the cantilever material and shape, in this case it is about 50KHz. Figure 4.3 shows three AFM measurements corresponding to three different scan sizes: $1\mu m$, 500nm and 100nm. Furthermore, in figure 4.3 there is also a graph showing a sample surface cross section. From these measurements it can be concluded first of all that the tip used, belonging to sample 15, has a reasonably-high sharpness allowing to analyze, with a resolution estimated at ~ 10 -20nm, the roughness of the sample. This seems at first to be in contradiction with that established in section 3.4.1, in which the tip top diameter was estimated at 250nm thanks to the SEM image (see figure 3.15). Indeed, the the top tip surface is covered with nanoscopic asperities and one of these was used as a probe during AFM analysis, leading to a measurement with reasonably high resolution. However, this is valid only if the samples used have a flat surface, as in this case, where high-

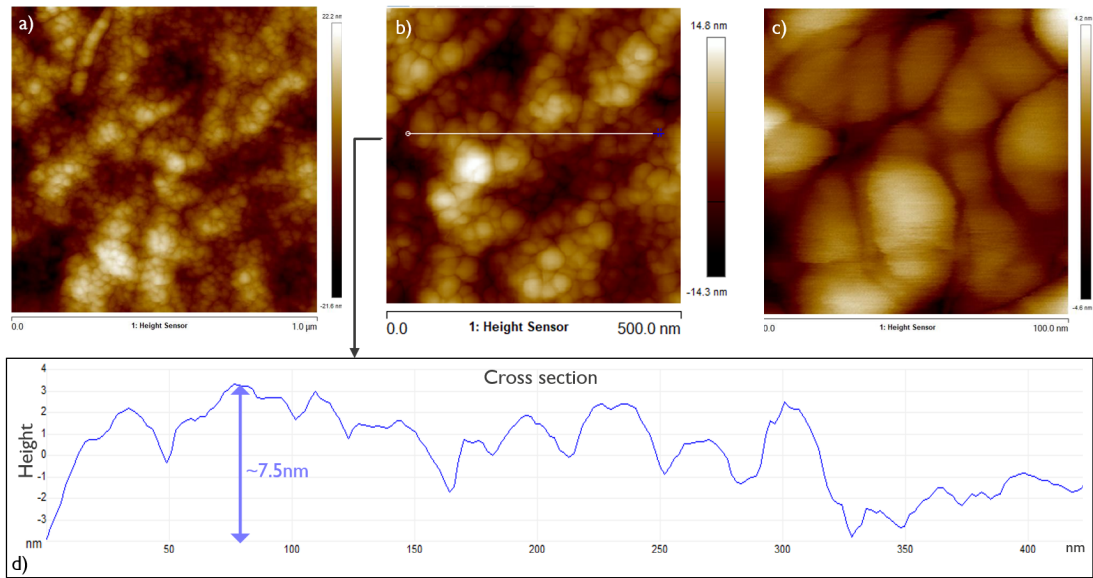


Figure 4.3: Sample A AFM measurements obtained used sample 15 tips as probes. Measurements were taken in tapping mode. Figure shown three different scan sizes measurements: $1\mu m$ (a), $500nm$ (b) and $100nm$ (c). In figure (d) a cross section of the sample surface is shown.

aspect-ratio tips are not necessary. If, on the other hand, one wanted to analyze a sample with trenches, the tip nanoscopic asperities would no longer play the fundamental role in the measurement and the resolution would be determined by the top microscopic diameter, in this case of $250nm$. In any case, for this particular sample, the used tip is nanoscopically sharp enough to evaluate the sample roughness.

Roughness is a physical parameter related to the morphology of a surface, it can be expressed by means of a set of mathematical parameters, which are extracted from the surface profile. The main parameters are the arithmetic mean deviation from the centre line (R_a) and the root mean square deviation from the centre line (R_q). R_a is the simpler and most used parameter, but is unable to distinguish between features with the same area despite of different heights. R_q is the standard deviation of the height distribution and it is more sensible than R_a to the presence of high peaks or low valleys. In this project the AFM measurements are analyzed with the NanoScope Analysis software which provides both R_a and R_q values. In this case R_a is $3.3nm$ and R_q is $4.1nm$, therefore the roughness of this sample corresponds to a few nanometers.

4.3.2 Sample B

Sample B, consisting of a DNPs-covered Ni cantilever, was also analyzed using the tips from tip sample 15 as probes (see figure 3.15). The measurement was performed in contact mode. Three AFM measurements ($1\mu\text{m}$, 500nm and 250nm) of the sample are shown in figure 4.4. The aim of this analysis is to estimate the image resolution, i.e. what is the minimum detectable size, which is strictly dependent on the tip size. As previously described, DNPs have a diameter of $4\text{-}5\text{nm}$ but they clustered together in the solution. Therefore it is impossible to know the real size of the particles being analyzed but from the images obtained it is possible to measure the size of the smallest structures detected. For this purpose, a line cross section of a portion of the sample surface is shown in figure 4.3(d). As one can see from the graph, the used tip was able to detect a structure of the size of 8.6nm , therefore it can be said that the tip resolution is at least corresponding to 8.6nm .

The same sample was analyzed using one tip of sample 20 as a probe (details relating to sample 20 are present in the section 3.4.1, fifth set of experiments). In figure 4.5 two AFM measurements, taken in tapping mode, are reported with different scan sizes: $3\mu\text{m}$ and $1\mu\text{m}$. A sample surface cross section graph is reported as well. The used tip has a top diameter of about 30nm , therefore the resolution

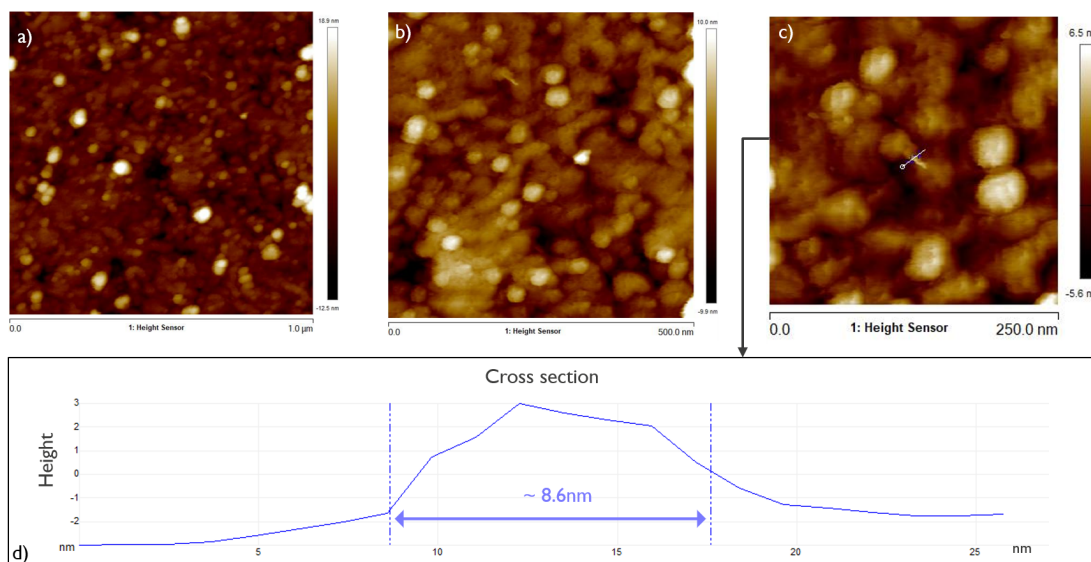


Figure 4.4: Sample B AFM measurements obtained used sample 15 tips as probes. The measurements were done in contact mode. Figure shown three different scan sizes measurements: $1\mu\text{m}$ (a), 500nm (b) and 250nm (c). In figure (d) a cross section of the sample surface is graphed. From these images is possible to obtain an order of magnitude of the resolution, it is at least 8.6nm .

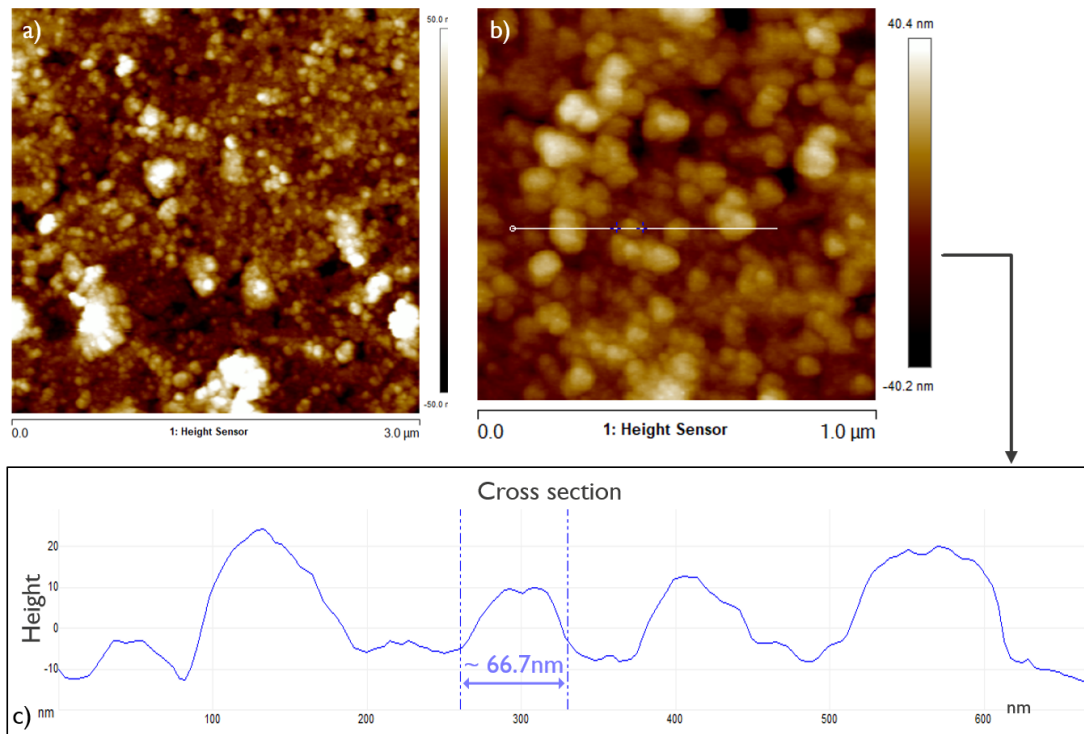


Figure 4.5: Sample B AFM measurements obtained used sample 20 tips as probes. AFM measurements were taken in tapping mode. Figure shown two different scan sizes measurements: $3\mu m$ (a) and $1\mu m$ (b). In figure (c) a cross section of the sample surface is graphed.

expected from measurements made with this tip is high. From the AFM images it can be seen that DNPs profile is clearly determined but unfortunately, DNPs with a diameter smaller than about 67nm were not detected on the surface. The only thing that can be said about the resolution is that it is at least about 67nm. To more accurately estimate the resolving power of this tip, it has been used for the analysis of other different samples.

As previously mentioned, the biggest advantage of the RTS SPM configuration is the ability to easily change the tip during the measurement by simply moving the cantilever from one tip to another one. As mentioned in section 3.2.2 (Distance between tips) the stage can only move over an area of $50\mu m \times 50\mu m$ after engaging the sample to the probe. For this reason if the distance between tips is $25\mu m$, then 9 tips can be changed during the measurement. Using the tips of sample 20 as a probe and the DNPs-covered Ni cantilever as a sample, it was demonstrated that the change of 9 tips during the RST SPM measurement is possible. In figure 4.6 two AFM images (with different scan sizes: $3\mu m$ and $1\mu m$) of the same surface are reported taken with each tip. This property of the RTS SPM configuration allows to save a lot of time during the measurement phase: when a tip is damaged

or worn it can be quickly changed without wasting time. It is also possible, as in this case, to scan the same surface with different tips, allowing to select the best AFM image afterwards.

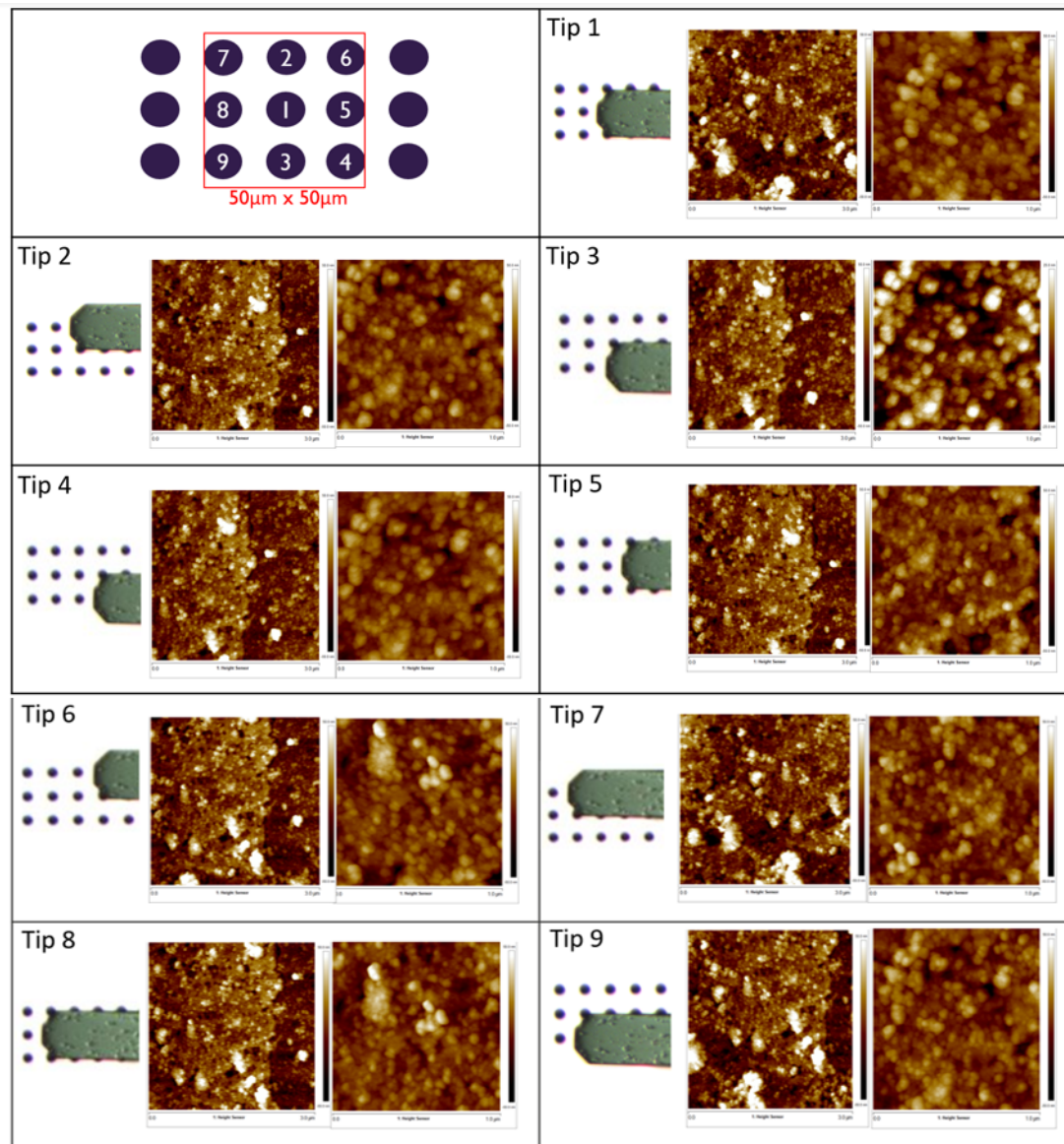


Figure 4.6: AFM images of the sample B taken with 9 different tips belonging to sample 20. For each tip two AFM measurements (with different scan size: $3\mu m$ and $1\mu m$) and an optical image of the cantilever during the measurement are reported. A scheme that represents the 9 tips used with their label is also reported.

4.3.3 Sample C

Tips of sample 20 are used as probes for the analysis of sample C, which has a surface of diamond grown through CVD. Figure 4.7 shows two AFM images at different scan sizes ($1\mu\text{m}$ and 500nm) and a cross section of the sample surface. Through the latter it can be seen that the tip is able to detect structures with a size of about 20nm therefore it can be said that the resolution is at least 20nm . As for the roughness of the sample, it was determined with the NanoScope Analysis software, the value of R_q is 1.1nm and the value of R_a is 0.9nm .

From these first AFM measurements carried out on samples A, B and C some conclusions can be drawn. First of all it can be stated that both used tips have a reasonable high sharpness, in particular in sample 15 it is caused by the nanoscopic asperities present on the surface of the tip while in sample 20 it is related directly by the nanometric tip top diameter. Furthermore, neither tip artifacts nor double-tip images are visible in the measurements taken. Secondly, the measurements have been carried out both in contact and in tapping mode with success; this shows that this type of configuration is versatile and can be used

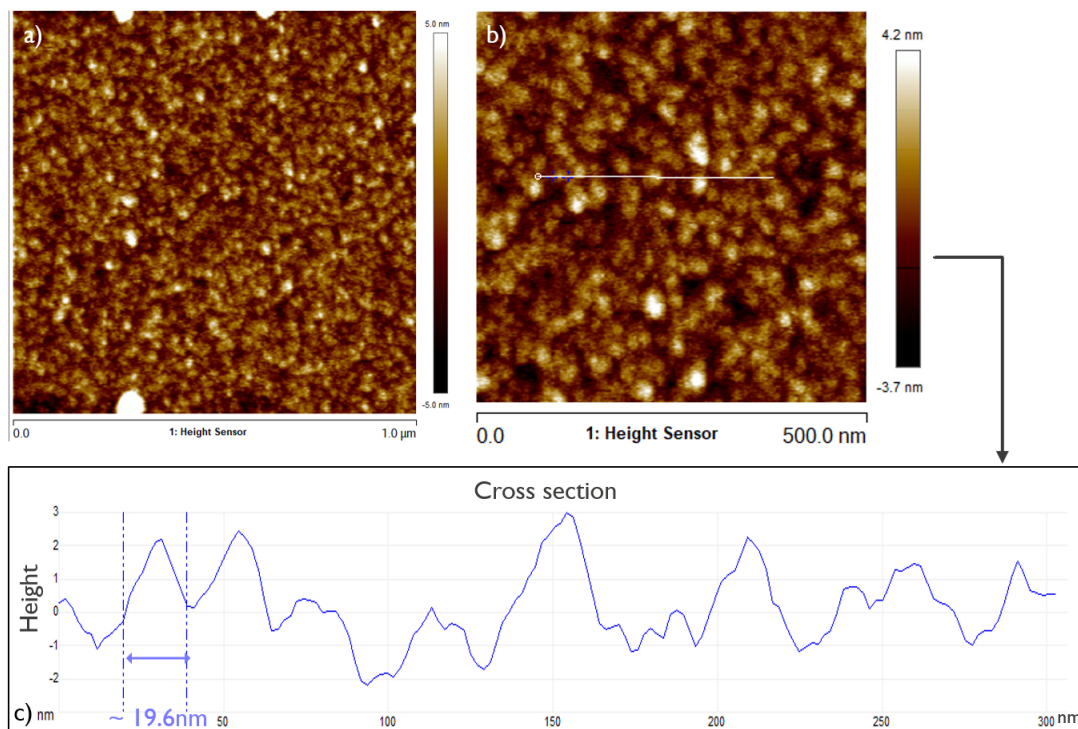


Figure 4.7: Sample C AFM measurements obtained used sample 20 tips as probes. AFM measurements were taken in tapping mode. Figure shown two different scan sizes measurements: $1\mu\text{m}$ (a) and 500 nm (b). In figure (c) a cross section of the sample surface is graphed. From this it is possible to estimate the resolution to at least about 20 nm .

for different AFM modes. As for the resolution, through these first measurements it was possible to make an estimate of its order of magnitude. The purpose of the subsequent measurements is to determine more precisely the resolving power of the tips contained in sample 20. Sample E, consisting of a silicon surface covered by DNA strands, was used. The DNA strands have a width of about 1-2nm therefore if they are detected during the measurement it means that the resolution of the image is very high and an estimation of the tip diameter can be done.

4.3.4 Sample D

The cantilever that hosts the DNA is a $125\mu\text{m}$ long silicon cantilever. For this reason a silicon cantilever with the same features as the one covered by DNA was analyzed to define its roughness. A Si tip from sample 20 was used as a probe. Figure 4.8 shows a SEM image of the silicon cantilever and two AFM measurements taken at different scan sizes. The AFM measurements are taken in tapping mode. The resonant frequency of this type of cantilever is about 350kHz. The roughness of the cantilever surface has been determined with NanoScope Analysis software, Ra is 0.4nm and Rq is 0.5nm.

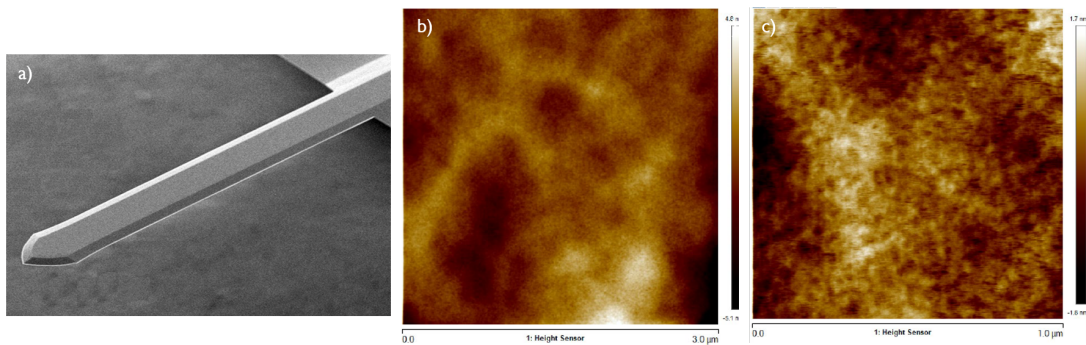


Figure 4.8: Sample D: a) SEM image of the silicon cantilever [62]. b) and c) AFM measurements obtained used sample 20 tips as probes. They were taken in tapping mode. Figure shown who different scan sizes measurements: $3\mu\text{m}$ (b) and $1\mu\text{m}$ (c). These measurements were used to determine the surface roughness.

4.4 Samples E

Two silicon cantilevers with the same characteristics were coated with bacteriophage lambda DNA as described above. One of them (sample E1) was prepared by moving the cantilever forward and backward from the DNA solution to obtain straight DNA strands, while the other one (sample E2) was prepared by moving the cantilever up and down the inside of the DNA solution to obtain more curled shape DNA strands. Both were analyzed using sample 20 tips as probes in AFM tapping mode.

Through these measurements it is possible to estimate the dimension of the tips used as probes. When analyzing morphological structures whose dimensions are comparable or smaller to those of the tip, what the instrument transmits is the convolution between the shape of the tip and that of the surface, as shown in figure 4.9. By analyzing the profile obtained, it is however possible to get various information regarding both the real size of the measured structure and the size of the tip diameter. With respect to the DNA it is possible to determine its real size by measuring the height of the peak of the profile obtained (d_{REAL}) while the width of the peak is measured ($d_{TIP} + d_{REAL}$), it is possible to estimate the diameter of the tip. The peak width is given by sum of the real DNA diameter and the diameter of the tip, therefore, once the size of the DNA has been estimated, it is also possible to estimate the diameter of the tip.

Figures 4.10, 4.11 and 4.12 show three different regions of sample E1 with four different scan sizes while figure 4.13 contains AFM measurements of two

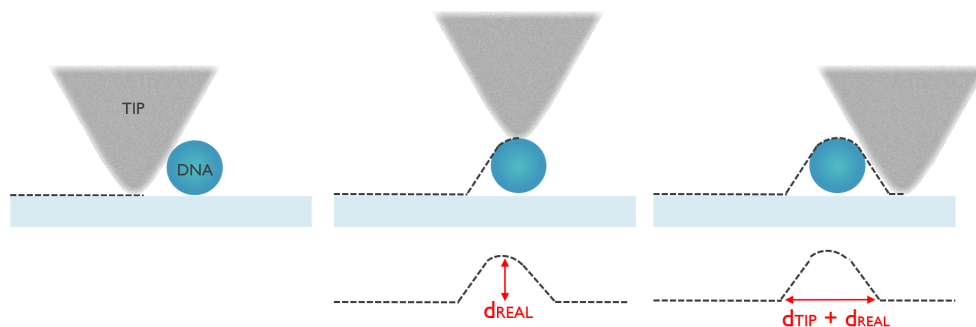


Figure 4.9: Estimation of the tip diameter: once the profile of the sample has been measured, it is possible to obtain information about the tip geometry if it has dimensions comparable or greater than those of the measured structure. By measuring the height of the peak (d_{REAL}) it is possible to determine the real size, in this case, of the DNA, while by measuring the width of the peak ($d_{TIP} + d_{REAL}$) information relating to the tip diameter are obtained as the width of the peak is approximately the sum of the real diameter of the DNA and the diameter of the tip.

different regions of the sample E2. In all figures it is possible to recognize the DNA profile. Cross sections of the surfaces have been reported to estimate the tip diameter and the DNA size. The heights of the peaks of the different cross sections reported have allowed to confirm that the diameter of the DNA is about 1-2nm. The peak widths measured are as follows: 11.8nm, 15.2 nm, 3.8nm, 20.5nm and 12.2nm. Therefore, considering that the real size of the DNA is about 1-2 nm, it is possible to establish that the diameter of the tips contained in the sample 20 ranges from about 2nm to 18nm.

In conclusion, these measurements have demonstrated that these tips can be successfully used to obtain high-resolution AFM measurements in RTS SPM configuration. By comparing the apex size of the tips produced in this project and the apex size of the tips on the market [63], [64], [65], it can be seen that they have approximately the same order of magnitude. Therefore it is possible to consider the RTS SPM configuration as a valid and competitive alternative to the classic AFM method. Furthermore, it has been shown that these tips can be successfully used to test biological tissues.

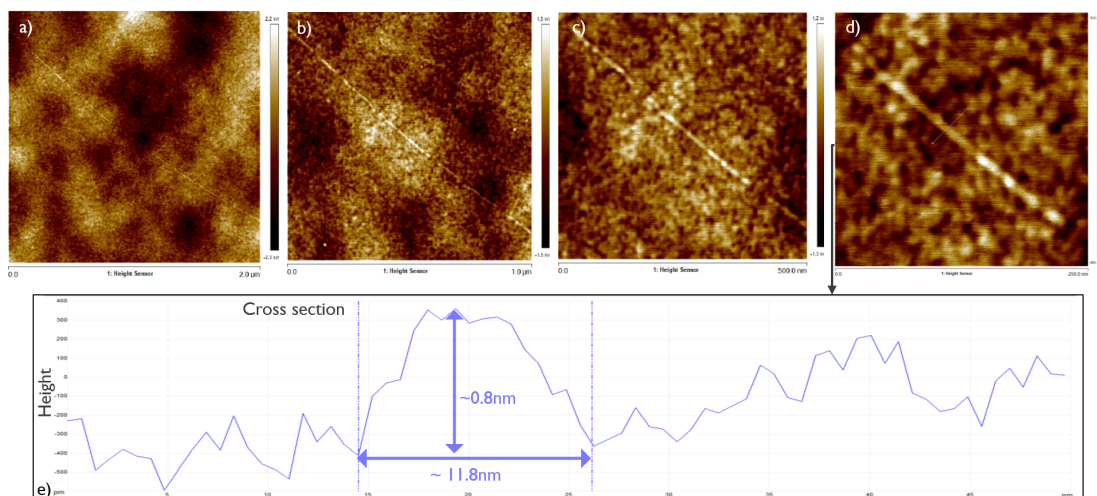


Figure 4.10: Sample E1 AFM measurements obtained used sample 20 tips as probes. AFM measurements were taken in tapping mode. Figure shown four different scan sizes measurements: $2\mu m$ (a), $1\mu m$ (b), 500nm (c) and 250nm (d). In figure (e) a cross section of the sample surface is graphed.

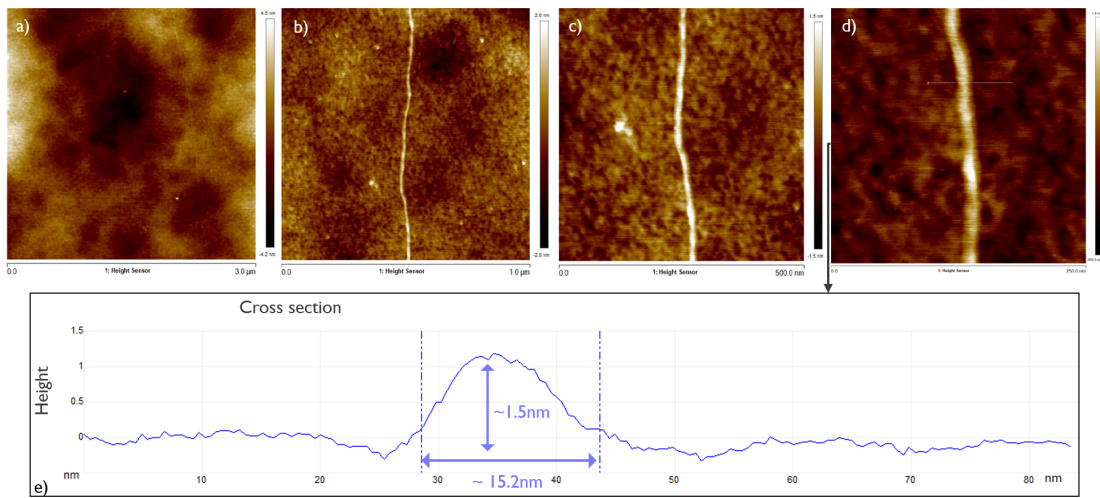


Figure 4.11: Sample E1 AFM measurements obtained used sample 20 tips as probes. AFM measurements were taken in tapping mode. Figure shown four different scan sizes measurements: $3\mu m$ (a), $1\mu m$ (b), $500nm$ (c) and $250nm$ (d). In figure (e) a cross section of the sample surface is graphed.

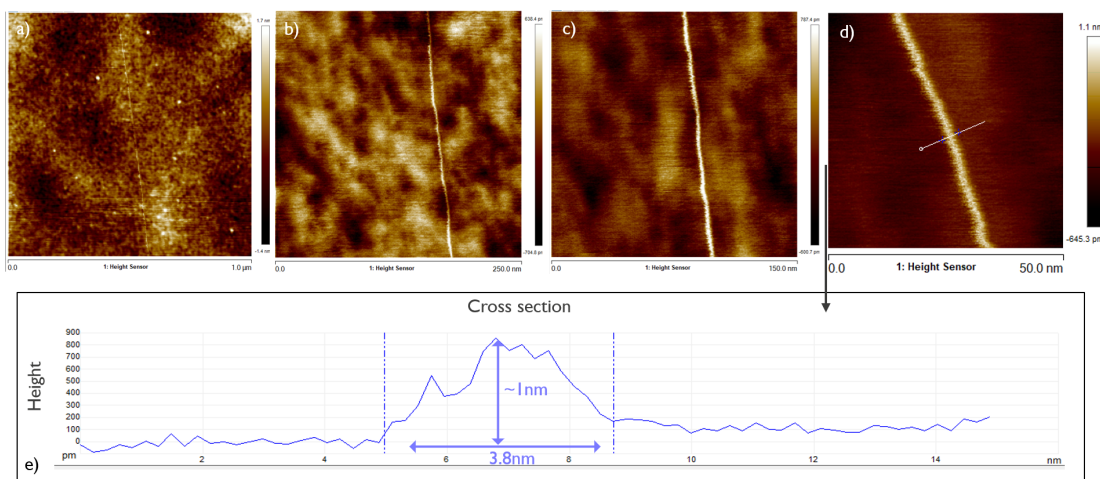


Figure 4.12: Sample E1 AFM measurements obtained used sample 20 tips as probes. AFM measurements were taken in tapping mode. Figure shown four different scan sizes measurements: $1\mu m$ (a), $250nm$ (b), $150nm$ (c) and $50nm$ (d). In figure (e) a cross section of the sample surface is graphed.

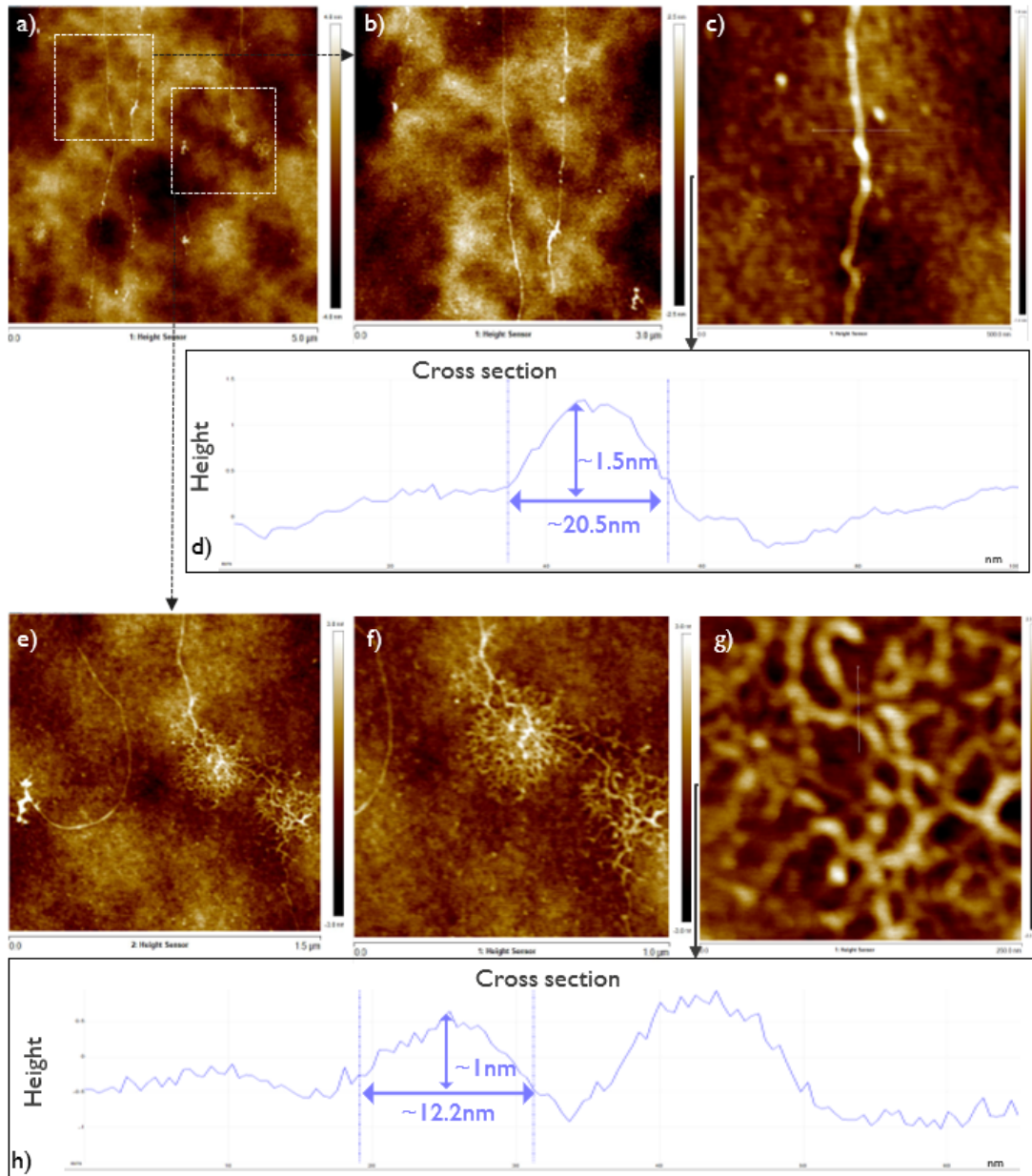


Figure 4.13: Sample E2 AFM measurements obtained used sample 20 tips as probes. Two AFM measurements were taken in tapping mode. The AFM image (a) shows two different regions of the surface measured with different scan sizes: $3\mu\text{m}$ (b), 500 nm (c), $1.5\mu\text{m}$ (e), $1\mu\text{m}$ (f) and 250 nm (g). Two cross sections (d) and (h) are reported to estimate the DNA sizes.

5. Conclusions and outlook

This chapter presents a summary of the main achievements obtained in this research and discuss possible further improvements in future projects.

5.1 Conclusions

In order to overcome some main limitations related to scanning probe microscopy (SPM), a new approach called reverse tip sample scanning probe microscopy (RTS SPM) has been developed at IMEC in recent years. This innovative method is based on the same operating principle as the classic SPM but involves the inversion of the tip and sample position. The main advantage that this new approach has brought is the possibility to substitute a single tip with a chip containing multiple tips. Consequently, this leads to the possibility of quickly and simply tip changing and the possibility of using tips with different features during the measurement. In a previous masters thesis work the first tip chip prototypes were produced. They were composed of pyramidal diamond tips made by a molding process but they still had some limitations: the tips suffered from a low-aspect-ratio and also the manufacturing method was not adaptable to other tip materials. Our research fitted into this context with the aim of overcoming the existing technology limitation. In particular it has the primary objective to design, fabricate and evaluate the new tip chip prototypes, composed of high-aspect-ratio and high sharpness silicon tips. The main achievements of this thesis work can be summarized as follows:

- A novel fabrication process has been established for Si tip chips manufacturing which overcomes the limitations of the existing molding approach (low aspect ratio tips, limited to diamond tips mainly).
- High-aspect-ratio Si tips with a high tip sharpness can be made and used for RTS SPM topography measurements. The developed two-step etching approach has the advantage that both the pedestal and tip height can be adjusted as needed for the application.

- The developed approach allows for cost-efficient manufacturing as it uses standard lithography and dry etching.
- The demonstrated plasma shrinkage step leads to the self-alignment of the small tip to the center of the pedestal which is advantageous for the targeted SPM applications.
- Silicon tips with a height of about $11\mu\text{m}$ and a top diameter ranging from 2nm to 18nm are obtained starting from a circular resist mask with a diameter of $7\mu\text{m}$. This is done by means of executing a dual-step dry etching process, using SF_6 as an etchant and C_4F_8 as a passivating.
- Using the fabricated prototype as probes, some samples were tested in RTS SPM configuration. This allowed us to evaluate the tip properties. In particular we can conclude that:
 - The tips used as probes have a sharpness high enough to allow the evaluation of the sample surface roughness.
 - The resolution of the AFM images obtained is high, the possibility to distinguish structures having dimensions of 8-9nm has been demonstrated.
 - It is possible to switch the probe tip during the measurement up to 9 times, thus obtaining 9 different AFM images of the same surface. This operation cannot be done in the normal mode and demonstrates that the RTS SPM configuration has a high potential.
 - Using a DNA strand deposited on a silicon cantilever as a sample, we could estimate that the tips top diameter is about 2-18 nm, value comparable to that of the AFM tips currently on the market.
 - Finally, this new configuration allows to carry out biological experiments as it allows to perform multiple measurements with different tips simply by fixing the biological tissue on the cantilever. Furthermore the measurement can easily be performed in liquids as required for most biological tissues so that they are not damaged during measurement.

5.2 Future work and outlook

In this research project we mainly focused on finding a recipe for the etching process that would lead to the predetermined result. However, at the same time, we realized that the process is not always reproducible: many times it has happened that, despite the use of the same recipe parameters, we have obtained different results. This can be mainly attributed to a lack of precision of the used research-lab tools with a tendency to drift in the process parameters due to the use for many different projects. Therefore it is suggested for future work to test the same process using more sophisticated in-line fab tools in order to obtain a completely reproducible process suitable for wafer scale manufacturing.

For future work it is also suggested to carry out some electrical measurements in RTS SPM configurations. They can be performed by covering the silicon tip chip with a metal coating, for example a metallic layer composed of 20nm of TiW and 20 nm of Au could be used.

Additionally, we used 2cmx2cm sized samples for our tests. We have noticed that if the same recipe used for the samples is used to directly process a 4-inch wafer different results are obtained. Probably this is due to the larger amount of Si substrate material to be etched: the same chemical species that were previously used for a 2cmx2cm sample are probably insufficient to etch a whole wafer in the same way; they, reacting with a greater quantity of material, are consumed faster altering the final result. Therefore, it is suggested to optimize the recipe for the production of tip chips contained on a surface of an entire 4-inch wafer.

Furthermore, as demonstrated for a circular mask with a diameter of $6\mu m$, by varying the parameters of the recipe it is possible to obtain tips with the same shape but with a smaller base, increasing the tip-aspect-ratio value.

Eventually, if a further reduction of the tip diameter is required, it would be interesting to try out to use a thermal oxidation step as the last step of the manufacturing process. There are references in the literature in which the thinning of silicon tips by thermal oxidation is demonstrated [66], [67].

Acknowledgments

First of all I would like to thank my mentor Thomas Hantschel for giving me the great opportunity to work at IMEC alongside him and for guiding me during this thesis project. His teachings and his brilliant ideas were invaluable and fundamental to achieving the goal. He not only showed me the right way but also left me the freedom to put my ideas into action and try to do everything with my hands, allowing me to learn as much as possible from this experience.

Secondly, I would like to thank my other supervisor, the professor Matteo Cocuzza, for helping and supporting me during the writing of this thesis.

I would also like to express my gratitude to Masoud Dialameh for his kindness and availability; he, with his knowledge, has provided me important suggestions for achieving the goal.

Furthermore, I would like to thank all the III-V area users who have always been available and ready to help me during my work in the cleanroom. In particular I would like to thank Tsvetan Ivanov and Patrick Verdonck for their help with Oxford Plasmalab 100 tool.

I dedicate this work to all the people I love: to my family, which has always been by my side and supported me during all these years of study; to Manuel, who, with his love, always made me feel at home; to my friends Irene, Carlo and Federica, who have always been there.

List of Figures

2.1	AFM setup	10
2.2	AFM D3100	10
2.3	AFM probe schematic figure	13
2.4	SSRM setup schematic figure	14
2.5	SSRM nanocontact schematic figure	16
2.6	SSRM equivalent electric circuit	17
2.7	SSRM probe composed of three different nickel cantilevers.	19
2.8	SSRM probe, zoom on the medium cantilever.	19
2.9	Scalpel SPM, 3D-image as a sum of 2D-images	20
2.10	Scalpel SSRM working principle schematic figure	21
2.11	RTS SPM setup schematic figure	22
2.12	RTS SPM concept	23
2.13	Diamond tips fabrication process	24
2.14	Diamond tip chips	25
2.15	RST sample preparation	26
3.1	Tip aspect ratio	28
3.2	Tip minimum height	30
3.3	Cantilever 7° tilted	31
3.4	Tip chip example of structure	32
3.5	Mask structure	33
3.6	Samples fabrication process	34
3.7	Reactive ion etching schematic figure	36
3.8	Reactive ion etching tool and chamber	37
3.9	Sample 5 SEM images	41
3.10	Etch dept graph	42
3.11	Second set of experiments: gas flow rates	43
3.12	Samples 8, 9, 10 and 11 SEM images	44
3.13	Samples 12, 13 and 14 SEM images	46

3.14	Two etching steps approach schematic figure	47
3.15	Sample 15 SEM images	48
3.16	Samples 16, 17 and 18 SEM images	50
3.17	Samples 19 SEM images	51
3.18	Chip model obtained with the <i>2nd</i> lithography mask	52
3.19	Samples 20 and 21 SEM images after O_2 plasma	53
3.20	Samples 20 and 21 SEM images	54
3.21	Oxygen plasma phase performed at different times	56
3.22	Samples 22 and 23 SEM images	57
4.1	DNPs covered Ni cantilever preparation	60
4.2	DNA covered Si cantilever preparation	61
4.3	Sample A AFM measurements obtained used sample 15 tips as probes	62
4.4	Sample B AFM measurements obtained used sample 15 tips as probes	63
4.5	Sample B AFM measurements obtained used sample 20 tips as probes	64
4.6	AFM images of sample B taken with 9 different tips belonging to sample 20	65
4.7	Sample C AFM measurements obtained used sample 20 tips as probes	66
4.8	Sample D AFM measurements obtained used sample 20 tips as probes and SEM image	67
4.9	Estimation of the tip diameter	68
4.10	Sample E1 AFM measurements obtained used sample 20 tips as probes	69
4.11	Sample E1 AFM measurements obtained used sample 20 tips as probes	70
4.12	Sample E1 AFM measurements obtained used sample 20 tips as probes	70
4.13	Sample E2 AFM measurements obtained used sample 20 tips as probes	71

List of Tables

3.1	Samples general information	40
3.2	Summary table containing information of the first set of experiments	41
3.3	Summary table containing information of the second set of experiments	43
3.4	Summary table containing information of the third set of experiments	45
3.5	Summary table containing information of the fourth set of experiments	49
3.6	Summary table containing information of the fifth set of experiments	54
3.7	Summary table containing information of the sixth set of experiments	56

Bibliography

- [1] *International Technology Roadmap for Semiconductors 2.0.*, (2015) <http://www.itrs2.net/itrs-reports.html>.
- [2] Radamson H. H., Zhu H., Wu Z., He X., Lin H., Liu J., Xiang J., Kong Z., Xiong W., Li J., Cui H., Gao J., Yang H., Du Y., Xu B., Li B., Zhao X., Yu J., Dong Y., Wang G., *State of the Art and Future Perspectives in Advanced-CMOS Technology*, *Nanomaterials*, 10, (2020), doi:10.3390/nano10081555.
- [3] Brown G. A., Zeitzoff P. M., Bersuker G., Huff H. R., *Scaling CMOS: Materials & devices*, *Materials Today*, 7, 1, pp. 24-25, (2004), doi: 10.1016/S1369-7021(04)00051-3.
- [4] Salapaka S. M., Salapaka M. V., *Scanning Probe Microscopy*, *IEEE Control Systems Magazine*, 28, 2, pp. 65-83, (2008), doi: 10.1109/MCS.2007.914688.
- [5] Mironov V. L., *Fundamentals of scanning probe microscopy*, The Russian academy of sciences institute for physics of microstructures, (2004).
- [6] Binnig G. K., Rohrer H., Gerber Ch., Weibel E., *Tunneling through a controllable vacuum gap*, *Appl. Phys. Lett.* 40, 178, (1982), doi: /10.1063/1.92999.
- [7] Binnig G. K., Quate C. F., Gerber Ch., *Atomic Force Microscope*, *Phys. Rev. Lett.* 56, 9, pp. 930-933, (1986), doi: 10.1103/PhysRevLett.56.930.
- [8] De Wolf P., Geva M., Hantschel T., Vandervorst W., Bylsma R.B., *Two-dimensional carrier profiling of InP structures using scanning spreading resistance microscopy*, *Appl. Phys. Lett.* 73, 2155 (1998), doi: 10.1063/1.122408.
- [9] Eyben P., Xu M., Duhayon N., Clarysse T., Callewaert S. et al., *Scanning spreading resistance microscopy and spectroscopy for routine and quantitative two-dimensional carrier profiling*, *J. Vac. Sci. Technol. B* 20, 471, (2002), doi: 10.1116/1.1424280.

- [10] Eyben P., Denis S., Clarysse T., Vandervorst W., *Progress towards a physical contact model for scanning spreading resistance microscopy*, Mater. Sci. Eng. B 102, (2003).
- [11] De Wolf P., Stephenson R., Trenkler T., Clarysse T., Hantschel T., Vandervorst W., *Status and review of two-dimensional carrier and dopant profiling using scanning probe microscopy*, J. Vac. Sci. Technol. B: Microelectronics and Nanometer Structures Processing, Measurement, and Phenomena 18, 361 (2000), doi: 10.1116/1.591198.
- [12] Celano U., Vandervorst W., *Scanning probe tomography for advanced material characterization*, 2014 IEEE International Integrated Reliability Workshop Final Report (IIRW), (2014), doi: 10.1109/IIRW.2014.7049494.
- [13] Schulze A., Hantschel T., Dathe A., Eyben P., Ke X., Vandervorst W., *Electrical tomography using atomic force microscopy and its application towards carbon nanotube-based interconnects*, Nanotechnology 23, (2012), doi: 10.1088/0957-4484/23/30/305707.
- [14] Xu M. W., Hantschel T., Vandervorst W., *Three-dimensional carrier profiling of InP-based devices using scanning spreading resistance microscopy*, Appl. Phys. Lett. 81, 177, (2002), doi: 10.1063/1.1490399.
- [15] Mody J., Zschätzsch G., Kölling S., De Keersgieter A., Eneman G., Kambham A. K., Drijbooms C., Schulze A., Chiarella T., Horiguchi N., Hoffmann T.-Y., Eyben P., Vandervorst W., *3D-Carrier Profiling in Fin-FETs using Scanning Spreading Resistance Microscopy*, Electron Devices Meeting, 1988, IEDM '88, Technical Digest., International, (2011), doi: 10.1109/IEDM.2011.6131498.
- [16] Celano U., Favia P., Drijbooms C., Dixon-Luinenburg O., Richard O., Bender H., Vancoille E., Paredis K., Loo R., Schulze A., Hikavy A., Witters L., Mitard J., Collaert N., Horiguchi N., Vandervorst W. *Individual Device Analysis Using Hybrid TEM-Scalpel SSRM Metrology*, Frontiers of Characterization and Metrology for Nanoelectronics, (2017).
- [17] Celano U., Hantschel H., Boehme T., Kannianen A., Wouters L., Bender H., Bosman N., Drijbooms C., Folkersma S., Paredis K., Vandervorst W., van der Heide P., *Reverse tip sample scanning for precise and high-throughput electrical characterization of advanced nodes*, 2019 IEEE International Electron Devices Meeting (IEDM), (2019).

- [18] Kannianen A., *Reverse tip sample scanning probe microscopy*, Master thesis, (2020).
- [19] Binnig G. K., *Atomic-Force Microscopy*, Phys. Scr. 53, (1987), doi: 10.1088/0031-8949.
- [20] <http://cbm.cnrs-orleans.fr/wp-content/uploads/2019/05/1-AFM-D3100.jpg>
- [21] Bramowicz M., Kulesza S., and Rychlik K., *A Comparison between Contact and Tapping AFM Mode in Surface Morphology Studies*, Techn. Sc., 15(2), pp. 307-318, (2012).
- [22] Hansma P. K., Cleveland J. P., Radmacher M., Walters D. A., Hillner P. E., Bezanilla M., Fritz M., Vie D., Hansma H. G., Prater C. B., Massie J., Fukunaga L., Gurley J., Elings V., *Tapping mode atomic force microscopy in liquids*, Appl. Phys. Lett. 64, 1738, (1994), doi:10.1063/1.111795.
- [23] Sauer B. B., McLean R. S., Thomas R. R., *Tapping Mode AFM Studies of Nano-Phases on Fluorine-Containing Polyester Coatings and Octadecyl-trichlorosilane Monolayers*, Langmuir, 14, 3045-3051, (1998).
- [24] Hantschel T., *Scanning probes for nanometer scale characterization of semiconductor structure*, (2000).
- [25] Yablon D., *The importance of the probe in AFM part 1: The tip*, Wiley Analytical Science, (2016). <https://analyticalscience.wiley.com/do/10.1002/micro.2100>.
- [26] Vandervorst W., Meuris M., *Method for resistance measurements on a semiconductor element with controlled probe pressure*, (1992)
- [27] De Wolf P., Snauwaert J., Clarysse T., Vandervorst W., Hellemans L., *Characterization of a point-contact on silicon using force microscopy-supported resistance measurements*, Appl. Phys. Lett. 66, 1530, (1995), doi:10.1063/1.113636.
- [28] Tan L. S., Tan L. C. P., Leong M. S., Mazur R. G., Ye C. W., *Characterization of ultrashallow dopant profiles using spreading resistance profiling*, J. Vac. Sci. Technol. B, 20, 483 (2002), doi: 10.1116/1.1426370.
- [29] Alvarez D., *Scanning Spreading Resistance Microscopy for characterization of advanced silicon devices*, (2017).

- [30] Schulze A., Eyben P., Mody J., Paredis K., Wouters L., Celano U. Vandervorst W., *Mapping Conductance and Carrier Distributions in Confined Three-Dimensional Transistor Structures*, (2019).
- [31] Hennig R. G., Wadehra A., Driver K.P., Parker W.D., Umrigar C. J., Wilkins J.W., *Phase transformation in Si from semiconducting diamond to metallic β - Sn phase in QMC and DFT under hydrostatic and anisotropic stress*, Physical Review B82, 014101, (2010), doi: 10.1103/PhysRevB.82.014101.
- [32] Gupta M. C., Ruoff A. L., *Static compression of silicon in the [100] and in the [111] directions*, Journal of Applied Physics, 51, 1072, (1979), doi: 10.1063/1.327714.
- [33] Durandurdu M., Drabold D. A., *Pressure-induced structural phase transition of paracrystalline silicon*, Phys. Rev. B, 66, 205204, (2002), doi: 10.1103/PhysRevB.66.205204.
- [34] Mylvaganam K., Zhang L. C., Eyben P., Mody J. Vandervorst J., *Evolution of metastable phases in silicon during nanoindentation: mechanism analysis and experimental verification*, Nanotechnology 20, 305705, (2009), doi:10.1088/0957 - 4484/20/30/305705.
- [35] Eyben P., Clemente F., Vanstreels K., Pourtois G., Clarysse T., Duriau E., Hantschel T., Sankaran K., Mody J., Vandervorst W., Mylvaganam K., Zhang L., *Analysis and modeling of the high vacuum scanning spreading resistance microscopy nanocontact on silicon*, J. Vac. Sci. Technol. B 28, 401, (2010), doi: 10.1116/1.3273895
- [36] Hantschel T., Niedermann P., Trenkler T., Vandervorst W., *Highly conductive diamond probes for scanning spreading resistance microscopy*, Appl. Phys. Lett. 76, 1603, (2000), doi: 10.1063/1.126109.
- [37] Smirnov W., Kriele A., Hoffmann R., Siller, E., Hees J., Williams O. A., Yang N., Kranz C., Nebel C.E., *Diamond-Modified AFM Probes: From Diamond Nanowires to Atomic Force Microscopy-Integrated Boron-Doped Diamond Electrodes*, Analytical Chemistry, 83(12), 4936–4941, (2011), doi:10.1021/ac200659.
- [38] Hantschel T., Conard T., Kilpatrick J., Cross G., *Diamond Probes Technology*, Electrical Atomic Force Microscopy for Nanoelectronics, NanoScience and Technology. Springer, cap 11, (2019), doi: 10.1007/978-3-030-15612-1_11.

- [39] Álvarez D., Hartwich J., Fouchier M., Eyben P., Vandervorst W., *Sub-5-nm-spatial resolution in scanning spreading resistance microscopy using full-diamond tips*, Appl. Phys. Lett. 82, 1724, (2003), doi: 10.1063/1.1559931.
- [40] Hisamoto D., Kaga T., Kawamoto Y., Takeda E., *A fully depleted lean-channel transistor (DELTA)—a novel vertical ultra thin SOI MOSFET*, International Technical Digest on Electron Devices Meeting, 833-836, (1989), doi: 10.1109/IEDM.1989.74182.
- [41] Pandey, K., Paredis, K., Hantschel, T. et al., *The impact of focused ion beam induced damage on scanning spreading resistance microscopy measurements.*, Sci Rep 10, 14893 (2020), doi:10.1038/s41598-020-71826-w.
- [42] Eyben P., Matagne P., Chiarella T., De Keersgieter A., Kubicek S., Mitard J., Mocuta A., Horiguchi N., Thean A.V-Y., Mocuta D., *Accurate prediction of device performance in sub- 10nm WFIN FinFETs using scalpel SSRM-based calibration of process simulations*, 2016 International Conference on Simulation of Semiconductor Processes and Devices (SISPAD), Nuremberg, 287-290, (2016), doi: 10.1109/SISPAD.2016.7605203.
- [43] Schulze A., Hantschel T., Dathe A., Eyben P., Ke X., Vandervorst W., *Electrical tomography using atomic force microscopy and its application towards carbon nanotube-based interconnects*, Nanotechnology, 23, 305707,(2012), doi: 10.1088/0957-4484/23/30/305707.
- [44] Mayer J., Giannuzzi L. A., Kamino T., Michael J., *TEM sample preparation and FIB-induced damage*, MRS Bulletin, (2007), doi: 10.1557/mrs2007.63.
- [45] Boisen A., Hanseny O., Bouwstra A., *AFM probes with directly fabricated tips*, J. Micromech. Microeng. 6, 58-62, (1996), doi:10.1088/0960-1317/6/1/012.
- [46] Ching Tan S. C., Zhao H., Thompson C. V., *Fabrication of high aspect ratio AFM probes with different materials inspired by TEM “liftout” method*, J. Vac. Sci. Technol. B 34, 051805, (2016), doi: 10.1116/1.4961595.
- [47] <https://www.nunano.com/blog/category/Resources>
- [48] Kopycinska-Müller M., Barth M., Küttner M., Köhler B., *Phase transformation in AFM silicon tips*, Nanotechnology 28, 355701, (2017), doi: 10.1088/1361-6528/aa7be8.

- [49] Kopycinska-Müller M., Geiss R.H., Hurley D. C., *Contact mechanics tip shape in AFM-based nanomechanical measurements*, Ultramicroscopy 106 466-474, doi:10.1016/j.ultramicro.2005.12.006.
- [50] *Dry & Wet Etching - Advantages & Disadvantages of Plasma Etching & Wet Etching*. <https://www.thierry-corp.com/plasma-knowledgebase/dry-etching-and-wet-etching>.
- [51] Lamoria A., *Shallow Etch Recipe Design using DOE for Silicon Waveguides*, Thesis, Rochester Institute of Technology, (2016), access from: <https://scholarworks.rit.edu/theses/9295>
- [52] *Oxford Instruments web site*: <https://plasma.oxinst.com/campaigns/technology/icp-etching>
- [53] *Polifab*: <https://www.polifab.polimi.it/equipment/oxford-plasmalab-100-rie/>
- [54] Tinck S., Tillocher T., Dussart R., Neyts E. C., Bogaerts A., *Elucidating the effects of gas flow rate on an SF₆ inductively coupled plasma and on the silicon etch rate, by a combined experimental and theoretical investigation*, Appl. Phys. 49 38520, (2016), doi: 10.1088/0022-3727/49/38/385201.
- [55] Yeo L. P., Poh S. L., Lam Y. C., Chan-Park M. B., *Plasma polymerization of C₄F₈ thin film on high aspect ratio silicon molds*, (2004).
- [56] Le Dain G., Rhallabi A., Fernandez M. C., Boufnichel M., Roqueta F., *Multiscale approach for simulation of silicon etching using SF₆/C₄F₈ Bosch process*, J. Vac. Sci. Technol. A 35, 03E113 (2017), doi: 10.1116/1.4982687.
- [57] Xu T., Tao Z., Li H., Tan X., Li H., *Effects of deep reactive ion etching parameters on etching rate and surface morphology in extremely deep silicon etch process with high aspect ratio*, (2017), doi: 10.1177/1687814017738152.
- [58] Yinsheng P., Xiaoling Y., Bo X., Peng J., Jiebin N., Rui J., Zhanguo W., *Optimization of inductively coupled plasma etching for low nanometer scale air-hole arrays in two-dimensional GaAs-based photonic crystals*, Journal of Semiconductors, (2010), doi:10.1088/1674-4926/31/1/012003.
- [59] Ayari-Kanoun A., Aydinoglu F., Cui B., Saffih F., *Silicon nanostructures with very large negatively tapered profile by inductively coupled plasma-RIE*, J. Vac. Sci. Technol. B 34, 06KD01, (2016), doi: 10.1116/1.4964402.

- [60] Saffih F., Con C., Alshammari A., Yavuz M., Cui B., *Fabrication of silicon nanostructures with large taper angle by reactive ion etching*, J. Vac. Sci. Technol. B 32, 06FI04, (2014), doi: 10.1116/1.4901420.
- [61] Hantschel T., Clarysse T., Ajaykumar A., Seidel F., Tsigkourakos M., Nuytten T., Paredis K., Eyben P., Majeed B., Tezcan D.S., Vanderworst W., *Diamond nanoprobes for electrical probing of nanoelectronics device structures*, Microelectronic Engineering 121, 19–23, (2014), doi: 10.1016/j.mee.2014.02.024.
- [62] NanoAndMore GMBH web site: <https://www.nanoandmore.com/AFM-Probe-TL-NCH>
- [63] Nanosensors web site: <https://www.nanosensors.com/afm-tips-catalog>.
- [64] BudgetSensors web site: <https://www.budgetsensors.com/afm-probes>.
- [65] NanoWorld web site: <https://www.nanoworld.com/afm-probes-series>.
- [66] He H., Zhang H., Yang J., Yang F., *Silicon tip sharpening based on thermal oxidation technology*, Microsyst Technol, 23:1799–1803, (2017), doi: 10.1007/s00542-016-2941-0.
- [67] Akamine S., Quate C. F., *Low temperature thermal oxidation sharpening of microcast tips*, J. Vac. Sci. Technol. B10, 2307, (1992), doi: 10.1116/1.586059.